The University Of Sheffield.

University of Sheffield

School of Mathematical and Physical Sciences

Theoretical and Simulation Approaches to Polymer Crystallisation and Self-Assembly in Chiral Liquid Crystals

Kutlwano Gabana

A thesis submitted in partial fulfilment of the requirements for the Doctor of Philosophy degree in Physics

Declaration

I declare that this thesis was composed by myself and that the work contained herein is my own, except where explicitly stated otherwise in the text.

Abstract

This research investigates complex phenomena during the polymer crystallisation and self-assembly of chiral liquid crystals through theoretical concepts in physics and molecular dynamics simulation.

Self-poisoning has been reported in three poly(ethylene brassylate) (PEB) polymers, which also exhibit quantised lamellar thickening; where the crystalline layer increases by multiples of the repeating unit's length. The poisoning is characterised by two minima in the crystallisation rate of the polymers. A one-dimensional quantitative model is developed from the extension of the Higgs and Ungar model to study the self-poisoning. The parameterised model agrees with the experimental curves, even capturing the minima.

Another case of self-poisoning was identified in precision polyethylene derivatives, specifically bromine-substituted poly(ethylene bromine) (PEBr). The three PEBr polymers exhibiting self-poisoning showed a growth rate minimum near the melting point of a less stable form of the polymer. The one-dimensional model developed for PEB was found to better fit the experimental growth rate data of PEBr compared to models attributing poisoning to competition between more and less stable forms.

A recent united-monomer model of polyethylene (PE) was extended by incorporating bromine atoms to mimic PEBr, enabling further study of its crystallisation. In this model, one bead represents a $-C_2H_4-$ unit or $-C_2HBr_2-$. Two crystallisation protocols were employed: self-seeding and continuous cooling. The self-seeded systems displayed temperature-dependent quantised lamellar thickening, while the continuous cooling systems did not. Quenching the system revealed bromine alignment into layers, similar to experimental observations in PEBr.

The crystallisation of the high-molecular-weight poly(lactic acid) stereocomplex is significantly hindered in a 1:1 mix. It has been suggested that this is due to the local fluctuations in enantiomer concentration within the melt. A Monte Carlo simulation on a two-dimensional lattice is employed to mimic the diffusion-driven motion of PLA enantiomers, capturing the effects of temperature and diffusion on stereocomplex formation. Crystallisation and melting probabilities are parameterised to investigate their interplay with diffusion. Metrics such as crystallinity of the stereocomplex and homochiral clustering are tracked during the simulations. The results of the simulation suggest that the stereocomplex can grow at lower tempertures.

A liquid crystal phase (LC) with chiral columns composed of achiral molecules with straight cores and aliphatic long chains is also reported. The observed LC phases exhibit an equal number of left- and right-handed columns, rendering the overall phase achiral. The chirality arises from a balance between the parallel stacking of the cores to maximise $\pi - \pi$ interactions and the avoidance of clashes by the tails. Two interacting dimers of the molecules were found to prefer perpendicular arrangements to optimise packing and minimise head-on clashes. A model of rotating quadrupoles was developed to capture the

interactions of dimers within the columns due to their similarity to linear electric quadrupoles. The experimentally observed Fddd configuration was found to have the lowest energy per dimer compared to three alternative configurations.

Publications

1. Kutlwano Gabana, Gillian A. Gehring, Xiangbing Zeng, and Goran Ungar. Monte Carlo Study of Self-Poisoning in Racemic Poly(lactic Acid) Stereocomplex Crystallisation. *Underpreparation*

2. Kutlwano Gabana, Gillian A. Gehring, Xiangbing Zeng, and Goran Ungar. Competition between Different Fold-lengths or Crystal Forms: A Quantitative Study of Self-Poisoning Mechanisms in Precisely Bromine-Substituted Polyethylene. *Ready for submission to Macromolecules*

3. Kutlwano Gabana, Gillian A. Gehring, Hendrik Meyer, Goran Ungar, Xiangbing Zeng, and William S. Fall. Molecular Simulations of Quantized Lamellar Thickening in Polyethylenes with Regularly Spaced Brominated Groups. *Macromolecules.* (Accepted)

4. Kutlwano Gabana, Gillian A. Gehring, Xiangbing Zeng, and Goran Ungar. Quantitative Model of Multiple Crystal Growth Rate Minima in Polymers with Regularly Spaced Substituent Groups. *Macromolecules.*2024;57(4):1667–1676

5. Ya-xin Li, Hong-fei Gao, Rui-bin Zhang, Kutlwano Gabana, Qing Chang, Gillian A. Gehring, Xiao-hong Cheng, Xiang-bing Zeng and Goran Ungar. A case of antiferrochirality in the liquid crystal phase of counter-rotating staircases. *Nature Communication.* 2022;13:384

Acknowledgments

I would like to thank my supervisors Prof Gillian A. Gehring, in the Dept of Physics and Astronomy at the University of Sheffield and Dr Xiangbing Zeng, in the Dept of Materials Science at the University of Sheffield, whom I appreciate for their guidance and tender care during my PhD. I would also like to thank Prof. Nigel Clarke, in the Dept of Physics and Astronomy at the University of Sheffield, for ensuring that all my administrative was up to date. I thank Prof. Goran Ungar for the interesting research he has provided us with.

I would like to say a big thank you to Dr William S. Fall at Institut Charles Sadron, Université de Strasbourg, for his patience during our collaboration and his ever so help conversations.

Lastly, I would like to thank the Government of Botswana for sponsoring me through the PhD. The University of Sheffield Dept of Physics and Astronomy is also acknowledged for their financial support.

Dedicated to my God,
For the opportunities He has and continues to give me,
And,
To my wife and bestfriend, Esther,
Our little Rhema,
And Family and Friends.

Contents

List of Figures

List of Tables

1 Introduction

Over the last century, there has been a shift from reliance on condensed hard matter to materials designed for specific applications. Hard condensed materials are characterised by the arrangements of its particles into highly ordered lattices. It is then possible to predict the behaviour and properties of the material from the interactions of its particles. Many of these properties are now well known and understood as compared to soft matter materials. Soft matter physics is a subfield of condensed matter physics dealing with materials that are easily deformed by thermal fluctuations and external forces. Materials in this category exhibit diverse properties and include polymers, liquid crystals, colloids, gels, emulsions, foams, and surfactants. These systems consist of basic units larger than atoms but smaller than the overall size of the materials, and exhibit weak interactions. Consequently, their properties, such as high sensitivity to temperature changes, make them challenging to study.

The name 'soft matter' was in fact coined by Pierre-Gilles de Gennes, a French physicist, during his Nobel prize talk. He received a Nobel prize in physics for his work adapting methods used to study hard matter ordering to soft matter, particularly liquid crystals and polymers. These have been used in studying phase transitions in liquid crystals. However, there is still a lot that remains unknown and misunderstood about polymers and liquid crystals to this day. There are many attempts to synthesise new polymers and liquid crystals for specific use to take advantage of some of their properties, yet this is limited by the fact that not many successful theories exist to predict the results. It is clear that first principle approaches would not be effective in computing the interactions of the systems with many atoms unlike in hard matter systems, but rather it calls for effective potentials and coarse-grained approaches.

1.1 Objectives of the Study

Polymers are the most widely used soft matter materials. Polymers are materials composed of large chain-like molecules formed from repeating units, synthesised from smaller molecules called monomers. They have many functions in everyday life, from being used as simple carrier bags to being used in construction.In most applications, polymers are used in their crystallised form, where segments of their chains become ordered, resembling the structure of hard matter. However because of their long chain nature and intrinsic polydispersity (the chains having a distribution of lengths), their crystallisation is not as well understood as compared to metals. Liquid crystals are another significant class of soft materials, combining fluidity similar to isotropic liquids with the long-range order characteristic of crystalline solids. However, phenomena such as the self-poisoning effect in polymer crystallisation and the spontaneous formation of chirality in liquid crystals remain poorly understood from a quantitative theoretical perspective.

This research focuses on exploring complex experimental phenomena in polymer and liquid

crystal systems through theoretical concepts and computer simulations. To achieve this my supervisors Professor Gillian Gehring and Dr Xiangbing Zeng, and I collaborated with Professor Goran Ungar from the Materials department within the University to identify such systems. Dr Zeng and Professor Ungar provided guidance on how to interpret the experimental data and to the key interactions to consider in our coarse-graining. Our collaboration proved very fruitful as insight offered from an experimental view would either point to an existing theoretical concept or lead to novel ideas. The approach taken afterwards was to implement existing theories in physics where possible to develop theoretical models that would able to interpret or reproduce the experimental data. This thesis aims to:

- Identify polymer systems suitable for theoretical analysis.
- Understand and improve existing theories relevant to these systems or similar ones.
- To design appropriate models and simulations to capture the mechanisms of the systems.
- parameterise models to compare theoretical results with experimental data.

1.2 Thesis Outline

The remainder of this chapter introduces polymer crystallisation, chirality in polymers, and the systems central to this thesis. It begins with the basics of polymer crystallisation, followed by a discussion of secondary nucleation theories, such as the Lauritzen-Hoffman theory, and introduces self-poisoning as a phenomenon these theories fail to explain. The chapter also highlights recent cases of self-poisoning in precision polymers, specifically poly(ethylene brassylate) and poly(ethylene bromine) (PEBr), as well as poly(lactic acid) which are investigated in this thesis. It continues by exploring chirality in polymers and liquid crystals, focusing on its impact on their assembly. The chapter concludes by presenting a newly discovered columnar liquid crystal phase with chiral columns formed from achiral molecules, exhibiting Fddd symmetry.

Chapter 2 outlines the methodologies used in the results chapters. It begins by detailing the curve-fitting method used to parameterise the quantitative models of self-poisoning developed in Chapters 3 and 4. The chapter continues with an explanation of molecular dynamics simulations, particularly the Large-scale Atomic/Molecular Massively Parallel Simulator (LAMMPS) software, which is employed in Chapter 5 to simulate PEBr. Monte Carlo dynamics are then introduced, along with the relevant algorithms. The chapter concludes by describing the model of linear electric quadrupoles used in Chapter 7 to quantify interactions in the chiral liquid crystal system.

Chapter 3 presents a quantitative coarse-grained model to explain self-poisoning in polymers with quantised lamellar thickness, adapted from the Higgs and Ungar model for long-chain n-alkanes. This model is parameterised for PEB, enabling comparisons with experimental data.

Chapter 4 extends the study of self-poisoning by examining PEBr. The one-dimensional model developed for PEB is shown to fit experimental growth rate data for PEBr better than a model based on competition between crystal forms.

Chapter 5 focuses on molecular simulations of PEBr using LAMMPS. These simulations investigate its growth and provide further insights into the mechanisms identified in Chapter 4.

Chapter 6 employs a Monte Carlo simulation to study the crystallisation of the poly(lactic acid) stereocomplex. This chapter explores the effects of temperature and diffusion on crystallisation, tracking metrics such as stereocomplex crystallinity and homochiral clustering.

Chapter 7 introduces a model of rotating quadrupoles to quantify interactions in a liquid crystal system with chiral columns. The experimentally observed Fddd configuration is shown to have the lowest energy per dimer compared to three alternative configurations.

Chapter 8 summarises the main findings of this research and discusses potential directions for future work.

1.3 Polymer Crystallisation

1.3.1 Polymers

Polymers are made up of long flexible chain-like molecules consisting of repeating substructures that are covalently bonded together [1, 2, 3]. They are made from smaller molecules called monomers through a process known as polymerisation. One of these polymer chains could range from several microns to mm in length. Polymers are ubiquitous in everyday life, with applications ranging from shopping bags to construction materials, many of which require their crystalline form for enhanced properties.

1.3.2 Crystallisation

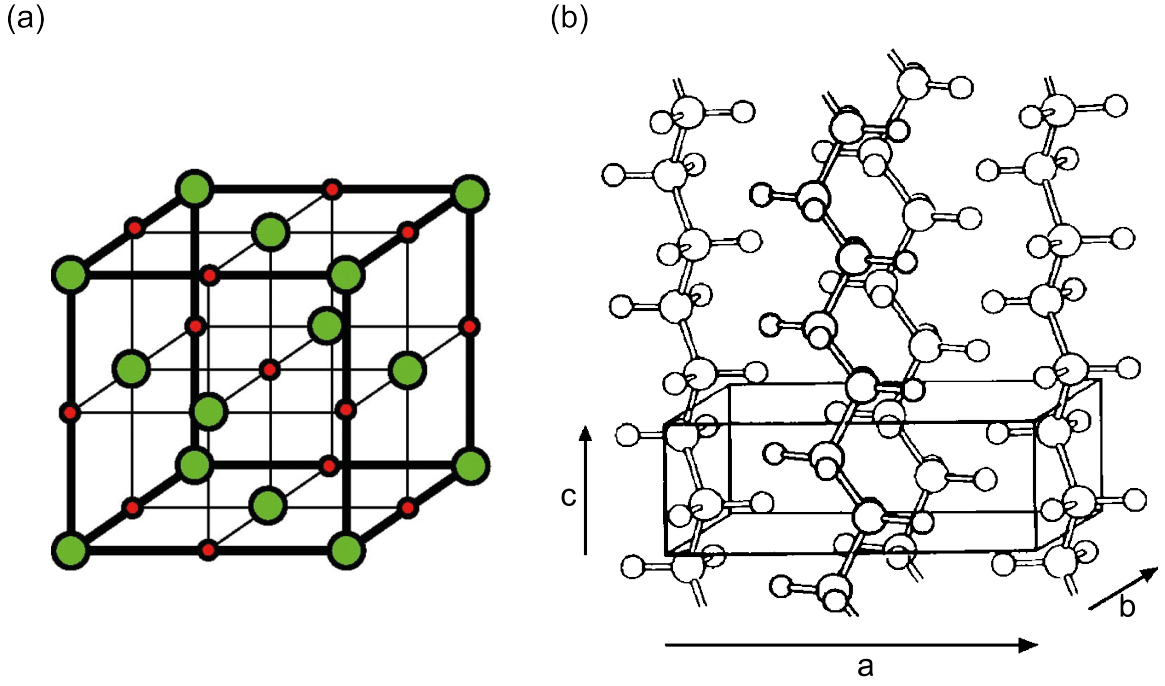

Figure 1.1: Unit cell of sodium chloride (NaCl) and polyethylene. (a) The unit cell of NaCl showing the position and order of the ions. The sodium ions are depicted as small red spheres and the chloride ions as the green bigger spheres. (b) The unit cell of polyethylene which is orthorhombic and contains 4 chains, with its chains arranged along the c-direction. Reproduced from [4] and [5].

Crystallisation is a process by which atoms, ions, or molecules arrange themselves into a well-ordered, repeating structure known as a crystal. The crystal is characterised by long-range positional and orientational order [6]. In materials such as metals and ionic compounds, this results in the formation of a lattice. The lattice is a three-dimensional (3D) array of points representing the equilibrium positions of the constituent particles [7]. The lattice exhibits periodicity, meaning the arrangement repeats uniformly throughout the crystal. Its structure is defined by a unit cell, the smallest repeating unit that captures the symmetry and spatial arrangement of the lattice. The entire crystal structure can be reconstructed by translating the unit cell in three dimensions [8].

While metals and ionic compounds form simple lattices, polymers crystallise in more complex patterns due to their chain-like molecular structure. The repeating units are small, and the crystal's periodicity is consistent across long distances. A typical example of this is sodium chloride (NaCl), with the unit cell shown in figure 1.1(a), consists of sodium ions (in red) and chloride ions (in green) arranged in a repeating pattern.

Polymers can undergo crystallisation akin to that of smaller molecules, where segments of chains lose their mobility and become ordered as they are cooled or as the solvent they are dissolved in is evaporated [3, 9]. In contrast, polymer unit cells are more complex due to the large, chain-like nature of polymer molecules. Instead of simple atoms or ions, the unit cell of a polymer contains segments of long molecular chains, as seen with polyethylene in figure 1.1(b), leading to irregular shapes and arrangements.

1.3.3 Polymer Single Crystal

Early studies on polymer crystallisation suggested that polymers could only achieve low crystallinity, with most segments remaining disordered [10]. Later, it was discovered that higher crystallinity polymers could be grown with polymers made of chains that have less branching and are more flexible like low-density polyethylene (PE) [11, 12]. Even more interestingly, near 100% crystallinity crystals, often with help of seeding, could be grown under special conditions of slow crystallisation and from dilute solution (under 0.1% concentration), and these crystals are called polymer single crystals [13, 14, 15, 11]. Polymer single crystals are regular shape, plate-like, very thin crystals that are much larger laterally, shown in figure 1.2(a) and (b).

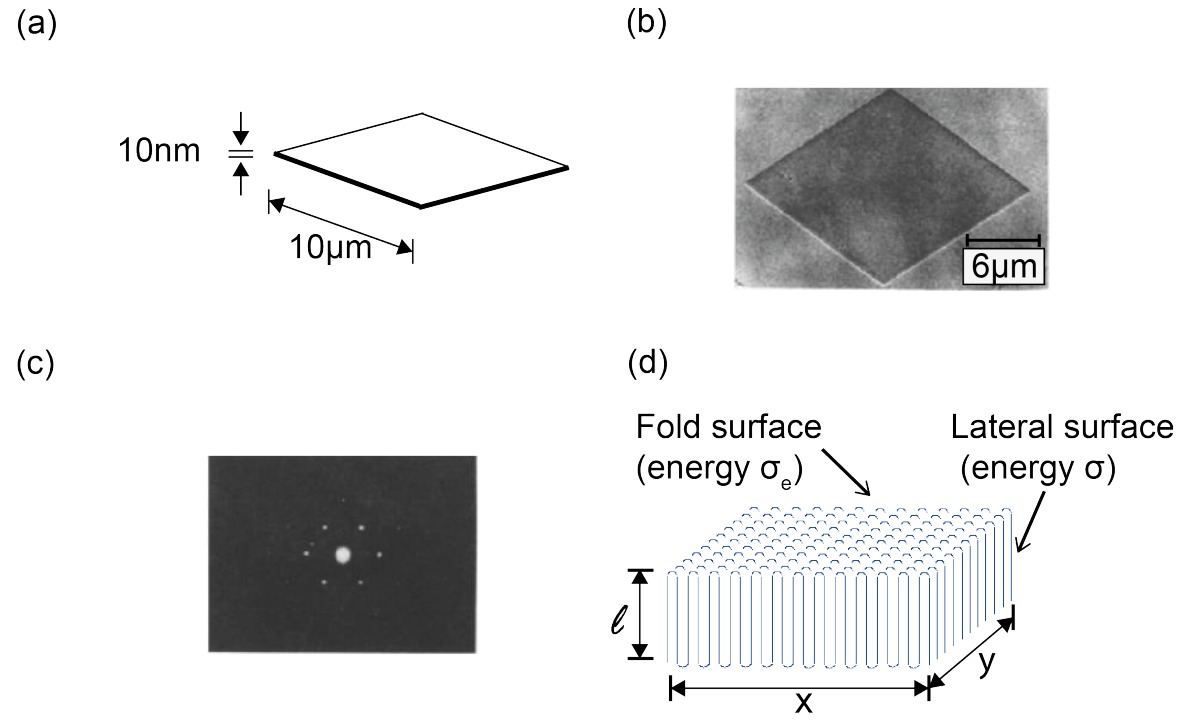

Figure 1.2: Molecular organisation in a polymer single crystal. (a) Illustration of a polymer single crystal with the thickness significantly smaller than the lateral length. (b) Image of a polymer single crystal under the microscope. (c) Diffraction pattern showing the direction of the chain orientation, along the thickness of the polymer single crystal. (d) The folded chain arrange into lamella with the straight side of the chains along the thickness of the lamella. The chains are added to the lamella perpendicular to the thickness. This creates a fold surface at the ends and another in the direction of growth of the lamella. Adapted from [10]

Experimental results from electron microscopy have revealed that the chains in polymer single crystals are oriented along the thickness of the crystal, the shortest dimension of the crystal, the c-axis of the unit cell [16] as shown in figure 1.2(c). The thickness of the crystal (about 10nm) is much shorter than the full length of the molecules, (several microns to mm long) and hence this result has led to a well-established concept of the chain folded crystallisation. The polymer chains only go a short way perpendicular to the lateral dimensions before folding back and forth many times on themselves. The folded chains arrange in thin, plate-like crystalline lamellar structures [11]. Each fold occurs at the surface of the lamella, and the polymer chains are added perpendicular to the lamellar surface. The chains then leave and re-enter the lamella at nearest neighbouring positions [11]. The resulting structure has two surfaces, the lateral surface where the chains are added to the lamella, and the fold surface at the ends figure 1.2(d).

1.3.4 Crystal growth

Classically many substances crystallise through nucleation and growth, where nucleation starts the process and then the crystal spreads [17]. Similarly, the process of polymer crystallisation can be divided in these two stages. Nucleation, the initial step in crystallisation, involves the spontaneous arrangement of polymer chains into an ordered structure [18]. This process can be categorised into two main types: primary nucleation and secondary nucleation [19]. Each type plays a distinct role in the formation and growth of polymer crystals. Primary nucleation refers to the formation of the very first crystalline nuclei in a polymer melt or solution [17]. It can take place uniformly throughout the polymer melt or solution without any preferential nucleation sites, homogeneous, or at specific sites within the polymer melt or solution, such as impurities, additives, or surfaces of the container, heterogeneous [20].

Homogeneous nucleation occurs when polymer chains arrange into a crystalline structure without external assistance. This process requires a significant amount of energy because it involves the creation of new surfaces (interfaces between the crystalline and amorphous regions) without any external assistance. While in heterogeneous nucleation the sites lower the energy barrier required for nucleation by providing a template that facilitates the orderly arrangement of polymer chains. The size of the critical nucleus required for stable nuclei formation depends on the free energy barrier to crystallisation. This critical nucleus size determines the difficulty of nucleation and is influenced by factors like undercooling, $T - T_m$ or supersaturation.

Secondary nucleation occurs on the surfaces of pre-existing crystals, where new nuclei form. This process is crucial during the growth phase of crystallisation. Primary nucleation is normally dominant only at the start of the crystallisation in non-seeded (without a pre-existing nucleus) processes [21]. Then polymer chains in the melt or solution can attach to the surface of these nuclei, forming new crystalline layers. Then further nuclei are formed on the pre-existing crystalline surfaces to allow for further crystal growth. This process continues, leading to the growth as more chains attach and crystal grows.

1.3.5 Structural Hierarchy in Semi-crystalline Polymers

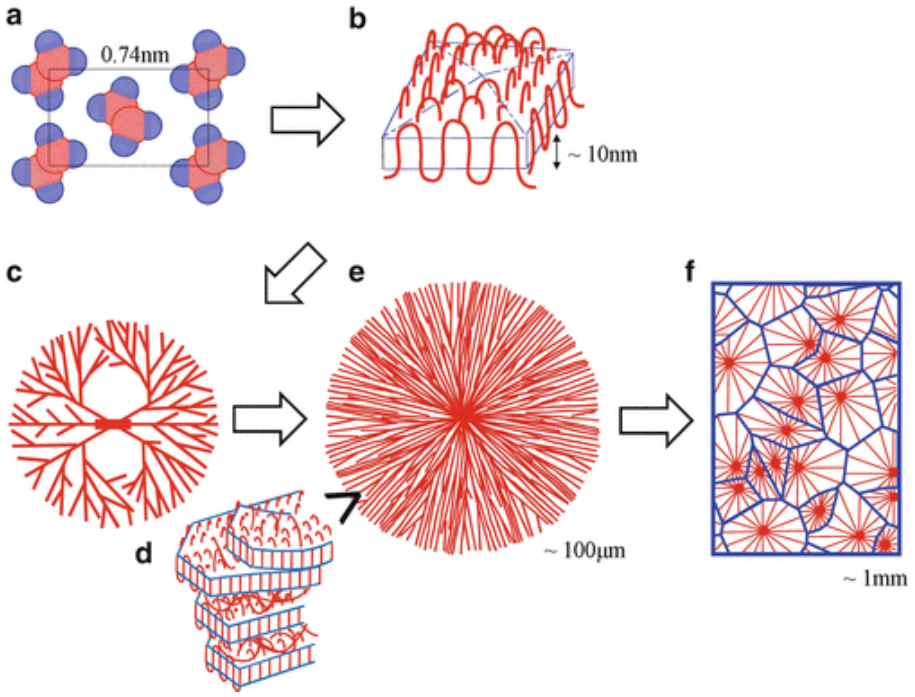

Figure 1.3: Structural Hierarchy in Semi-crystalline Polymers. a Represents the unit cell of the crystalline structure (with a lattice spacing of 0.74 nm in one direction). This is the smallest structural level, where the basic repeating units pack into a regular arrangement. b Shows the formation of a lamellar structure, which consists of folded polymer chains. The thickness of these lamellae is around 10 nm. The chains fold back and forth, creating a layered structure with alternating crystalline and amorphous regions. c Illustrates the formation of a spherulite. The lamellae branch out radially, creating a pattern that resembles tree branches or a fan-like shape. This branching helps to fill space during the crystallisation process. d Depicts the semi-crystalline arrangement of the crystalline layers sandwiching the amorphous regions. e Shows a fully developed spherulite with a diameter of approximately 100 μm. The radial growth of the lamellae from the nucleation point creates this larger, spherical structure. f Illustrates the macroscopic morphology of the crystallised polymer material, with spherulites impinging into each other filling the entire volume. The size of these spherulites can reach around 1 mm, and grain boundaries (blue line) form where different spherulites meet. Taken from [22]

Melt-grown polymers also crystallise forming lamellar structures [15, 23]. Unlike in the ideal case of single crystal polymers with one lamella (figure 1.3b), most melt- and solution-grown crystals are semi-crystalline, with multiple lamellae separated by amorphous regions [24] (figure 1.3d). The lamellar in these semi-crystalline polymers is similar to those in the single crystal polymers,

albeit less ordered. For semi-crystalline polymers, the lamellar thickness is the crystalline layer thickness plus that of the amorphous layer. In some cases of high nucleation a chain can pass through an amorphous region from one lamella and joins onto another. Such chains are called tie molecules or tie chains [25].

In semi-crystalline polymers, the lamellar arrangement often evolves into more complex structures known as spherulites [26] such as in figure 1.3e. Spherulites are well-known phenomenon that is ubiquitous to many compounds of small molecule solids [27, 28, 29]. In polymers they form as the polymer crystallises, with lamellae radiating outward from a nucleus to create a spherical, 3D structure. Unlike simpler lamellar arrangements, in spherulites, the lamellae can twist and branch as they grow (figure 1.3c), adding to the complexity of the structure. Within the spherulite, the lamellae are interspersed with amorphous regions. When viewed under polarised light, spherulites show that the polymer chains are arranged tangentially around the nucleus, and thus the lamellae grow radially from the centre nucleus. The spherulites will grow until they crash into each other, forming interspherulitic boundaries (figure 1.3f) that may exhibit less perfect crystalline order compared to the core.

In many polymers, spherulites are often observed in the range of 1–100 μm, but they can grow larger under slower cooling conditions, reaching sizes up to several millimeters [22, 30]. This makes them visible under an optical microscopy which allows for the evolution of their crystalline layers to be directly measured. The rate at which the crystalline lamellae extend outward from a nucleation site to form a spherulite is referred to as the growth rate of the polymer. It describes how quickly the crystalline regions within the polymer grow, measured as the distance travelled by the growth front per unit time. In most instances the radii of the spherulites are seen to grow linearly with time [31].

The growth rate values obtained from directly measuring the change in the diameter of the spherulites with time are very accurate. On the other hand, the process may take a long time and in polymers with high-nucleation the spherulites may be too small for the growth rate to be determined this way [32]. In such instances it is better to measure the overall transformation from the amorphous to the crystalline state occurs in the polymer, referred to as the crystallisation rate [31]. It includes both the nucleation rate and the growth rate of crystalline regions. The crystallisation rate represents the speed of the entire crystallisation process, resulting in a change in the degree of crystallinity over time. The crystallisation rate ν is related to the growth rate by the equation below,

$$\nu = GN(t) \tag{1.1}$$

where G is the growth rate and $N(t)$ is a time dependent function about the number of spherulites growing [31].

It is traditionally measured using the Differential Scanning Calorimetry (DSC), where the heat

released during crystallisation is monitored [33]. The area under the exothermic peak in a DSC curve corresponds to the extent of crystallisation, and the time to reach half of the peak height (half-time) gives an indication of the crystallisation rate. For polymers with high heating and cooling rates, typically ranging from hundreds to thousands of degrees Celsius per second, an advanced calorimetric Fast Scanning Calorimetry (FSC) is preferred over the conventional DSC [34]. The core principle of FSC is similar to that of traditional DSC, where the heat flow associated with thermal transitions is monitored. Techniques like X-ray diffraction (XRD) or infrared spectroscopy (FTIR) can also track changes in crystallinity over time, providing a measure of the crystallisation rate.

1.3.6 Thermodynamics of polymer crystallisation

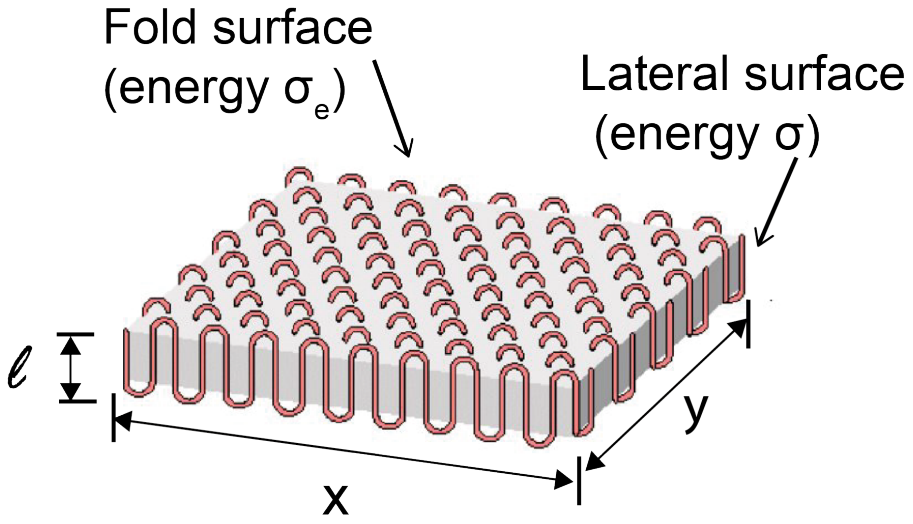

Figure 1.4: Lamellar structure illustrating lateral dimensions x and y, average thickness l and along with the surface energies per unit area σ for the lateral surfaces and σ_e for the fold surfaces.

The formation of a lamella crystal begins with nucleation, followed by the addition of new molecular chains to the growing crystalline structure. This process creates two distinct surfaces: the fold surface, where chains change direction, and the lateral surface, where new chains attach. The free energy change associated with this process forming a lamella crystal with lateral dimensions x and y, average thickness l and along with the surface energies per unit area σ for the lateral surfaces and σ_e for the fold surfaces as shown in figure 1.4, can be divided into two, the bulk and surface energy changes.

The bulk free energy change ($\Delta\Phi_{bulk}$) represents the difference between the crystalline and amorphous states, and is given by,

$$\Delta\Phi_{bulk} = xyl\Delta\Phi_c \tag{1.2}$$

where xyl is the volume of the lamella and $\Delta\Phi_c$ is the free energy change per unit volume for the transition from amorphous to crystalline state and is taken to be positive. The change in the surface energy accounts for the creation of new surfaces on the sides of the lamella and creation of new surfaces at the folds surfaces. The total change due to surface energy $\Delta\Phi_{surface}$ is then

$$\Delta\Phi_{surface} = 2xy\sigma_e + 2l(x+y)\sigma \tag{1.3}$$

The total change in the free energy $\Delta\Phi_f$ is then

$$\Delta\Phi_f = 2xy\sigma_e + 2l(x+y)\sigma - xyl\Delta\Phi_c \tag{1.4}$$

If the lateral dimensions x and y of the lamella are significantly larger than the thickness l, the term $2l(x+y)\sigma$ becomes negligible compared to $2xy\sigma_e$, simplifying the free energy calculation:

$$\Delta\Phi_f \approx 2xy\sigma_e - xyl\Delta\Phi_c \tag{1.5}$$

At the melting temperature of the crystal, T_m, $\Delta\Phi_f$ is zero and

$$\Delta\Phi_c(T_m) = 2\sigma_e/l \tag{1.6}$$

For an infinitely large perfect crystals the free energy change per unit volume is,

$$\Delta\Phi_{c,\infty}(T) = \Delta H_{c,\infty}(T) - T\Delta S_{c,\infty}(T) \tag{1.7}$$

where $\Delta H_{c,\infty}(T)$ and $S_{c,\infty}(T)$ are the enthalpy and entropy changes during the crystallisation for the infinite crystal.

At the melting temperature of infinitely large crystal, $T_{m,\infty}$, the crystal becomes in equilibrium with the melt around it and $\Delta\Phi_{c,\infty}$ becomes zero.

Then equation (1.7) can be rearranged to have $\Delta S_{c,\infty}(T_{m,\infty})$ as the subject of the formula

$$\Delta S_{c,\infty}(T_{m,\infty}) = \Delta H_{c,\infty}(T_{m,\infty})/T_{m,\infty} \tag{1.8}$$

At T_m the free energy change per unit volume of the infinitely large crystal is non-zero and given by,

$$\Delta\Phi_{c,\infty}(T_m) = \Delta H_{c,\infty}(T_m) - T\Delta S_{c,\infty}(T_m) \tag{1.9}$$

For high melting temperatures T_m the differences in entropy change between T_m and $T_{m,\infty}$ tend to be minimal. Therefore it is reasonable to approximate $\Delta S_{c,\infty}(T_m)$ as,

$$\Delta S_{c,\infty}(T_m) \approx \Delta S_{c,\infty}(T_{m,\infty}) \tag{1.10}$$

Assuming that similarly there is little temperature dependence, then $\Delta H_{c,\infty}(T_m)$ can be approximated as,

$$\Delta H_{c,\infty}(T_m) \approx \Delta H_{c,\infty}(T_{m,\infty}) \tag{1.11}$$

By substituting equations 1.10 and 1.11 into 1.9 we get,

$$\Delta\Phi_{c,\infty}(T_m) = \Delta H_{c,\infty}(T_{m,\infty}) - T_m\Delta H_{c,\infty}(T_{m,\infty})/T_{m,\infty} \tag{1.12}$$

Equating equations 1.6 and 1.12 we get

$$2\sigma_e/l = H_{c,\infty}(T_{m,\infty}) - T_m\Delta H_{c,\infty}(T_{m,\infty})/T_{m,\infty} \tag{1.13}$$

This can be rearranged as,

$$T_m = T_{m,\infty}\left[1 - \frac{2\sigma_e}{l\Delta H_{c,\infty}T_{m,\infty}}\right] \tag{1.14}$$

This derivation leads to the well-known Gibbs-Thomson equation, which relates the melting temperature of a lamella with a given thickness to the melting temperature of an infinitely large crystal. The equation can also be rearranged to obtain the minimum stable lamellar thickness at a given temperature,

$$l_{min} = \frac{2\sigma_e}{\Delta H_{c,\infty}\Delta T} \tag{1.15}$$

where $\Delta T = T_{m,\infty} - T_m$. The critical lamellar thickness is inversely proportional to supercooling as observed experimentally. Lamellae with greater thickness can also grow, contributing to metastable states characteristic of chain-folded crystallisation. However, an increase in thickness typically lowers the free energy, making the crystal more stable overall

1.3.7 Kinetic Theory of Polymer Crystallisation

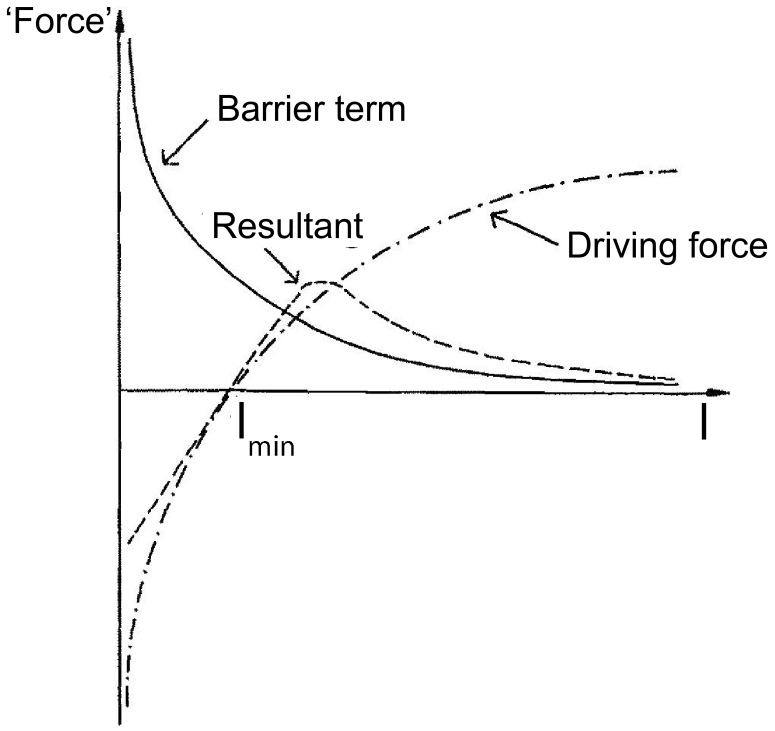

Figure 1.5: The growth rate due to the competition between the barrier term and the driving force. The barrier term is proportional to $\exp(-E_b/(kT))$, where E_b is the barrier, The driving force increases with l, but at a slower rate than the decrease of the force due to the barrier term. Hence the overall growth rate is positive for $l > l_{min}$ but decreases to zero at large l, with a maximum in between. Adapted from [35]

It is assumed that polymers growth is controlled by kinetics and not thermodynamics [35]. This has led to a rise in many kinetic theory models. These models are all characterised by a driving force and an energy barrier [35]. The driving force for crystallisation increases with supercooling, leading to higher crystallisation rates at lower temperatures. This driving force is also related to the thickness of the lamellar, for $l > l_{min}$, the driving force increases. It is usually derived from the free energy difference from the melt and the crystal and is normally the same for all the theories. The molecules then must overcome a barrier to attach to the crystal

and increase its lamella [35]. The exact nature of this barrier is specific to each theory. Often the barrier term is used instead of the barrier. The barrier term represents the energy required for molecular attachment and is proportional to $\exp(-E_b/(kT))$, where E_b is the barrier. The growth rate of the polymer is then a result of the competition between the two forces, figure 1.5.

Lamella of any thickness greater than the minimum stable thickness can be formed, however it is the thickness with the fastest growth rate that is observed to grow. The experimental findings indicating that the growth rate is proportional to $\exp(-1/\Delta T)$ and the formation of facetted single crystals in solution provide strong evidence that polymer crystallisation is governed by nucleation. The formation of well-defined, single crystals in the solution indicates a specific, orderly process of crystal formation, rather than a more random or amorphous aggregation of polymer molecules [35]. As a result, most kinetic theories are secondary nucleation theories. In this introduction the two most famous secondary nucleation theories of Lauritzen - Hoffman and Saddler - Gilmer are discussed, with attention paid to the former as it is analytical like the models developed later in this work.

1.3.8 Lauritzen - Hoffman Theory

The Lauritzen-Hoffman (LH) theory is one of the most widely used kinetic theories, providing a quantitative framework for understanding polymer crystal growth [36, 37]. The theory focuses on secondary nucleation as the driving force for crystallisation, assuming the preexistence of a crystal.

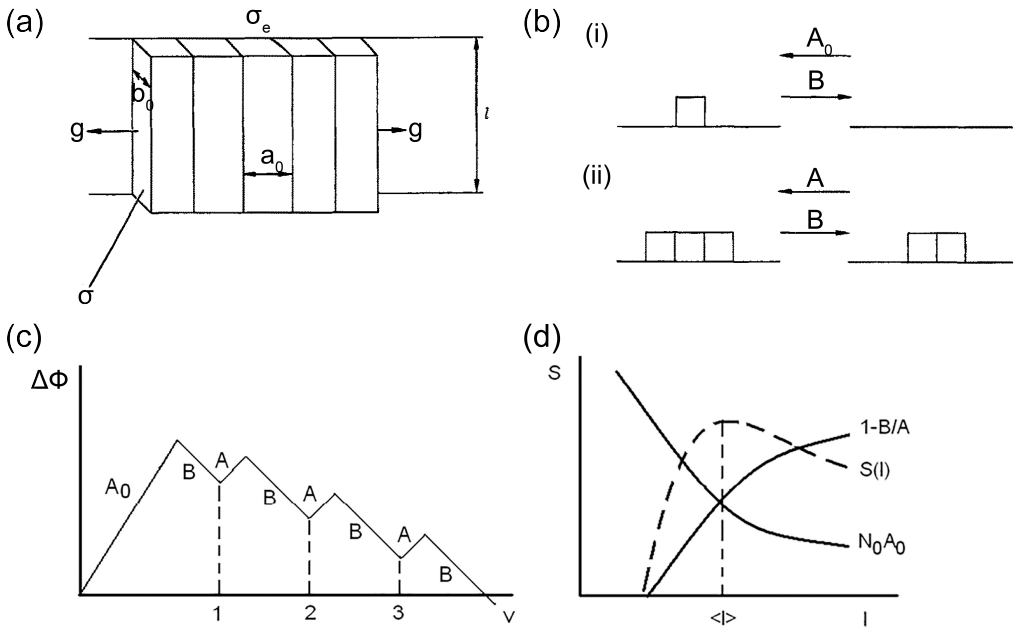

Figure 1.6: Schematic for the Lauritzen - Hoffman theory and free energy landscape. (a) The model of LH theory for stems of width a_0 and depth b_0. The surface tensions on fold and lateral surfaces are σ_e and σ, respectively. Taken from [35]. (b) The possible transitions in the LH theory. A's and B's are rate constants for addition and subtraction of a stem and depend upon the number of neighbours of a stem, from [35]. (c) The change in free energy for the LH theory with the number of stems. (d) The flux S(l) of crystals grown with length l, and driving force $(1 - B/A)$ and the barrier term (N_0A_0), where N_0 is the number of crystals growing with lamella of thickness l, equation 1.22. The barrier favours growing of thin crystals whilst the driving force favours thicker crystals. Adapted from [38]

In the LH theory, the growth front is taken to be the lateral surface and it is taken to be smooth as in figure 1.6. The first step involves a single molecular stem weakly adsorbing to a smooth crystal lateral surface, forming the initial foundation for growth [36]. This deposition creates two lateral surfaces, increasing the free energy by $2b_0\sigma l$, where b_0 represents the layer thickness and, l is the length of the segment and σ is the surface energy per unit area. This initial step the faces the biggest energy barrier and this makes it the rate controlling step, and the magnitude of the barrier increases with the length of the segment l [36].

The second step is the attachment of this stem to the surface, which result in it losing conformational entropy and decreases the energy by $a_0b_0l\Delta\phi_c$, where a_0 is the width of the stem and $\Delta\phi_c$ is the free energy change of crystallisation per unit volume. The LH theory assumes that this single stem is sufficient to act as the secondary nucleus for growth. Another assumption of the LH theory is that the subsequent stems of a folded chain are added adjacently. This means that the next steps are of the stems of the same chain being attached either side of the nucleus and they all grow with the same length as the nucleus. A result of this assumption is that no

other chain can grow until the first is fully grown. Each of the subsequent stems contributes two folded surfaces and this increases the energy by $2a_0b_0\sigma_e$, where σ_e is the energy penalty for creating a folded surface. The attachment of the stems reduce the energy by $a_0b_0l\Delta\phi_c$.

The possible transitions of adding and removing stems are captured in figure 1.6b using the rate A_0, A and B. A_0 is the rate of adding new stems onto a clean smooth crystal surface and have an corresponding removal rate B. A is the rate of addition of the next stems adjacent an existing stem of an equivalent length, and these steps are removed at rate B. These rates can be estimated by the Arrhenius equation using the associated free energy changes as:

$$A_0 = \beta \exp\left(-2b_0\sigma l/(kT)\right) \tag{1.16}$$

$$B = \beta \exp\left(-a_0b_0l\Delta\phi_c/(kT)\right) \tag{1.17}$$

$$A = \beta \exp\left(-2b_0a_0\sigma_e/(kT)\right) \tag{1.18}$$

.

Where β is the number of times per second that a molecule attempts to attach to the surface, l is the lamellar thickness, and k is the Boltzmann constant.

The dynamics and assumptions of the LH theory make for a simple theory of fundamental processes, nucleation, and lateral growth as means of growing the crystal. This helps define natural parameters that describe the polymer crystallisation [35]. The first parameter is the nucleation rate, i, which is the rate of depositing stems per unit substrate. The second parameter is then the lateral spreading rate, g, which is the difference between the attachment and detachment of stems. By considering the behaviour of the two rates, the three-regime event arises, each describing the interplay between the two rates.

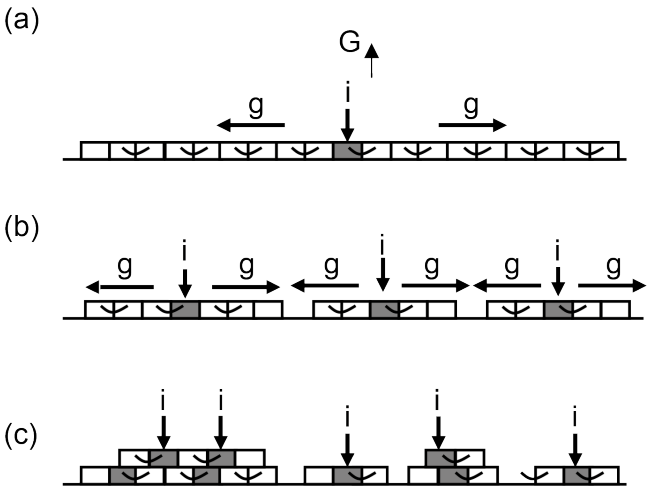

Figure 1.7: Schematic of the three regimes from the LH theory. The nucleus as depicted with dark rectangles and the rest of the stems in white. (a) Regime I, (b) regime II and (b) regime III.

In the first regime, which occurs at high temperatures, the lateral spreading rate (g) is significantly greater than the nucleation rate (i). Once a nucleus is attached to the surface subsequent stems are quickly deposited and wait for another nucleation step to take place (figure 1.7(a)). In this case the nucleation is the rate controlling step. This results in the growth rate being [39, 35]

$$G_I = b_0 i L_p \tag{1.19}$$

where L_p is the persistence length [40, 41]. Since i is defined as the nucleation rate per unit substrate length, the nucleation rate is iL_p. The L_p used to be called the crystal size, however, it changed due to the fact that this implied that wide crystals would grow faster, and this went against experimental observations that the crystal growth is independent of the crystal size.

Another regime is one taking place at moderate temperatures. Here the rate at which new nuclei are deposited and the rate at which the growth spreads at the surfaces created by nuclei are comparable (figure 1.7(b)). The growth rate then only depends on the two [42],

$$G_{II} = b_0 \sqrt{ig} \tag{1.20}$$

At low temperatures when $i >> g$, nuclei are deposited multiple times within a short space of time and the spreading rate becomes insignificant (figure 1.7(c)). This is normally called regime III [42]. The growth rate becomes similar to the first but with $L_p{}'$ now representing the distance between two nuclei.

$$G_{III} = b_0 i L_p{}' \tag{1.21}$$

The determined values of the rates from equation 1.16-1.18 were then used to find the values of i and g, and by extension the value of G in the different temperature regions. The flux (S(l)) of crystals grown with length l due to nucleation and growth spread was determined to be,

$$S(l) = N_0 A_0 (1 - B/A) \tag{1.22}$$

Where N_0 is the number of crystals growing with lamella of thickness l, and $N_0 A_0$ as the barrier term and $(1 - B/A)$ as the driving force. g was readily determined from the flux as,

$$g = a_0 A (1 - B/A) \tag{1.23}$$

However, i is found from the total flux of stems , S_T, through the barrier, found by integrating over stems of all lengths,

$$S_T = \int_{2\sigma_r/\Delta G_f}^{\infty} S(l) dl \tag{1.24}$$

$$i = S_T / Lp \tag{1.25}$$

The LH theory does a good job of predicting the growth rate as a function of the undercooling, as well as the regime behaviour, however, it presents with several shortcomings as well [43, 44, 45, 46]. Initially the rates were to be determined by apportioning, that is, dividing the free energy available to the different rates, and the apportioning factor ψ can be between 0 and 1. It has been observed that if the apportioning factor is greater than 0 then at some specific temperature lamella of infinite length could grow without any energy barrier. This result has never seen experimentally and is unphysical as the energy barrier increases with the length of the stem. One of the ways around this so called δl catastrophe, was to use the apportioning factor equal to 0 and as was done by Hoffman [47].

The LH theory assumes nucleation occurs on smooth surfaces, yet experimental observations reveal crystals with curved edges in both solution and melt, challenging its applicability under certain conditions [48, 49]. This inconsistency undermines a core assumption of the theory. Another of the limitations associated with the LH theory is that no other chain can grow until one chain has been fully attached or removed from the growth front. And because of the size of the barrier that the initial stem needs to overcome, it can take a long time for this to happen. This shows a defect in the theory because we could be waiting for a long time before

the attachment is complete. There have been several developments of the theory to try and address its limitations, however, it seems that any theory adapted from the assumptions of the original model make it difficult.

1.3.9 Sadler - Gilmer Theory

As previously discussed, the LH theory is built off the idea that crystallisation takes place on a smooth surface and thus the barrier comes from creating new clean surfaces from depositing a stem on the existing surface. At sufficiently high temperatures crystals may be rough and when new stems are deposited they fill the gaps created by the roughness, instead of creating new surfaces. This would imply that as there are no new surfaces there is no barrier per the LH theory. This is contrary to experimental observations that show that there is still nucleation at these higher temperatures. To address this inconsistency, it was proposed that an entropic barrier would be better suited to explain the observations. Point [43] theorised that stems could have more choices on being deposited rather than in the previous theory. From this idea came the birth of the Sadler – Gilmer (SG) theory.

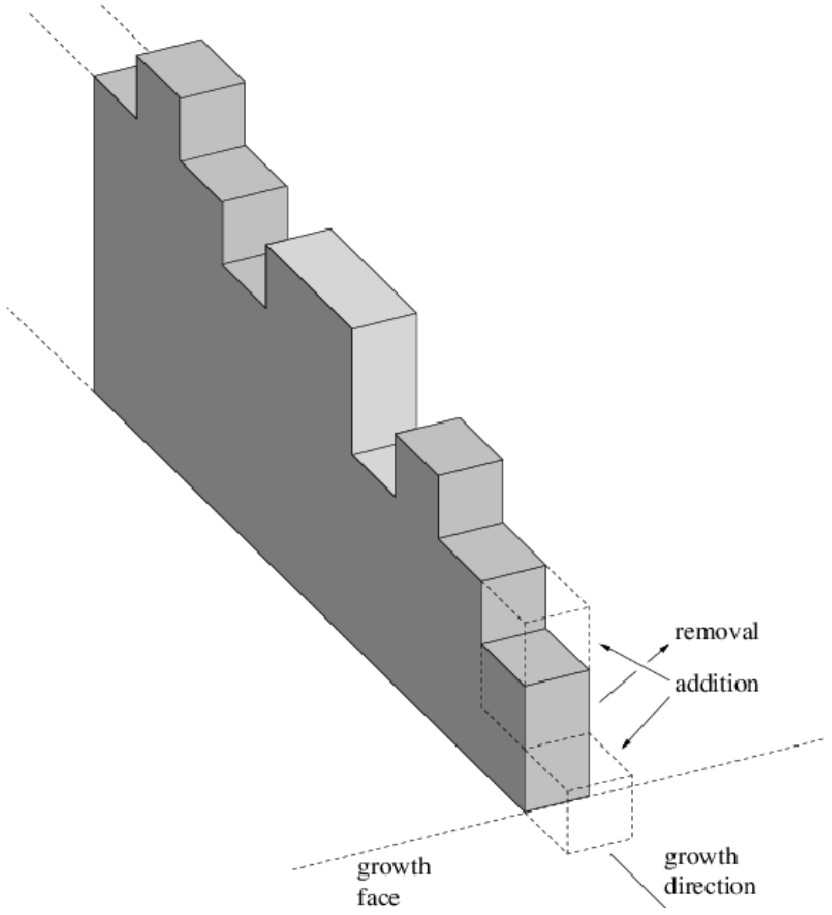

Figure 1.8: A schematic diagram shows a two-dimensional cross-section of a lamella polymer crystal, which serves as the foundation for the two-dimensional version of the Sadler-Gilmer model. The model allows for three possible configuration changes, shown with dashed lines. Taken from [50]

The SG adopts the same concept that Point suggested that a chain being deposited can take a range of different conformations [43]. By doing so it is possible for one of the subsequent stems of a chain to take on wrong conformations. This would prevent the further deposition of the other stems of the chain and thus stop the growth, leading to was they called pinning, and to keep the growth going the wrong stem must be removed [51, 44]. By definition, any step that limits crystal growth would be considered a barrier and, in this case, it is the removal of these wrong conformed stems [51, 44, 52] (figure 1.8). The barrier to nucleation was taken to be purely entropic and for enthalpic considerations to have no effect. The driving force was still taken to be the difference in free energy between crystal and the amorphous and is proportional to the lamellar thickness. As the barrier originates from deposition of the wrong stems, the probability of such stems would increase with thicker lamella as there are more configurations. This then means that the lamellar thickness is dependent on both the driving force and the

barrier and thus the two compete for an optimum thickness [51]. The growth rate from the model was found to be,

$$G \propto \exp\left(-Kl\right)(l - l_{min})\Delta\Phi_c/(kT) \tag{1.26}$$

where $\Delta\Phi_c$ is the change in free energy of crystallisation and k is the Boltzmann's constant, T is the temperature, and K is a constant [38].

It is worth highlighting that though the SG and LH theories present models with differing barriers, they both have somewhat similar growth rate that predict similar growths of crystals and lamellar thickness. However, while the LH theory produces an analytical model, the SG theory does not and is achieved by simulation. This is because it takes into account the different configuration that the stem can take. Several authors [53, 54, 55] have attempted to create unified models as they believe the SG theory is complimentary to the LH as the change in free energy has both enthalpic and entropic contributions. Doye and Frenkel [53, 54] suggested a model where the nucleus was made of several stems instead of one. The thickness of the layer would then be resultant from a convergence process related to the entropy,instead of being controlled by the nucleus.

1.3.10 Growth Rate Minimum

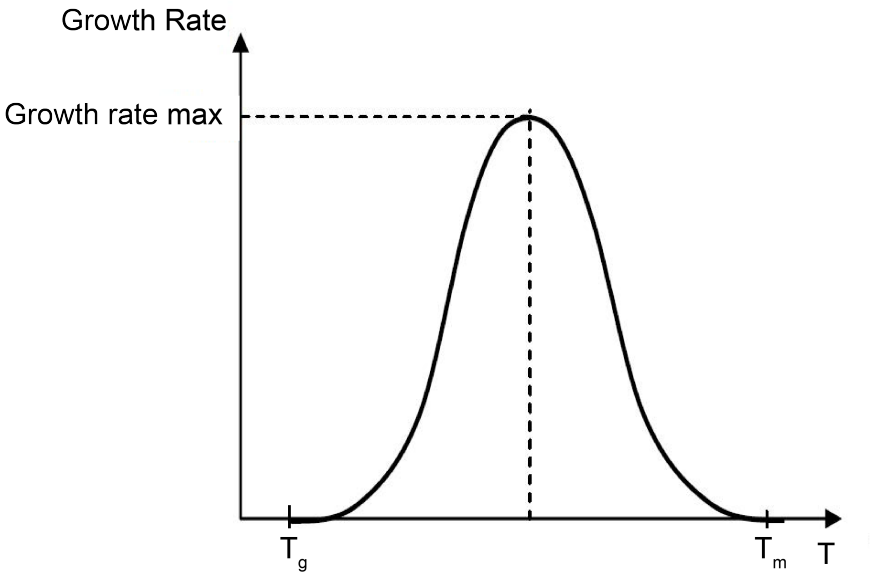

Figure 1.9: Typical growth rate of polymers. The growth rate increases with supercooling until it reaches a maximum and the decreases due to loss of mobility as it approaches glass temperature (T_g).

According to the LH theory, the growth rate G of polymer crystals increase with supercooling to a point, and then starts to go down as is shown in figure 1.9. This results in a characteristic bell-shaped curve. This decline is due to the decrease in molecular mobility near the glass transition, leading to a reduced growth rate.

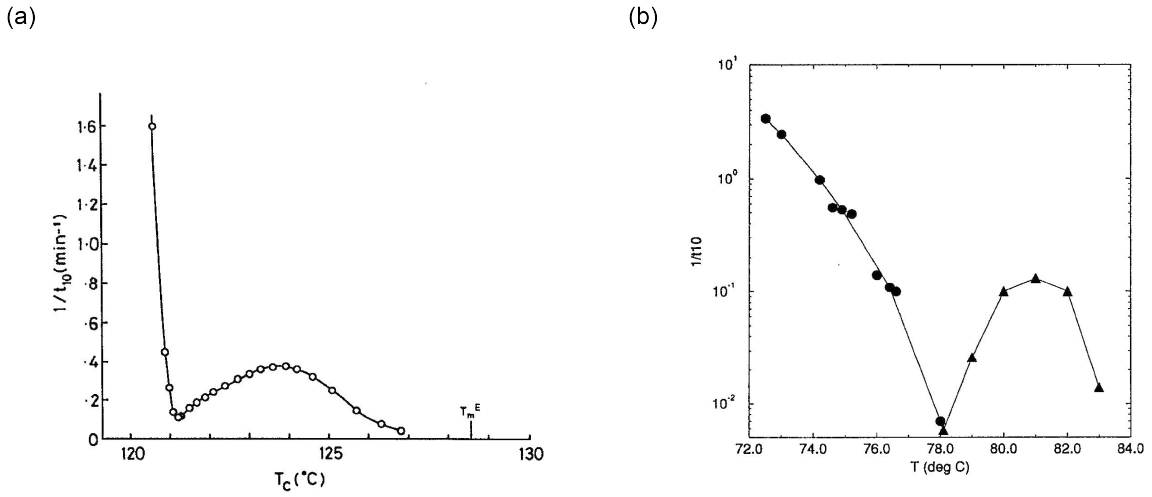

Figure 1.10: The growth rate for $C_{246}H_{494}$ and $C_{198}H_{396}$ showing a minimum as a function of supercooling. (a) The growth rate for $C_{246}H_{494}$ and (b) the growth rate for $C_{198}H_{396}$. t_{10} is the time to taken release 10% of the heat during crystallisation.Taken from [56], [57]

In an experiment involving pure long n-alkanes used to study the early stages of chain folding, it was found that the chains may fold only if they had more than 150 carbons in the backbone. The data from the Raman, small-angle X-ray and electron microscope [58, 56, 57] showed that in these polymers the chains are either fully extended or grow as fold into integer fractions of the original length. As well as this, it was found that the crystallisation rates of melt grown $C_{198}H_{396}$ and $C_{246}H_{494}$ as a function of the temperature, as calculated from the differential scanning calorimetry (DSC), had a minima. The crystallisation rate was seen to initially increase as the temperature was lowered until a certain temperature whereat it began to decrease to a nonzero minimum as the temperature is further lowered, like it shows in figure 1.10. The crystallisation rate then picks up again and increases with supercooling. It is worth pointing out that this minimum occurs at higher temperature than T_g, therefore this result cannot be attributed to the glass transition. This result was inexplicable by the LH theory as it did not predict any minima in the growth.

The idea of surface polymer growth rate poisoning by impurities was a well-known subject by the time of discovery [59]. However, in this case it was ruled out as the sample was extremely pure. Instead, it was proposed that the extended chains growing at the higher temperature ranges are poisoned by the growth of the once folded chains, and this phenomenon was termed self-poisoning [58]. Initially the extended chains grow as found by the SAXS and DSC, however their growth is blocked by the folded chains [60]. Though they are not stable above their own melting point, it takes time for them to detach, thus slowing down the growth. The same phenomenon was found in solution grown $C_{198}H_{396}$. Similar results have been observed in the studies of lamellar thickening carried out on low molecular weight fractions of poly (ethylene oxide) [61]. The minimum observed was not as well defined as that seen for the long n-alkanes,

however, republication of the data showed that the growth of the extended chains slowed down near where the kink was in the growth rate, which implied self-poisoning.

Current polymer crystallisation theories vary in their ability to reproduce the growth rate minima, and such attempts are important in evaluating the assumptions made in such theories. Classic coarse-grain Lauritzen-Hoffman (LH) theory could not reproduce them without some strained assumptions [62], mostly because of its failure to take into account properly the self-poisoning effect, where polymer chains at growth front are trapped in futile conformations slowing-down crystal growth. Fine grain models such as Sadler's roughness-pinning theory could generate the growth rate minima naturally and qualitatively [63], but have a problem to explain the smooth crystal surfaces observed in many polymers showing growth rate minimum. Monte Carlo simulation based on segmented polymer chains was also able to show the minima, even though less pronounced than in real alkane systems [64]. Based on mean-field theory and computer simulation it was argued that self-poisoning is ubiquitous, as long as a molecule can bind in two (or more) energetically non-equivalent ways to a crystal, and their binding probability is sufficiently different [65].

1.3.11 Higgs – Ungar Model

Higgs and Ungar (HU) developed a model that was able to semi-quantitatively explain the growth rate minimum at the transition between extended and once-folded forms of long chain n-alkanes [60]. The model is based on a simplified version of the SG row model. Though the latter does show a minimum in the growth rate, the former is analytically soluble. The HU model is developed on the assumption that the once-folded form can be deposited on the extended form but the reverse is not possible. Because of this assumption, the extended form surface can readily has several m once-folded chains.

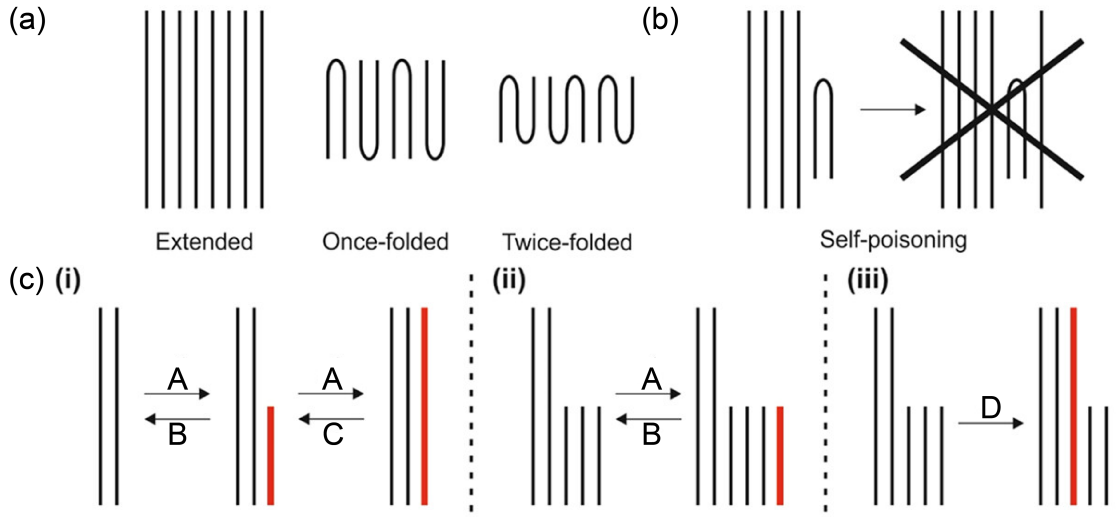

Figure 1.11: A diagram of the HU model. (a) The chains fold precisely into two or three segments, forming tight chain folds, with the chain ends consistently located at the crystalline layer surfaces. (b) The growth of the extended chain form is hindered by the frequent deposition of unstable, once-folded chains at the growth interface, which blocks further extension and attachment of additional chains. (c) An earlier model for the growth of the extended-chain form with self-poisoning. By allowing the crystallisation of covered half-crystallised stems at the growth front to the extended form, then it is possible to obtain a non-zero minimum growth rate when D $<$ A. Taken from [56], [66]

The model also assumes that the extended form grows at the growth front by two consecutive steps. The first step sees attachment of a half-crystallised stem at the growth front with attachment rate A and an associated detachment rate of B. The second step involves attachment of a second half of the stem to create the extended form stem at the same rate A, a fully extended stem can revert to the half-crystallised stem by rate C. The dynamics are presented in figure 1.11(c)(i). It was assumed that the change in free energy for the deposition of the first half stem was,

$$\Delta\Phi_1 = -\frac{\epsilon}{2} + \frac{\Delta STl}{2} + \sigma_e \tag{1.27}$$

Where ϵ is the energy that each monomer gains due to the attractive forces between the chains, ΔS is the loss in entropy associated with the loss of mobility of the chain, σ_e is the energy from crowding of the ends of the chains and the chain folds, with T at the temperature, and l as the length of the fully extended stem segment. Attachment of the second half-crystallised stem was assumed to have a free energy change of,

$$\Delta\Phi_2 = -\frac{\epsilon}{2} + \frac{\Delta STl}{2} \tag{1.28}$$

Where the variables still mean the same thing, however here there is no overall new surfaces created hence the absence of the σ_e. The growth rate of the once folded form, V_{fold}, would then be the difference between the rate of the half-crystallised stems being deposited, A, and their detachment rate, B,

$$V_{fold} = A - B \tag{1.29}$$

The growth rate of the extended form (V_{ext}) was found to the difference between the rate of deposition of the second half-crystallised stem leading to the extended form, AP_1 and the number of extending form reverting to the half-crystallised, CP_0,

$$V_{ext} = AP_1 - CP_0 \tag{1.30}$$

Where P_0 is the probability of having a surface with 0 half-crystallised stems, and P_1 is the probability of having a surface with 1 half-crystallised stem. Here P_m represent the probability of having m half-crystallised stems at the growth front. By constructing and combining differential equations for the change of these probabilities, and the fact that $\sum_{m=0} P_m = 1$, they were able to obtain P_0 and P_1 in terms of the rates as,

$$P_0 = \frac{(A+B)(1-A/B)}{(A+B)(1-A/B)+A+C} \tag{1.31}$$

$$P_1 = \frac{(A+C)(1-A/B)}{(A+B)(1-A/B)+A+C} \tag{1.32}$$

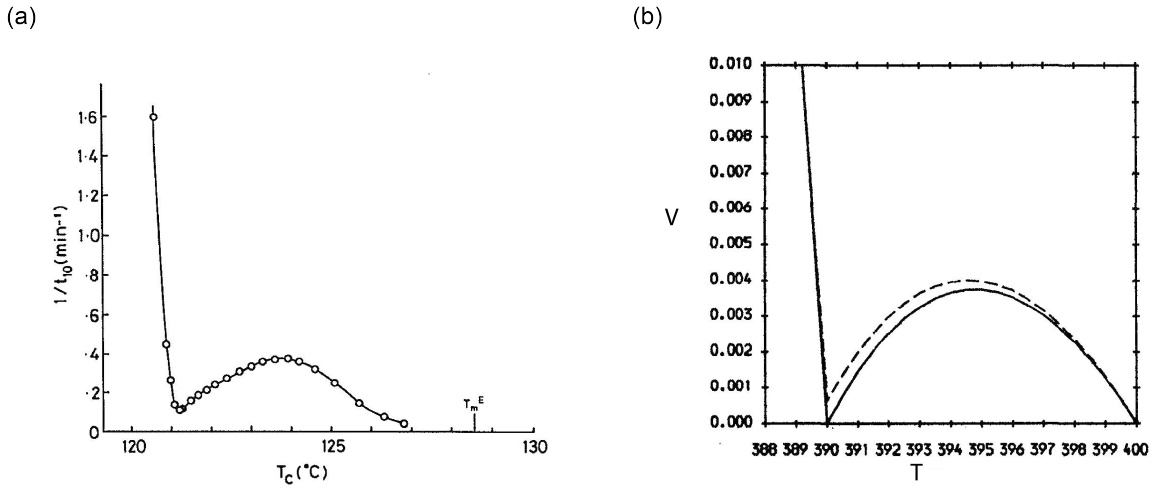

Figure 1.12: The crystallisation rate as a function of temperature (K) of $C_{246}H_{494}$ compared with that generated from the HU model. (a) Growth rate of $C_{246}H_{494}$. (b) Crystallisation rate from the HU model. By using apportioning with $A = 1$, the HU model generated a minimum in the crystallisation rate. The dashed line shows that using a small value of $f = 0.005$ a non-zero minimum can be obtained by allowing crystallisation of covered chains. Adapted from [60] and [57]

Above the melting point of the once-folded form, a half-crystallised stem at the growth rate is not stable as $B > A$ while the fully extended stem is stable as $A > C$. This means that the extended form grows above the melting point of the once-folded form, T_2. As the temperature approaches T_2, A grows and the number of half-crystallised stems arriving at the growth front increases. As the extended stem can grow only when such additional half-chains are removed, this poisons their growth and by the model the growth would drop to zero. In the observed experimental results figure 1.12(a), the growth does not drop all the way to zero but is rather a non-zero value. To account for this, it was suggested that inclusion of a conversion rate D for covered half-crystallised stems near the extended form growth front would yield the observed results, as seen by the dashed line not dropping all the zero in figure 1.12(b). D was defined such that $D = f$, where f is a number small than 1.

1.3.12 Two Minima in Crystallisation Rate of Poly(ethylene Brassylate)

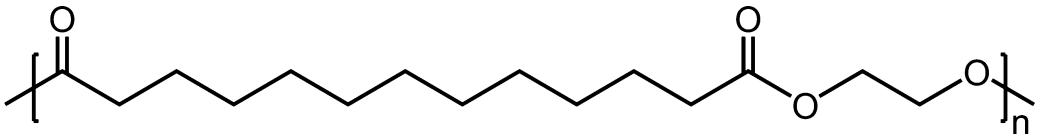

Figure 1.13: Poly(ethylene brassylate) molecule.

It is possible to design materials with specific properties by choosing the right microstructure and processing methods. One way to understand this is to synthesise and study polyethylene-inspired polymer models with regularly spaced moieties substituted into the structure. An example of such polymers is poly(ethylene brassylate) (PEB). PEB can be synthesised from the ring-opening of ethylene brassylate [67]. Its repeating unit contains eleven methyl groups sandwiched by ester groups at the ends, as shown in figure 1.13 [68]. PEB is biodegradable and biocompatible which makes it a potential candidate for medicine and drug delivery.

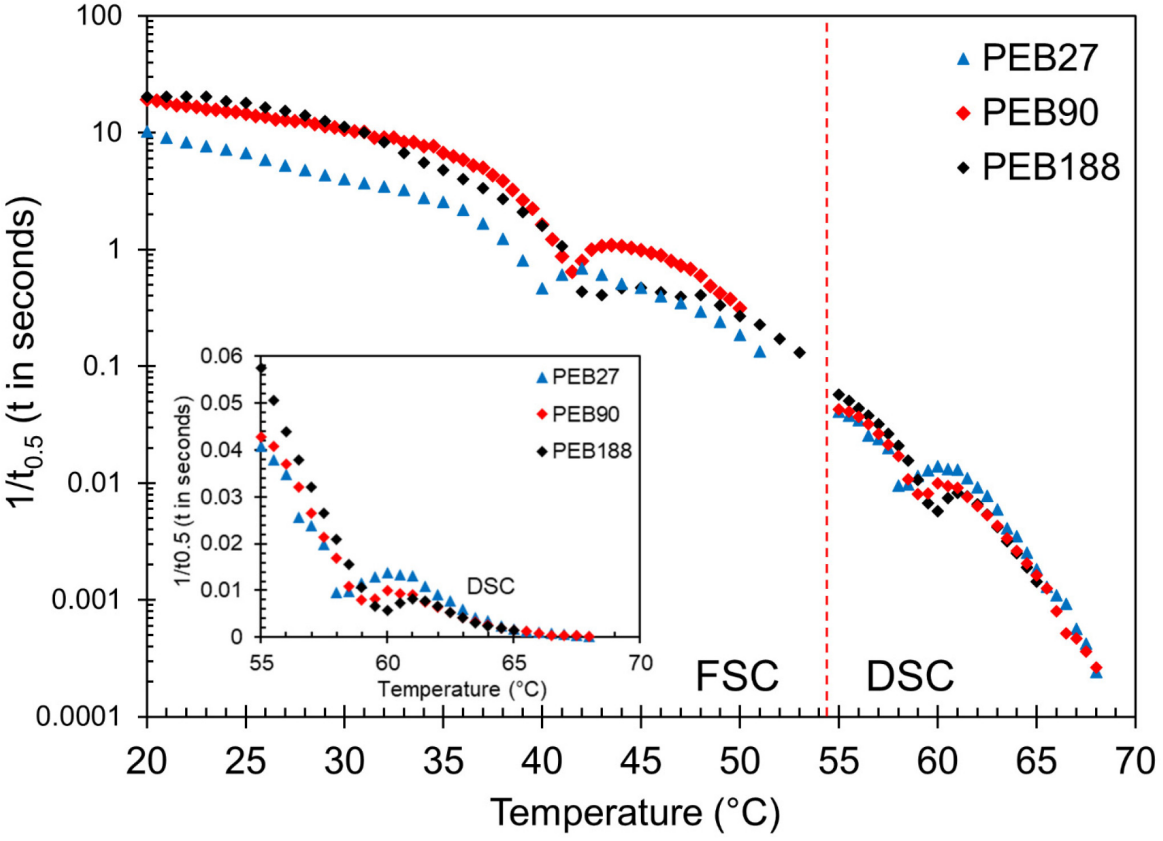

Figure 1.14: The crystallisation rate from the inverse of the exothermic peak crystallisation time vs crystallisation temperature for PEB27, PEB90 and PEB188. The higher temperature data was obtained by conventional DSC while the lower temperature data was collected by FSC, with the red dashed line separating the two regions. The vertical dashed line demarcates data obtained by conventional DSC and data obtained via fast scanning calorimetry (FSC). The inset shows a blown up picture of the crystallisation rate minimum at high-temperatures in Cartesian coordinates. From [68].

Recently Marxsen et al [68] studied the isothermal crystallisation kinetics of PEB from melt to better understand and predict the critical processing parameters for semicrystalline biopolymers. In the study PEBs with average molar mass of 26.9, 89.9 and 188.1 kg/mol were stud-

ied with differential scanning calorimetry (DSC) at higher temperatures, and fast scanning calorimetry (FSC) at lower temperatures. The polymers are herein referred to as PEB27, PEB90, and PEB188 according to their average molar mass to the nearest whole number. The most surprising result from the study was the observation of two minima in the overall crystallisation rate of the three PEB polymers (figure 1.14).

These minima occurred at temperatures where the average lamellar spacing increased by one repeating unit of the polymer chain. It was deduced that this change was due to the quantised change in the crystalline thickness. Analysis of the atomic-level order via the Wide Angle X-ray Scattering (WAXS) confirmed the same crystal structure at all temperatures. The authors of the paper thus deduced that the unusual behaviour is equivalent to the quantised self-poisoning phenomenon in long chain n-alkanes and low molecular weight PEO fractions. The minimum at higher temperatures is from the growth of the form with lamellar thickness of four repeating units (herein referred to as the F_4 form) being poisoned by the form with lamellar thickness of three repeating units (F_3 form). Whilst the minimum at at lower temperatures is due to the growth of the F_3 form being poisoned by the growth of form with lamellar thickness of two repeating units (F_2).

In Chapter 3 of this thesis, an analytical one-dimensional (1D) model for self-poisoning due to quantised lamella thickness is developed from the 1D Higgs-Ungar (HU) model for long chain n-alkanes. The model is then parameterised to fit the experimental results of PEB.

1.3.13 Growth Rate Minimum in Poly(ethylene Bromine)

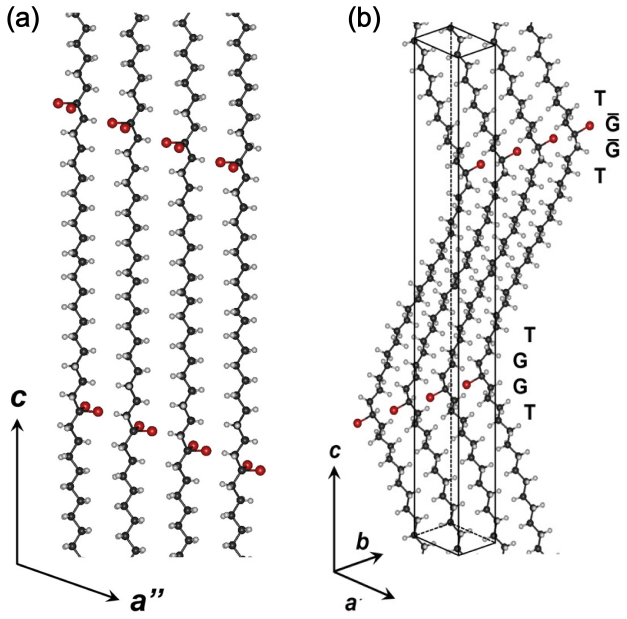

Figure 1.15: Crystal structure model of PE21Br form I and II crystal obtained by energy minimisation. (a) The polymer chains in form I are planar zig-zagging at every carbon, similar to the conventional polyethylene structure. The bromines are embedded within the bulk of the crystal. (b) Form II chains bend at the carbons with the bromine and in between the chain is linear. The bromines stick out at the bends and are aligned. Courtesy of [69]

Another example of polyethylene-inspired polymers are the halogen substituted polyethylene precision polymers. Here a hydrogen atom is replaced by a halogen every m methylene groups [70, 71, 72, 73, 74]. A key characteristic of these polymers is that they crystallise forming two distinct crystals structures, Form I and Form II. Form I is observed when cooling the melt at faster rates. Its chains have an all-trans planar conformation (figure 1.15(a)) and it was found to be less stable than Form II [69, 75]. Form II is observed at slower cooling rates and its chains favour a zigzagged structure, where an all-trans configuration occurs along the m long methyl group and the bends at the carbon with a bromine [69, 75] (figure 1.15(b)). The melting point of Form I is lower than that of Form II and upon heating above this melting point, Form I melts and recrystallises to Form II.

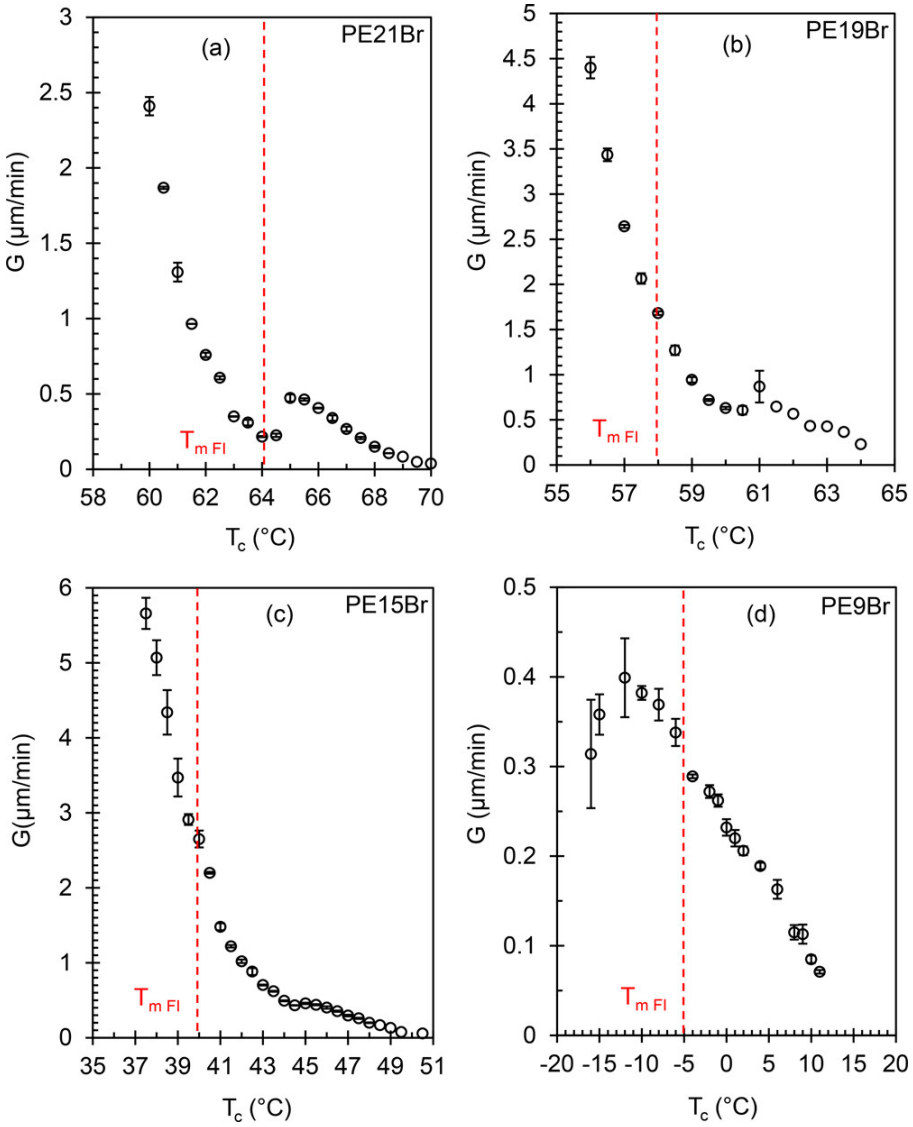

Figure 1.16: Linear spherulitic growth rates of Form II as a function of crystallisation temperature. Experimental results are shown by the open circles and error bars are added. (a) PEBr21 shows the most pronounced minimum, followed by (b) PEBr19, then (c) PEBr15, while (d) PEBr9 does not show any poisoning. The melting temperature of Form I is shown by the red dashed lines, the melting temperature gets closer to the rate minimum as the spacing between the carbons with the bromine increases. Taken from [75]

In a research by Zhang et al [75], four samples of such precision polymers with bromine replacing a Hydrogen every m= 9, 15, 19 and 21 methylene groups were studied. The poly(ethylene bromine) (PEBr) polymers were named PEBr9, PEBr15, PEBr19 and PEBr21 according to the number of carbons between the bromines. The investigation of the isothermal linear spherulitic growth rates with decreasing temperature of Form II under an optical microscope revealed a

minimum near the melting point of Form I (figure 1.16). The authors of the research concluded that the observed minimum was due to self-poisoning. They suggested that the growth of Form II was poisoned by that of Form I.

What makes the self-poisoning in PEBr peculiar is that Form II was observed to grow both above and below the minimum. In other known cases of self-poisoning [58, 52, 68] the more stable form grows above the poisoning and the less stable form grows below the poisoning. Zhang et al [75] also investigated the possibility that Form I may have grown below the poisoning point and subsequently been converted to Form II later. However, it was found that no solid-solid transition took place from Form I to Form II, and in fact Form I converts to Form II upon heating through melt and recrystallisation.

An alternative approach to this problem is to assume that the observed poisoning is due to two forms of the Form II that have different lamella thickness, as with poly(ethylene brassylate) and the long chains n-alkanes. Chapter 4 of this thesis is dedicated to exploring the differences between a model of self-poisoning due quantised lamellar thickness and that self-poisoning of Form II growth by Form I.

1.3.14 Poisoning of Stereocomplex crystallisation by Homochiral Poly-lactic acid

A stereocomplex (SC) is a structure formed when two molecules that are mirror images of each other, enantiomers, combine in a complementary arrangement. A mixture containing equal numbers of left- and right-handed enantiomers is known as a racemic mixture, or simply a racemate. SC crystals are considered beneficial for improving properties of the homochiral crystal (HC) polymers, such as the heat resistance and mechanical properties. A notable example is poly(lactic acid) (PLA), where the SC form has a higher melting temperature (230°C) compared to its HC polymers (below 175°C), poly(l-lactic acid) (PLLA) and poly(d-lactic acid) (PDLA). This higher stability makes SC-PLA highly desirable for enhancing mechanical and thermal properties in biodegradable applications [76, 77, 78, 79].

When a 1:1 mix of high-molecular-weight PLLA and PDLA (molecular-weight $\geq 4 \times 10^4$ g/mol) is crystallised at high temperatures ($\sim$ 180°C), SC crystallisation tends to halt, with HC forming upon further cooling [80, 81]. Early studies suggested that microscopic phase separation might increase HC formation, but this was later refuted [82, 83]. He et al. [84] found that increased molecular weight reduces SC formation by causing same-chain clustering, which suppresses SC nucleation.

Recently, Cui et al. [85] investigated SC crystallisation in high-molecular-weight and low-molecular-weight PLLA/PDLA racemates using DSC, optical microscopy, and X-ray scattering. For low-molecular-weight, DSC showed single peaks above 200°C for both cooling and heating, indicating SC formation. In high-molecular-weight racemates, the DSC cooling curves showed distinct behaviours based on the seeding temperature (T_s). Above 230°C, SC crystallised be-

tween 225°C and 140°C, while HC crystallised around 130°C. Higher T_s resulted in slower SC crystallisation and more prominent HC crystallisation, confirmed by two melting peaks at $\sim$ 230°C (SC) and $\sim$ 170°C (HC). Notably, slower cooling rates increased SC crystallinity, showing that slower cooling favours SC formation over HC.

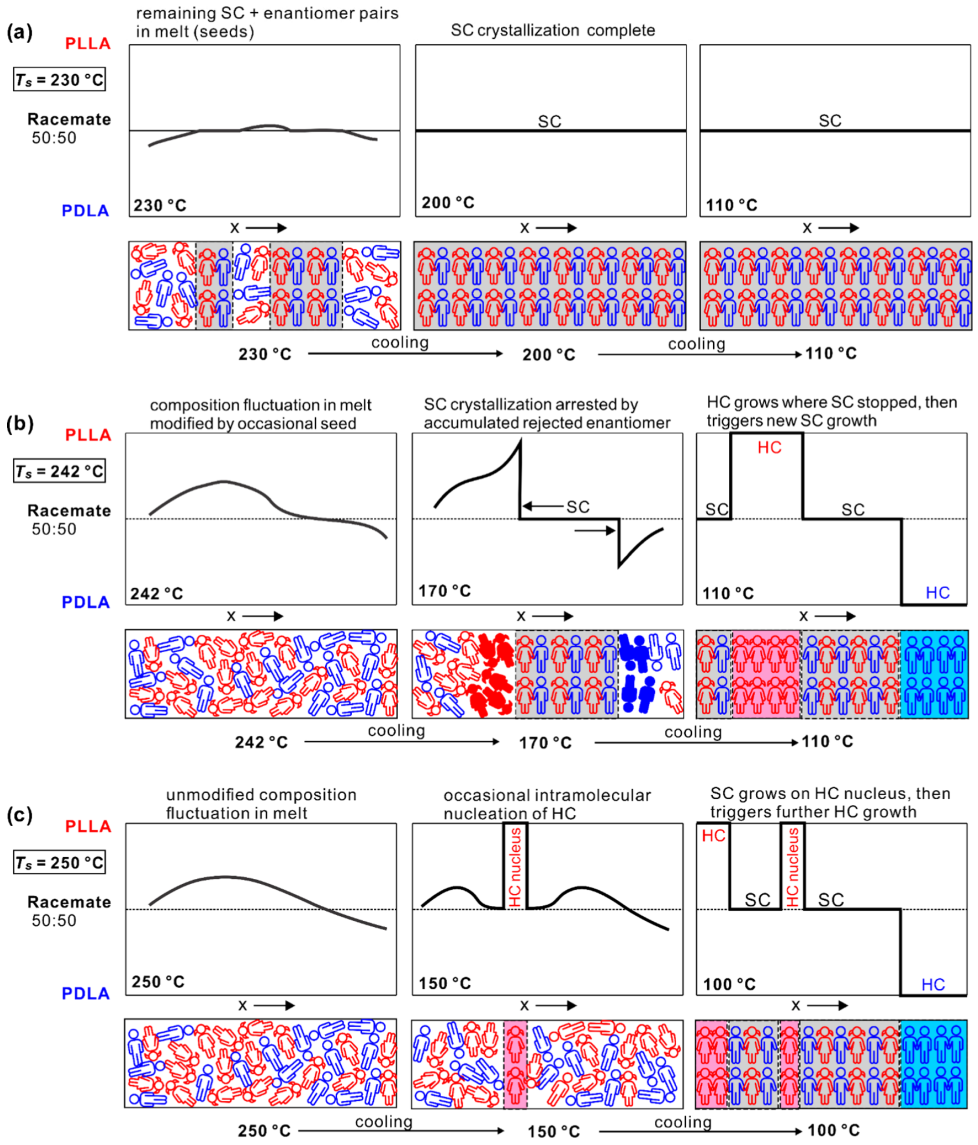

Figure 1.17: Diagram illustrating the processes occurring during the cooling of high molecular weight PLLA/PDLA racemate after brief annealing at three distinct annealing temperatures (T_s). In each subfigure, the top row depicts the spatial variation of enantiomer ratios at specific temperatures, while the bottom row illustrates the molecular configuration, with "boys" and "girls" representing PDLA and PLLA molecular segments, respectively. (a) For $T_s = 230\,°C$, SC crystallisation proceeds smoothly as the melt remains well-mixed with minimal compositional variability. Residual seeds promote continued SC growth upon cooling to 200 °C and 110 °C. (b) At $T_s = 242°C$, pronounced compositional fluctuations in the melt create an excess of one enantiomer (indicated by filled symbols), which accumulates at the SC growth front and halts further crystallisation. Homochiral (HC) domains emerge in these regions, triggering HC growth at lower temperatures (110 °C). (c) When $T_s = 250\,°C$, compositional fluctuations remain unaltered, and sporadic intramolecular nucleation of HC domains disrupts SC crystallisation. HC crystallisation becomes the dominant process as cooling progresses. Taken from [85]

Cui et al. offered a qualitative explanation for the observation, drawing similarities to the self-poisoning in the long chain n-alkanes, PEO, PEBr and PEB. They suggested that at low T_s values there are still some remaining crystallites in the melt and this reduces the fluctuations at in the enantiomer concentrations (figure 1.17(a)). But as the T_s is increased the seeds melt away and there is enantiomer build up ahead of the SC crystal (figure 1.17(b)). At high temperatures all the seeds have melted away and the SC growth is highly suppressed (figure 1.17(c)). The growth of SC is controlled by the diffusion. In Chapter 6 of this thesis a lattice Monte Carlo dynamics simulation is carried out to investigate the crystallisation of PLA SC and the poisoning by purity.

1.4 Chiral Polymers and Liquid Crystals

1.4.1 Chirality

Chirality is an intrinsic property of a lot of polymers and liquid crystals. It leads to the development of interesting structures and self-organisation of these polymers. An object is said to be chiral if it has a broken mirror symmetry, that is, if its mirror image cannot be superimposed on it. Chirality may arise in a polymer either by having a chiral centre or by axial chirality. A molecule is said to have a chiral centre if it has a central atom that is bonded to four different groups, and there are different arrangements of the groups in space around the central atom that are not superimposable, as show in figure 1.18, [86, 87]. Axial chirality is where an object winds into a helix along an axis [87].

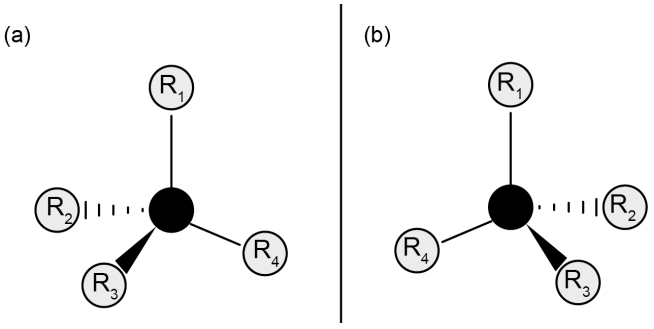

Figure 1.18: The figure shows two molecules that have the same molecular formula and sequence of bonded atoms, but have different orientations in three-dimensional space. The molecules are called enantiomers and are not superimposable. The central atom is the chiral centre and has 4 distinct groups attached to it.

This section of the introduces chirality in polymers and liquid crystals. It starts off by giving a brief review of some of the helical structures that arise in biopolymers and polymer crystals

and how these lead to different packing in space. Liquid crystals are then introduced and and how chirality in different phases of liquid crystals influences packing.

1.4.2 Biopolymers

Biopolymers are polymers that are produced and found in cells of living things [86, 88]. They are made up of monomers covalently bonded to give rise to larger molecules. There are three main classes of biopolymers that are classified according to the monomers they are made from and these are polynucleotides, polysaccharides, and polypeptides.

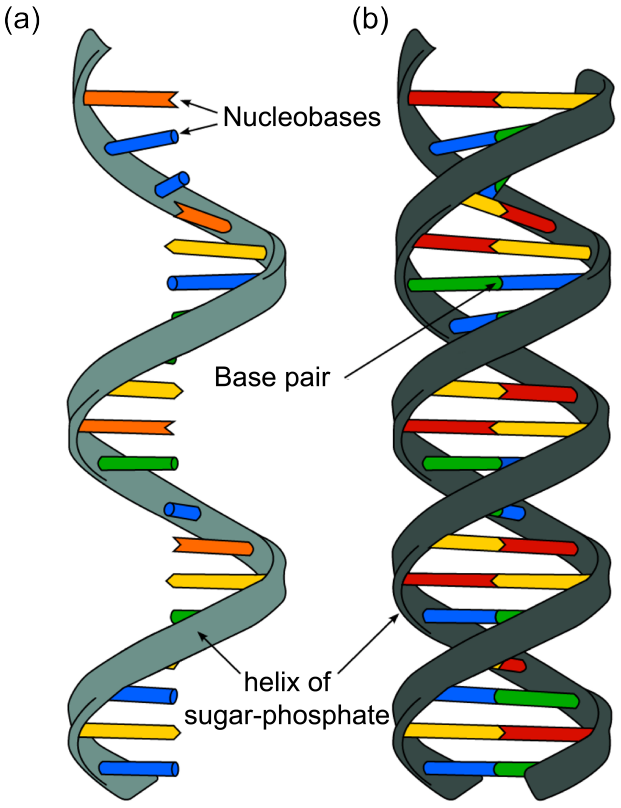

Figure 1.19: RNA and DNA molecules. (a) Single strand RNA and (b) DNA double helix . From [89].

The two most studied biopolymers are deoxyribonucleic acid (DNA) and ribose nucleic acid (RNA) [90] (figure 1.19). DNA stores genetic information, serving as the blueprint for an organism's development and function, while RNA transfers and interprets this information to synthesise proteins essential for cellular processes. They are both made up of nucleotides, which consist of a 5-carbon sugar, deoxyribose in DNA and ribose in RNA, a phosphate group and one of four nucleobases. The nucleotides have chiral centres, making DNA and RNA chiral.

A key characteristic of biopolymers that are chiral is internal molecular conformation. These molecules interact with themselves producing certain structures, usually helical in nature. In RNA and DNA, the complementary nucleobases along the strands form hydrogen bonds with each other [86]. This results in RNA winding into a helix (figure 1.19(a)) and DNA into a double helix (figure 1.19(b)).

1.4.3 Polymer Crystal

Segments of polymer chains can become ordered as they fold and align with each other. This process is called crystallisation as mentioned in the last subsection. Polymers can crystallise by being mechanical stretched, by cooling the melt, or by evaporation of a solvent they are dissolved in. The method by which the crystal is obtained can also result in different helical conformation as well as the different structure in the crystals. Most of these polymers crystallise into crystals with chains wound up into helices [91, 92]. Isotactic Poly-1-butene (iPB) and PLA are examples of polymers that crystallise forming helices. These polymers have been well studied because of their wide range of applications.

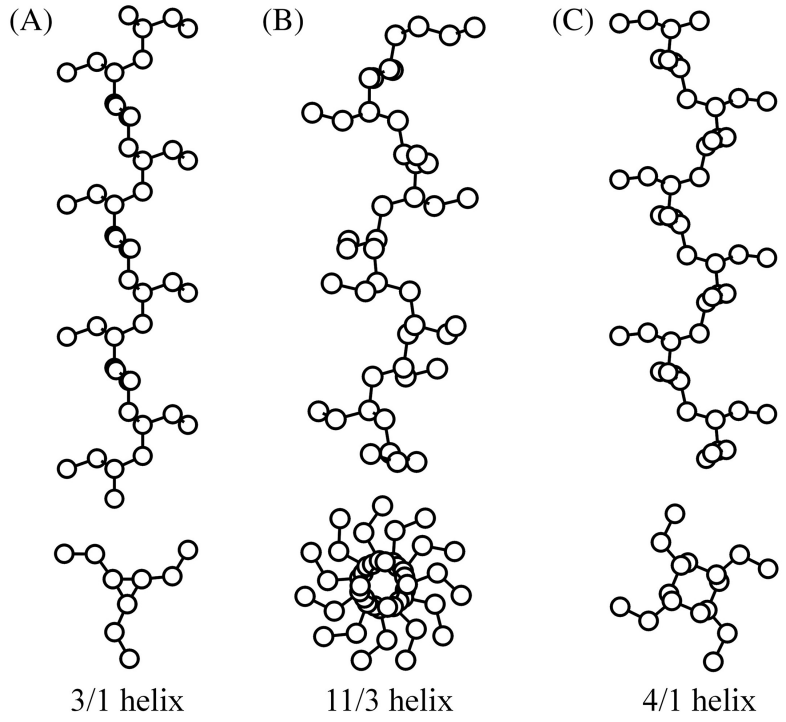

Figure 1.20: The polymorphs of isotactic Poly-1-butene. The planar zigzag of PE is shown on the left. (A) Form I of iPB with a 3/1 conformation, (B) Form II with a 11/3 helical conformation, and (C) Form III with a 4/1 helical conformation. The top pictures show the side view of the helical chains, while he bottom picture is the projection view which is the same as form I of iPP except the branches are ethyl groups not methyl groups. Taken from [93]

.

iPB crystallises into three main crystals forms depending on the conditions as shown in figure 1.20. It crystallises forming trigonal unit cell with both left- and right-handed helices in Form I, with the helices in 3/1 conformation [92, 94]. The conformation means that there are three monomeric units every full turn of the helix. Form II of iPB is obtained from cooling of the melt, and it has 11/3 helical conformation packed into a tetragonal crystalline lattice [92, 94]. Though this form is favoured by melt crystallisation, it is unstable and spontaneously changes to Form I in about 10 days. The third form is obtained from evaporating the solvent. It has 4/1 helices, with two of them packed in an orthorhombic unit cell [92]. This form is also unstable and it transforms into Form I upon drawing.

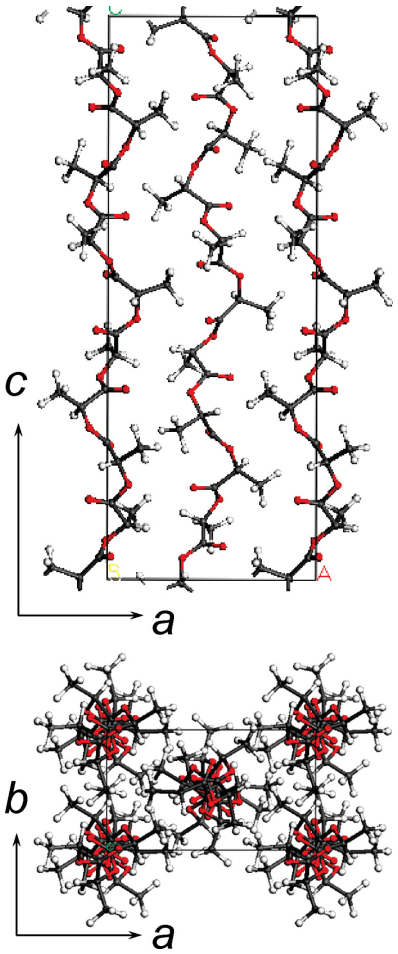

Figure 1.21: Crystal structure of the α-form of PLLA, viewed along the c-axis (top) and a-axis (bottom), showing the 10/3 helical chain conformation in a unit cell. Carbon atoms are shown in black, oxygen atoms in red, and hydrogen atoms in white [95]

.

PLA that was discussed in the previous subsection exhibits various polymorphs, each characterised by distinct helical conformations that impact their structural and mechanical properties. The α-form, the most common polymorph, adopts a 10/3 helical conformation [96, 97]. This is typically formed in PLLA via slow cooling rates or high-temperature annealing (figure 1.21). The δ-form (also know as the α'-form) also has a 10/3 helical structure [98]. It is formed at lower temperatures and lacks the complete ordering seen in the α-form, resulting in lower stability and crystallinity. Upon heating, it transitions into the α-form. The β-form, in contrast, adopts a looser 3/1 helical structure [99, 100]. This form commonly appears under stretching conditions. The γ-form is less well-defined and is thought to adopt a 3/1 helical structure similar to the β-form, though it is even less ordered and less stable [101]. Finally, SC [102], formed from blending PLLA and PDLA chains, consists of an extended 3/1 helical structure, where alternating chirality allows for tightly interlocked packing in an orthorhombic lattice.

This configuration provides the SC with enhanced thermal stability and mechanical strength compared to homopolymer PLA forms.

1.4.4 Liquid Crystals

Liquid crystals are a state of matter that possess properties that are between those of solid crystals and isotropic liquids [87, 103, 104]. Molecules that exhibit liquid crystal characteristics are referred to as mesogens. There is no long-range order in the positions of centres of gravity of molecules [105]. There are two classes of liquid crystals, lyotropic and thermotropic, and these are classified according to how the liquid crystal state is obtained. Lyotropic liquid crystals are obtained by dissolving the crystals in solvent [87, 103, 104]. They often have hydrophilic cores and hydrophobic tails. Thermotropic LCs on the other hand are obtained by heating the crystal. Normally the crystal goes from a crystalline phase to a LC phase then to isotropic liquid upon heating. Sometimes however, it goes through more than one distinguished LC phase before transitioning to an ordinary isotropic liquid crystal. This research is only concerned with thermotropic LCs.

1.4.5 Thermotropic Liquid Crystals

Simple thermotropic liquid crystals (LCs) can be classified as calamitic or discotic [87, 103, 104]. Calamitic LCs consist of rod-like molecules, whereas discotic LCs are composed of disc-like molecules. Typical phases in calamitic LCs include nematic and smectic phases. In nematic phases, the LC molecules exhibit long-range orientational order, meaning that over large distances, the long axes of the molecules are on average aligned in the same direction. This direction is specified by a vector called the director 1.22(a). Smectic phases, on the other hand, exhibit both long-range orientational order and a layered structure, with positional order along one dimension. The molecules in smectic phases can either align parallel to the layer normal or be tilted with respect to it, as shown in figure 1.22(b-c).

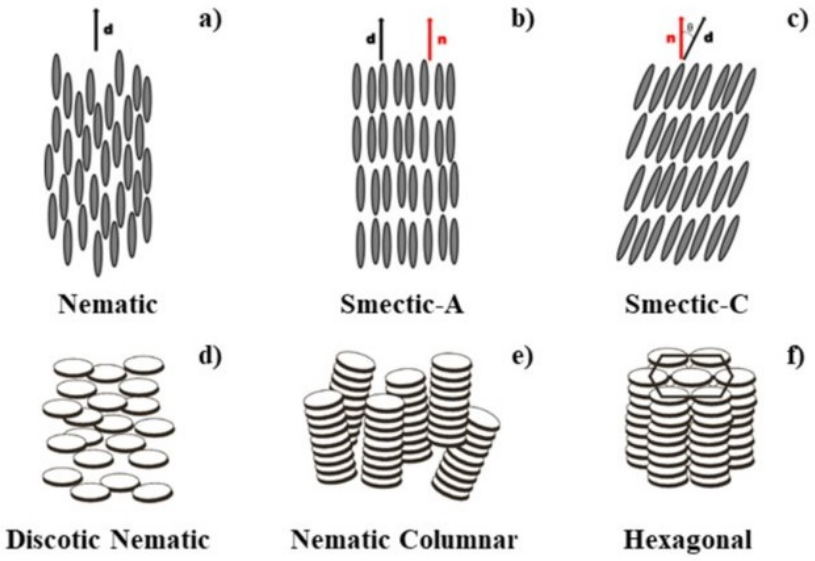

Figure 1.22: Simple thermotropic LC phases. The top row are the calamitic phases, namely the (a) nematic, (b) smectic A, and (c) smectic C. The bottom row are disc-like molecule in (d) nematic, (e) smectic and (f) hexagonal phases. From [106]

Discotic LCs, by contrast, are formed from disc-like molecules with planar cores that allow for stacking interactions [107]. These LCs can form phases similar to the calamitic nematic and smectic phases [103, 104]. In the nematic-like phase of discotic LCs, the short axis of each disc aligns with the director, resulting in the discs lying perpendicular to the director on average 1.22(d). Additionally, discotic LCs can form more highly ordered columnar phases, where the disc-shaped molecules stack into columns 1.22(e-f).

1.4.6 Chirality in Liquid Crystals

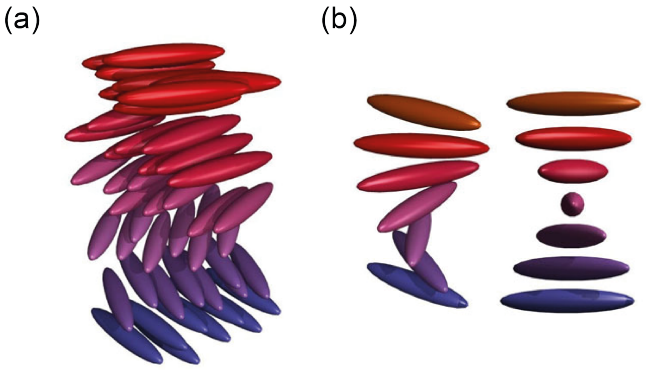

Figure 1.23: Chiral nematic LC. (a) Chiral nematic LC having the director rotated from one layer to the other. (b) Shows the helical rotation of the director well. Taken from [108]

Chirality is observed in certain nematic compounds composed of chiral mesogens. In achiral nematic phases, the director remains uniform across the material. However, in chiral nematic phases, the director undergoes continuous rotation along an axis, forming a helical structure, as shown in Figure 1.23 [103]. This rotation results in a complete 360° twist over a characteristic length known as the pitch. Chirality, however, does not always manifest as a helical structure. In chiral smectic C phases, chirality arises from the tilt of the mesogens relative to the layer normal (figure 1.24). This tilt creates a chiral, non-mirror-symmetric arrangement between the tilt axis and the optical orientation of the mesogens [103]. This type of chirality is also observed in discotic columnar phases, where the plane of each discotic molecule is tilted relative to the central column axis, leading to a chiral arrangement [103].

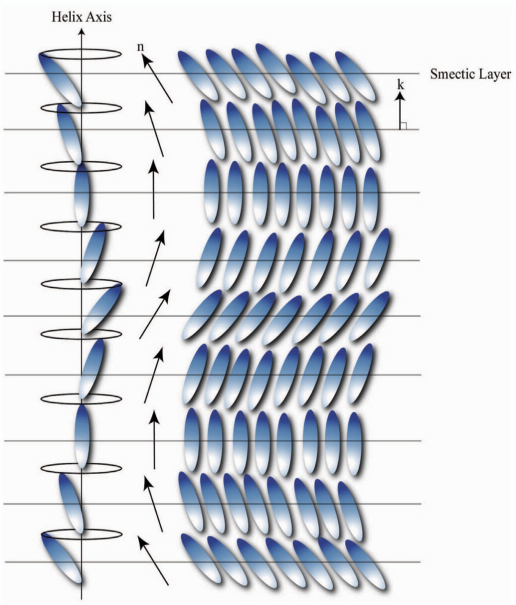

Figure 1.24: Chiral smectic LC. The arrangement of molecules in one pitch of a chiral smectic C phase. The figure also shows the showing the layer planes, the layer normal k, the director n, and the helix axis. Adapted from [109]

Chirality can emerge in LC phases composed of bent-core achiral molecules due to their unique molecular shape. The bent shape disrupts the symmetry typical of rod-like molecules, creating an inherent asymmetry that favours twisted or helical arrangements. This structural asymmetry is amplified by the presence of dipole moments along the molecular arms or at the bend of the molecule, promoting polar interactions that drive the molecules to align in a way that minimises electrostatic repulsions [110, 111].

1.4.7 Bicontinuous Phases

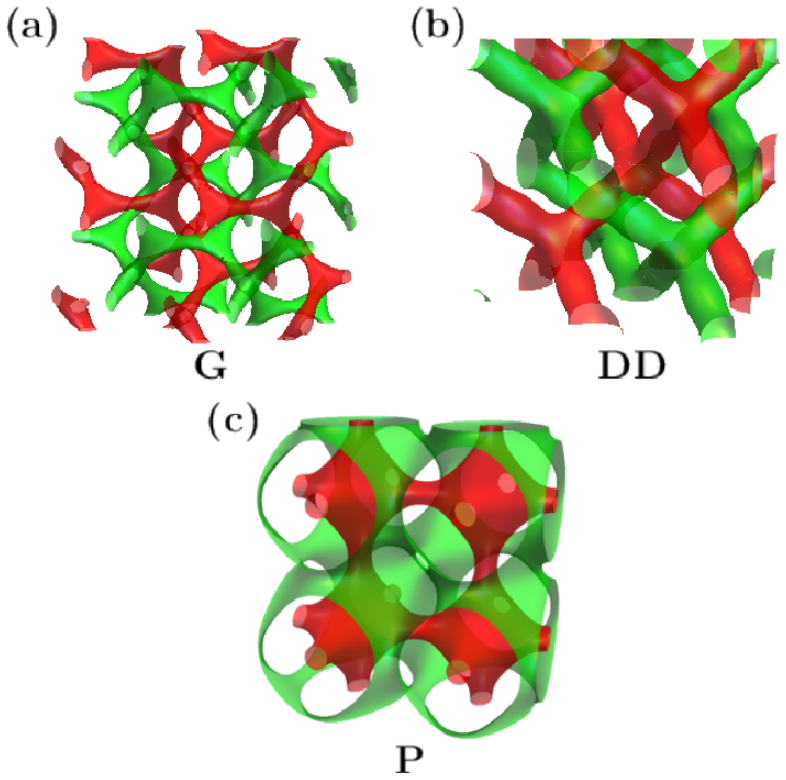

Figure 1.25: The minimal surfaces of the (a) double-gyroid (G) phase, (b) double-diamond (DD) phase, and (c) plumber's nightmare (P) phase. Taken from [112]

Not all liquid crystals form lamellae and columnar phases. Liquid crystals that are formed of molecules with two opposing functional groups, such as hydrophilic and hydrophobic groups in lyotropic LC, tend to form phases where the space occupied by the different groups is separated. In bicontinuous phases, both of these spaces form a continuum [113], [114], [115]. An example of these phases that has attracted the most interest and has been the cubic phases. Three lyotropic cubic phases have been studied in detail and these are made up of two interpenetrating networks and each network has junctions at which its columns meet. The space around the networks is then filled by the solvent. These phases are the "double gyroid" (DG, space group $Ia\bar{3}d$), "double diamond" (DD, $Pn\bar{3}m$) and "plumber's nightmare" (PN, $Im\bar{3}m$), and they have three-, four- and six-way junctions respectively.

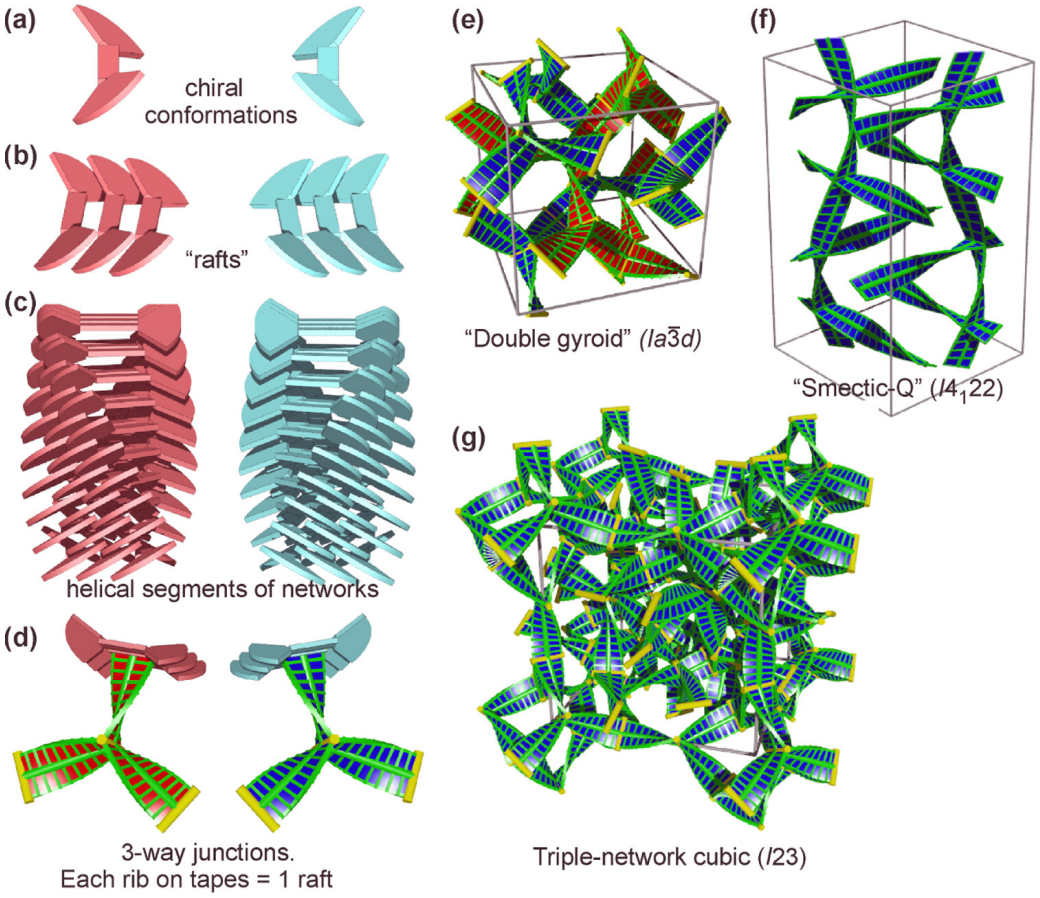

Figure 1.26: Schematic representations of the self-assembly of achiral polycatenar molecules into thermotropic bicontinuous phases. (a) Polycatenars with a rigid aromatic core and two or three end chains which are depicted as fans. Two to four of these polycatenars join to form (b) rafts which in turn stack into (c) helical networks. The networks meet each other at (d) junctions (here a three-way junction is shown). (e–g) Ribbon models of (e) the double-gyroid which is achiral, (f) the tetragonal Smectic-Q phase which is chiral, and (g) the chiral triple-network cubic phase. The space group are shown in brackets for each bicontinuous phase. [116]

For many years now, the double gyroid phase has been known to exist in some thermotropic LC made from rod-like mesogens. Like its lyotropic counterpart, it is made up of two networks, each with three-way junctions. Another common thermotropic cubic phase is one formerly known as Smectic-D (SmD), named so because it was thought to be a smectic phase [114]. Initially, Smectic-D was thought to be in the same space group as the plumber's nightmare, ($Im\bar{3}m$), but was later moved to a lower symmetry group of $I23$ as it was found to always be chiral, even if when made from achiral molecules [114]. Like PN it has three networks, but only has three-way junctions joining each network. A third bicontinuous thermotropic LC that has been observed is the so-called Smectic Q, but unlike the other two it has a tetragonal symmetry [113].

It is made up of two networks, all thought to be of the same chirality and all having four-way junctions. This phase has also been found to always be chiral, regardless of the chirality of the molecules that make it up. Some of these achiral compounds even display chirality in the isotropic liquid phase, termed Iso* [115].

These phases are made up of polycatenars, which are molecules characterised by having multiple flexible chains (referred to as tails) attached to a rigid central core made of aromatic molecules. In these bicontinuous phases the molecules have 1-3 aliphatic chains at the ends. The rod-like molecules then bunch up into rafts of about three or four rods, see figure 1.26(a). The columnar networks are then made up of these rafts stacked together (figure 1.26(b)). The rafts would ideally prefer to stack up parallel to each other to maximise the $\pi - \pi$ bonds between the aromatic cores, but instead they are twisted through angles of 7-9° because of steric clashes of the end chains (figure 1.26(c)). This then induces helicity within the columns. At the junctions the columns come in with the same handedness for better packing and hence there is only one handedness within each network. The junctions therefore stabilise the chirality and prevent helical reversals, refer to figure 1.26(b). In the DG the networks are of opposing chirality and hence it being achiral overall, while in the smectic Q has homochiral networks [113], [114], [115].

1.4.8 Antiferrochirality in a Liquid Crystal Phase of Fddd

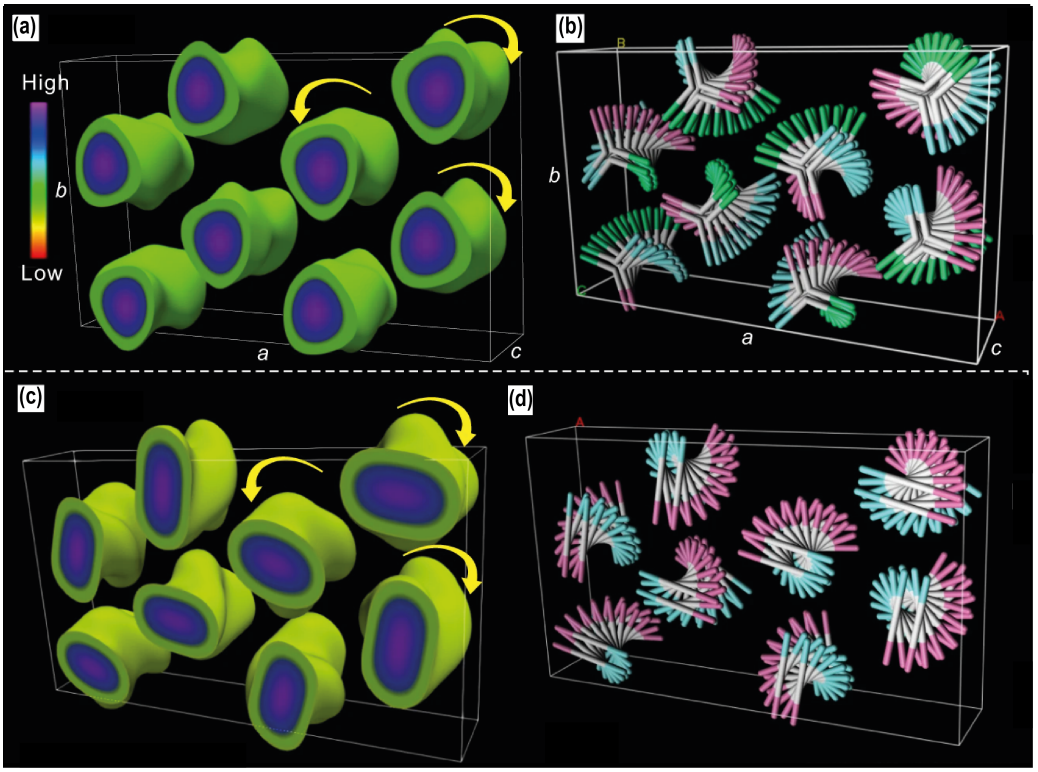

Figure 1.27: Liquid crystal phases in IC^3/n and FO16 Compounds. (a) The electron density map of (a) IC^3/n and (c) FCN16, showing the helical columns. The stylised models of (b) IC^3/n and (d) FO16, created from the the electron density maps. Taken from [117].

A recent study by Li et al. [117] reported the observation of a chiral columns in a LC phase of compounds that were made from achiral polycatenars. The chirality presents in the form of helical columns [117] similar to networks in the bicontinuous phases (figure 1.27). The unit cell is comprised of eight columns, four right-handed and four left-handed helices and this was shown by the electron density maps and supported by the patterns in the small angle x-ray diffraction. The overall LC phases are achiral because of the equal number of left and right handed columns. The x-ray diffraction also reveals that the phase has an Fddd symmetry.

The chirality in these Fddd phases arise in the same way as the bicontinuous phases [114] [115]. Unlike with the bicontinuous phases where the twisting is about 7-10°, the Fddd phases have larger twists of about 18°. This is thought to be due to the six tails in the molecules as compared to 1-3 in the bicontinuous phases. This observation was made in four compounds of two types. The first type has a bent core with the molecules being IC^3/n, where n is 12 or 14. The second type is the straight core compounds FCN16 and FO16. Upon further heating the IC^3/n compounds the columns lose their chirality and transition to a triagonal columnar

LC phase. Similarly, the columns in the FCN16 and FO16 compounds lose their chirality upon heating and transition into a hexagonal LC phase. Further heating of both types of compounds results in a continuous phase transition into an isotropic liquid. The phases of each compound are shown in figure 1.27.

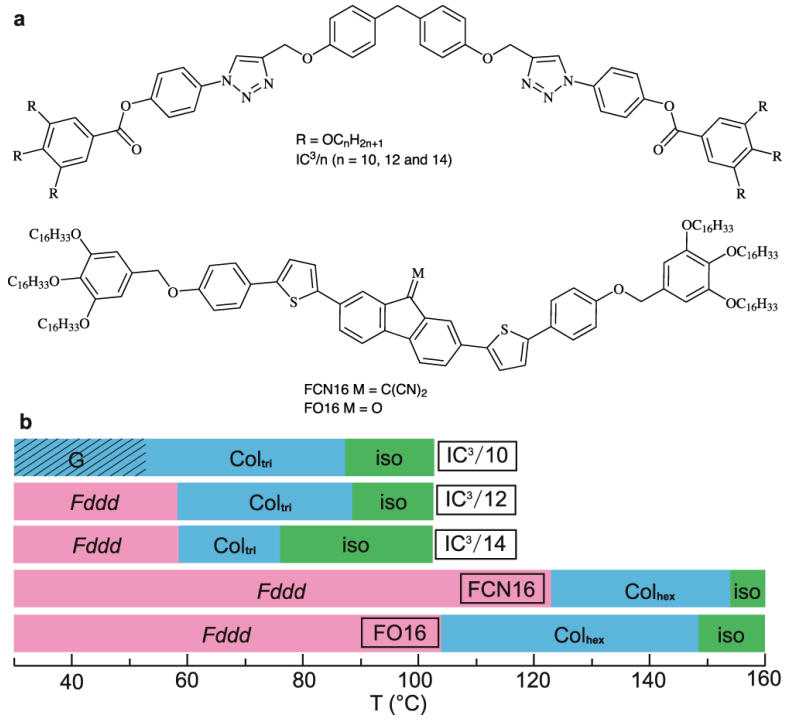

Figure 1.28: (a) The chemical formulae of IC^3/n, FCN16, and FO16. (b) The phase transitions with temperature of the compounds IC^3/n, FCN16, and FO16. Taken from [117]

Chapter 7 of this thesis will present a simple model and results of investigating the packing of the columns in these complex systems for the straight core molecules. Significant time was spent working on a model for the bent core molecule systems, however, could not reproduce the results found from the experiments.

References

[1] George Odian. *Principles of Polymerization*. Wiley, 2004.

[2] N M Nurazzi et al. *Introduction to Polymer Crystallization*. John Wiley Sons, Ltd, 2023, pp. 1–12.

[3] Peggy Cebe and Su Don Hong. "Crystallization behaviour of poly(ether-ether-ketone)". In: *Polymer* 27 (8 1986), pp. 1183–1192.

[4] E C M Vermolen et al. "Fabrication of large binary colloidal crystals with a NaCl structure". In: *Proceedings of the National Academy of Sciences of the United States of America* 106 (38 2009), pp. 16063–16067.

[5] C W Bunn. "The crystal structure of long-chain normal paraffin hydrocarbons. The "shape" of the <CH2 group". In: *Transactions of the Faraday Society* 35 (0 1939), pp. 482–491.

[6] Alberto. Pimpinelli and Jacques. Villain. *Physics of Crystal Growth*. Cambridge University Press, 1998, p. 400.

[7] J Hook and H Hall. *Solid state physics*. 2nd. Manchester: Wiley, 1991, p. 475.

[8] A West. *Solid State Chemistry and its Applications, 2nd Edition, Student Edition*. WILEY, 2014, p. 584.

[9] A Keller. "Morphology of Crystallizing Polymers". In: *Nature 1952 169:4309* 169 (4309 1952), pp. 913–914.

[10] Paul J Phillips. "Polymer crystals". In: *Reports on Progress in Physics* 53 (5 1990), p. 549.

[11] Keller A. "A note on single crystals in polymers: Evidence for a folded chain configuration". In: *Philosophical Magazine* 2 (21 1957), pp. 1171–1175.

[12] D.C Bassett. *Principles of polymer morphology*. Vol. 20. Cambridge University Press, 1981, pp. 279–280.

[13] Ralph Jaccodine. "Observations of Spiral Growth Steps in Ethylene Polymer". In: *Nature 1955 176:4476* 176 (4476 1955), pp. 305–306.

[14] PH Till. "The growth of single crystals of linear polyethylene". In: *Journal of Polymer Science* 24 (106 1957), pp. 301–306. ISSN: 1542-6238.

[15] Von E.W Fischer. "Stufen- und Spiralförmiges Kristallwachstum Bei Hochpolymeren". In: *Zeitschrift fur Naturforschung - Section A Journal of Physical Sciences* 12 (9 1957), pp. 753–754.

[16] K H Storks. "An Electron Diffraction Examination of Some Linear High Polymers". In: *Journal of the American Chemical Society* 60 (8 1938), pp. 1753–1761.

[17] Willard Gibbs. "On the equilibrium of heterogeneous substances". In: *American Journal of Science* s3-16 (96 1878), pp. 441–458.

[18] D Turnbull and J C Fisher. "Rate of Nucleation in Condensed Systems". In: *The Journal of Chemical Physics* 17 (1 1949), pp. 71–73.

[19] P H Lindenmeyer. "Surface area and secondary nucleation theory". In: *Nature 1977 269:5627* 269 (5627 1977), pp. 396–397.

[20] J C Wittmann and B Lotz. "Epitaxial crystallization of polyethylene on organic substrates: A reappraisal of the mode of action of selected nucleating agents". In: *Journal of Polymer Science: Polymer Physics Edition* 19 (12 1981), pp. 1837–1851.

[21] Shujing Zhang et al. “Secondary nucleation in polymer crystallization: A kinetic view”. In: *Polymer Crystallization* 4 (3 2021), e10173.

[22] Akihiko Toda. *Spherulitic Growth in Crystalline Polymers*. Springer, Berlin, Heidelberg, 2013, pp. 1–12.

[23] R Eppe, E W Fischer, and H A Stuart. “Morphologische strukturen in polyäthylenen, polyamiden und anderen kristallisierenden hochpolymeren”. In: *Journal of Polymer Science* 34 (127 1959), pp. 721–740.

[24] Paul J Flory and Do Yeung Yoon. “Molecular morphology in semicrystalline polymers”. In: *Nature 1978 272:5650* 272 (5650 1978), pp. 226–229.

[25] Roland Seguela. “Critical review of the molecular topology of semicrystalline polymers: The origin and assessment of intercrystalline tie molecules and chain entanglements”. In: *Journal of Polymer Science Part B: Polymer Physics* 43 (14 2005), pp. 1729–1748.

[26] C W Bunn and T C Alcock. “The texture of polythene”. In: *Transactions of the Faraday Society* 41 (0 1945), pp. 317–325.

[27] G Ryschenkow and G Faivre. “Bulk crystallization of liquid selenium Primary nucleation, growth kinetics and modes of crystallization”. In: *Journal of Crystal Growth* 87 (2-3 1988), pp. 221–235.

[28] J Bisault, G Ryschenkow, and G Faivre. “Spherulitic branching in the crystallization of liquid selenium”. In: *Journal of Crystal Growth* 110 (4 1991), pp. 889–909.

[29] J H Magill. “Spherulites: A personal perspective”. In: *Journal of Materials Science* 36 (13 2001), pp. 3143–3164.

[30] Ferdinand. Rodriguez et al. *Principles of polymer systems*. CRC Press, 2015, p. 789.

[31] M Raimo. “Estimation of polymer nucleation and growth rates by overall DSC crystallization rates”. In: *Polymer Journal 2011 43:1* 43 (1 2010), pp. 78–83.

[32] A T Lorenzo and A J Müller. “Estimation of the nucleation and crystal growth contributions to the overall crystallization energy barrier”. In: *Journal of Polymer Science, Part B: Polymer Physics* 46 (14 2008), pp. 1478–1487.

[33] P J Haines and F W Wilburn. “Differential thermal analysis and differential scanning calorimetry”. In: *Thermal Methods of Analysis* (1995), pp. 63–122.

[34] Michael E Brown and Patrick K Gallagher. “Introduction to Recent Advances, Techniques and Applications of Thermal Analysis and Calorimetry”. In: *Handbook of Thermal Analysis and Calorimetry* 5 (C 2008), pp. 1–12.

[35] K Armitstead and G Goldbeck-Wood. “Polymer crystallization theories”. In: *Advances in Polymer Science* 100 (1991), pp. 218–311.

[36] John I Lauritzen and John D Hoffman. “Theory of Formation of Polymer Crystals with Folded Chains in Dilute Solution”. In: *Journal of research of the National Bureau of Standards. Section A, Physics and chemistry* 64A (1 1960), p. 73.

[37] John D Hoffman and Jr. John I Lauritzen. "Crystallization of Bulk Polymers With Chain Folding: Theory of Growth of Lamellar Spherulites". In: *Journal of Research of the National Bureau of Standards. Section A, Physics and Chemistry* 65A (4 1961), p. 297.

[38] Wenbing Hu. "Growth rate equations of lamellar polymer crystals". In: *Polymer Crystallization* 1 (4 2018), e25838.

[39] Jr John I Lauritzen and Elio Passaglia. "Kinetics of Crystallization in Multicomponent Systems: II. Chain-Folded Polymer Crystals". In: *Journal of Research of the National Bureau of Standards. Section A, Physics and Chemistry* 71A (4 1967), p. 261.

[40] J J Point, M Ch Colet, and M Dosiere. "Experimental criterion for the crystallization regime in polymer crystals frown from dilute solution: Possible limitation due to fractionation". In: *Journal of Polymer Science Part B: Polymer Physics* 24 (2 1986), pp. 357–388.

[41] M Dosiere, M -Ch Colet, and J J Point. "An isochronous decoration method for measuring linear growth rates in polymer crystals". In: *Journal of Polymer Science Part B: Polymer Physics* 24 (2 1986), pp. 345–356.

[42] John D Hoffman. "Regime III crystallization in melt-crystallized polymers: The variable cluster model of chain folding". In: *Polymer* 24 (1 1983), pp. 3–26.

[43] Jean Jacques Point. "Reconsideration of kinetic theories of polymer crystal growth with chain folding". In: *Faraday Discussions of the Chemical Society* 68 (0 1979), pp. 167–176.

[44] D M Sadler and G H Gilmer. "A model for chain folding in polymer crystals: rough growth faces are consistent with the observed growth rates". In: *Polymer* 25 (10 1984), pp. 1446–1452.

[45] Jens Uwe Sommer. "Theoretical Aspects of the Equilibrium State of Chain Crystals". In: *Lecture Notes in Physics* 714 (2007), pp. 19–45. ISSN: 1616-6361.

[46] M Muthukumar and P Welch. "Modeling polymer crystallization from solutions". In: *Polymer* 41 (25 2000), pp. 8833–8837.

[47] Michael C Zhang, Bao Hua Guo, and Jun Xu. "A Review on Polymer Crystallization Theories". In: *Crystals* 7 (1 2016).

[48] A Toda. "Growth of polyethylene single crystals from the melt: change in lateral habit and regime I-II transition". In: *Colloid Polymer Science* 270 (7 1992), pp. 667–681.

[49] Akihiko Toda. "Growth mode and curved lateral habits of polyethylene single crystals". In: *Faraday Discussions* 95 (0 1993), pp. 129–143.

[50] J P K Doye. "Computer simulations of the mechanism of thickness selection in polymer crystals". In: *Polymer* 41 (25 2000), pp. 8857–8867.

[51] David M Sadler. "Roughness of growth faces of polymer crystals: Evidence from morphology and implications for growth mechanisms and types of folding". In: *Polymer* 24 (11 1983), pp. 1401–1409.

[52] Stephen Z D Cheng and Bernard Lotz. "Enthalpic and entropic origins of nucleation barriers during polymer crystallization: the Hoffman–Lauritzen theory and beyond". In: *Polymer* 46 (20 2005), pp. 8662–8681.

[53] Jonathan P K Doye and Daan Frenkel. "Mechanism of Thickness Determination in Polymer Crystals". In: *Physical Review Letters* 81 (1998), p. 2160.

[54] Jonathan P K Doye and Daan Frenkel. "The mechanism of thickness selection in the Sadler-Gilmer model of polymer crystallization". In: *The Journal of Chemical Physics* 110 (14 1999), pp. 7073–7086.

[55] Akihiko Toda. "Kinetic barrier of pinning in polymer crystallization: Rate equation approach". In: *The Journal of Chemical Physics* 118 (18 2003), pp. 8446–8455.

[56] G Ungar and A Keller. "Inversion of the temperature dependence of crystallization rates due to onset of chain folding". In: *Polymer* 28 (11 1987), pp. 1899–1907.

[57] E Boda et al. "Crystallization rate minima in a series of n-alkanes from C194H390 to C294H590". In: *Macromolecules* 30 (16 1997), pp. 4674–4678.

[58] Goran Ungar and Andrew Keller. "Time-resolved synchrotron X-ray study of chain-folded crystallization of long paraffins". In: 27 (12 1986), pp. 1835–1844.

[59] Terry A Land et al. "Recovery of surfaces from impurity poisoning during crystal growth". In: *Nature 1999 399:6735* 399 (6735 1999), pp. 442–445.

[60] Paul G Higgs and Goran Ungar. "The growth of polymer crystals at the transition from extended chains to folded chains". In: *The Journal of Chemical Physics* 100 (1 1994), pp. 640–648.

[61] Stephen Z D Cheng and Jianhua Chen. "Nonintegral and integral folding crystal growth in low-molecular mass poly (ethylene oxide) fractions. III. Linear crystal growth rates and crystal morphology". In: *Journal of Polymer Science Part B: Polymer Physics* 29 (3 1991), pp. 311–327.

[62] John D Hoffman. "Transition from extended-chain to once-folded behaviour in pure n-paraffins crystallized from the melt". In: *Polymer* 32 (15 1991), pp. 2828–2841.

[63] David M Sadler. "On the growth of two dimensional crystals: 2. Assessment of kinetic theories of crystallization of polymers". In: *Polymer* 28 (9 1987), pp. 1440–1454.

[64] Yu Ma et al. "Understanding self-poisoning phenomenon in crystal growth of short-chain polymers". In: *Journal of Physical Chemistry B* 113 (41 2009), pp. 13485–13490.

[65] Stephen Whitelam, Yuba Raj Dahal, and Jeremy D Schmit. "Minimal physical requirements for crystal growth self-poisoning". In: *Journal of Chemical Physics* 144 (2016), p. 64903.

[66] S J Organ, G Ungar, and A Keller. "Rate Minimum in Solution Crystallization of Long Paraffins". In: *Macromolecules* 22 (4 1989), pp. 1995–2000.

[67] Jorge Fernández et al. "Effect of molecular weight on the physical properties of poly(ethylene brassylate) homopolymers". In: *Journal of the Mechanical Behavior of Biomedical Materials* 64 (2016), pp. 209–219.

[68] Stephanie F Marxsen et al. "Crystallization Rate Minima of Poly(ethylene brassylate) at Temperatures Transitioning between Quantized Crystal Thicknesses". In: *Macromolecules* (2022).

[69] Masafumi Tasaki et al. "Polymorphism and phase transitions of precisely halogen-substituted polyethylene. (1) Crystal structures of various crystalline modifications of bromine-substituted polyethylene on every 21st backbone carbon". In: *Macromolecules* 47 (14 2014), pp. 4738–4749.

[70] Emine Boz et al. "Synthesis and crystallization of precision ADMET polyolefins containing halogens". In: *Macromolecules* 39 (13 2006), pp. 4437–4447.

[71] Emine Boz et al. "Precision ethylene/vinyl chloride polymers via condensation polymerization". In: *Macromolecules* 40 (18 2007), pp. 6545–6551.

[72] Emine Boz et al. "Precision ethylene/vinyl bromide polymers". In: *Advanced Synthesis and Catalysis* 349 (1-2 2007), pp. 137–141.

[73] Emine Boz et al. "Well-defined precision ethylene/vinyl fluoride polymers: Synthesis and crystalline properties". In: *Macromolecules* 41 (5 2008), pp. 1647–1653.

[74] R G Alamo et al. "Crystallization of polyethylenes containing chlorines: Precise vs random placement". In: *Macromolecules* 41 (19 2008), pp. 7141–7151.

[75] Xiaoshi Zhang et al. "Effect of Self-Poisoning on Crystallization Kinetics of Dimorphic Precision Polyethylenes with Bromine". In: *Macromolecules* 51 (4 2018), pp. 1386–1397.

[76] Yoshito Ikada et al. "Stereocomplex Formation between Enantiomeric Poly(lactides)". In: *Macromolecules* 20 (4 1987), pp. 904–906.

[77] Hideto Tsuji and Ippei Fukui. "Enhanced thermal stability of poly(lactide)s in the melt by enantiomeric polymer blending". In: *Polymer* 44 (10 2003), pp. 2891–2896.

[78] Jun Shao et al. "Remarkable melting behavior of PLA stereocomplex in linear PLLA/PDLA blends". In: *Industrial and Engineering Chemistry Research* 54 (7 2015), pp. 2246–2253.

[79] Beng Hoon Tan et al. "Recent Progress in Using Stereocomplexation for Enhancement of Thermal and Mechanical Property of Polylactide". In: *ACS Sustainable Chemistry and Engineering* 4 (10 2016), pp. 5370–5391.

[80] Hideto Tsuji, Suong Hyu Hyon, and Yoshito Ikada. "Stereocomplex Formation between Enantiomeric Poly(lactic acid)s. 3. Calorimetric Studies on Blend Films Cast from Dilute Solution". In: *Macromolecules* 24 (20 1991), pp. 5651–5656.

[81] Hideto Tsuji and Yoshito Ikada. "Stereocomplex Formation between Enantiomeric Poly(lactic acid)s. 9. Stereocomplexation from the Melt". In: *Macromolecules* 26 (25 1993), pp. 6918–6926.

[82] Yan Fei Huang et al. "The Role of Melt Memory and Template Effect in Complete Stereocomplex Crystallization and Phase Morphology of Polylactides". In: *Crystal Growth and Design* 18 (3 2018), pp. 1613–1621.

[83] Jingqun Liu et al. "Suppression of Phase Separation for Exclusive Stereocomplex Crystallization of a High-Molecular-Weight Racemic Poly(l-lactide)/Poly(d-lactide) Blend from the Glassy State". In: *Macromolecules* 53 (9 2020), pp. 3493–3503.

[84] Yucheng He et al. "Tammann analysis of the molecular weight selection of polymorphic crystal nucleation in symmetric racemic poly(lactic acid) blends". In: *Macromolecules* 55 (9 2022), pp. 3661–3670.

[85] Jiaming Cui et al. "Poisoning by Purity: What Stops Stereocomplex Crystallization in Polylactide Racemate?" In: *Macromolecules* 56 (3 2023), pp. 989–998.

[86] Robert A. Meyers. *Encyclopedia of Molecular Cell Biology and Molecular Medicine*. Vol. 1. 2nd Ed. New York, NY: Wiley-Interscience, 2004.

[87] Kitzerow H and Bahr C. *Chirality in liquid crystals*. New York: Springer, 2005, pp. 1–87.

[88] Davide Marenduzzo. *The Physics of DNA and Chromosomes*. Bristol: IOP Publishing, 2008.

[89] Hemalatha Gunasekaran et al. "Analysis of DNA Sequence Classification Using CNN and Hybrid Models". In: *Computational and Mathematical Methods in Medicine* 2021.1 (2021), p. 1835056.

[90] Paul G. Higgs. "RNA secondary structure: physical and computational aspects". In: *Quarterly Reviews of Biophysics* 3.33 (2000), pp. 199–253.

[91] De Santis P et al. "Stability of helical conformations of simple linear polymers". In: *Journal of Polymer Science Part A: General Papers* 4.1 (1963), pp. 1383–1404.

[92] Androsch R et al. "Mesophases in polyethylene, polypropylene, and poly(1-butene)". In: *Polymer* 21.51 (2010), pp. 4639–4662.

[93] Claudio De Rosa et al. "Crystal structures and polymorphism of polymers: Influence of defects and disorder". In: *POLYMER CRYSTALLIZATION* 1.4 (2018), e10015.

[94] Auriemma F De Rosa C. *Crystals and crystallinity in polymers*. Hoboken: Wiley", 2014, pp. 1–87.

[95] Kaewkan Wasanasuk et al. "Crystal Structure Analysis of Poly(l-lactic Acid) Form On the basis of the 2-Dimensional Wide-Angle Synchrotron X-ray and Neutron Diffraction Measurements". In: *Macromolecules* 44.16 (2011), pp. 6441–6452.

[96] P. De Santis and A. J. Kovacs. "Molecular conformation of poly(S-lactic acid)". In: *Biopolymers* 6.3 (1968), pp. 299–306.

[97] W. Hoogsteen et al. "Crystal structure, conformation and morphology of solution-spun poly(L-lactide) fibers". In: *Macromolecules* 23.2 (1990), pp. 634–642.

[98] Kaewkan Wasanasuk and Kohji Tashiro. "Crystal structure and disorder in Poly(l-lactic acid) form (form) and the phase transition mechanism to the ordered form". In: *Polymer* 52.26 (2011), pp. 6097–6109.

[99] B. Eling, S. Gogolewski, and A.J. Pennings. "Biodegradable materials of poly(l-lactic acid): 1. Melt-spun and solution-spun fibres". In: *Polymer* 23.11 (1982), pp. 1587–1593.

[100] J. Puiggali et al. "The frustrated structure of poly(l-lactide)". In: *Polymer* 41.25 (2000), pp. 8921–8930.

[101] L. Cartier et al. "Epitaxial crystallization and crystalline polymorphism of polylactides". In: *Polymer* 41.25 (2000), pp. 8909–8919.

[102] Hideto Tsuji. "Poly(lactic acid) stereocomplexes: A decade of progress". In: *Advanced Drug Delivery Reviews* 107 (2016), pp. 97–135.

[103] Dierking I. "Chiral Liquid Crystals: Structures, Phases, Effects". In: *Symmetry* 2.6 (2014), pp. 444–472.

[104] Prost J deGennes P. *The physics of liquid crystals*. Oxford: Clarendon Press, 1998.

[105] D. Andrienko. "Introduction to liquid crystals". In: *Journal of Molecular Liquids* 267.45 (2018), pp. 520–541.

[106] Mohamad Azani Abd Khadir Jalani. "Temperature-Dependent X-Ray Studies of Discotic Hexagonal Columnar Mesophases in Trinuclear Gold(I) Pyrazolate Complex". In: *Malaysian Journal of Fundamental and Applied Sciences* 17 (3 2021), pp. 285–294.

[107] C Destrade et al. "Disc-Like Mesogen Polymorphism". In: *Molecular Crystals and Liquid Crystals* 106.1-2 (1984), pp. 121–146.

[108] Michel Mitov. "Cholesteric Liquid Crystals with a Broad Light Reflection Band". In: *Advanced Materials* 24 (47 2012), pp. 6260–6276.

[109] Alison D Ford, Stephen M Morris, and Harry J Coles. "Photonics and lasing in liquid crystals". In: *Materials Today* 9 (7-8 2006), pp. 36–42.

[110] R. Amaranatha Reddy and Carsten Tschierske. "Bent-core liquid crystals: polar order, superstructural chirality and spontaneous desymmetrisation in soft matter systems". In: *J. Mater. Chem.* 16 (10 2006), pp. 907–961.

[111] Hideo Takezoe and Yoichi Takanishi. "Bent-Core Liquid Crystals: Their Mysterious and Attractive World". In: *Japanese Journal of Applied Physics* 45.2R (2006), p. 597.

[112] Weihua Li and Sung-Sik Lee. "Theory of Binary Mixtures of Diblock Copolymers: A New Route to the Bicontinuous Double-Diamond Plumber's Nightmare Phases". In: (2017).

[113] Lu H. J et al. "Solution of the Puzzle of Smectic-Q: The Phase Structure and the Origin of Spontaneous Chirality". In: *Angew. Chem. Int. Ed.* 57.11 (2018), pp. 2835–2840.

[114] Zeng X and Ungar G. "Spontaneously chiral cubic liquid crystal: three interpenetrating networks with a twist". In: *Journal of Materials Chemistry C* 16.8 (2020), pp. 5389–5398.

[115] Dressel C et al. “Helical networks of -conjugated rods - A robust design concept for bicontinuous cubic liquid crystalline phases with achiral Ia3d and chiral I23 lattice”. In: *Adv. Funct. Mater* 30.45 (2020), p. 2004353.

[116] Yan Wang et al. “Enantiomers Self-Sort into Separate Counter-Twisted Ribbons of the Fddd Liquid CrystalAntiferrochirality and Parachirality”. In: *Journal of the American Chemical Society* 145 (31 2023), pp. 17443–17460.

[117] Ya xin Li et al. “A case of antiferrochirality in a liquid crystal phase of counter-rotating staircases”. In: *Nature Communications* 13 (1 2022).

2 Methodology

2.1 Curve Fitting

Curve fitting is a process in which a curve is constructed to best fit a series of data points. Curve fitting is a fundamental tool in data analysis, allowing researchers to approximate the underlying relationship between variables, model trends, and make predictions. In Chapters 3 and 4 of this thesis, theoretical models were parameterised to the experimental data by fitting using Python language.In Python, this is often accomplished using the `curve_fit` function from the `scipy.optimize` module. In this section, the `curve_fit` function and how it works is explained.

2.1.1 The Mathematics of Curve Fitting

Curve fitting involves finding a mathematical function, f(x), that best approximates a set of data points (x_i, y_i), where x_i is an independent variable, and y_i is a dependent variable. The most common approach for curve fitting is the *least squares method*, which minimises the sum of the squares of the residuals (the differences between the observed and predicted values).

Mathematically, the goal is to minimise the following objective function:

$$S(\theta) = \sum_{i=1}^{n} (y_i - f(x_i; \theta))^2 \tag{2.1}$$

.

where:

- $S(\theta)$ is the sum of the squared residuals,
- y_i are the observed data points,
- $f(x_i; \theta)$ is the model function with a vector of parameters θ,

The optimal parameters θ are those that minimise $S(\theta)$.

The `curve_fit` function in Python uses non-linear least squares to fit a function to data. The function requires the user to specify:

1. The model function in the form of the equation to fit.

2. The data points (x, y) to which the function should be fitted.
3. Initial guesses for the parameters.

The function `curve_fit` uses the Levenberg-Marquardt algorithm [1, 2] by default, which is a combination of the gradient descent and Gauss-Newton methods, to iteratively refine the parameter estimates until convergence is achieved.

2.1.2 Levenberg-Marquardt Algorithm

The Levenberg-Marquardt algorithm is a popular optimisation algorithm that is particularly effective for non-linear least squares problems. It is a blend of two minimisation methods: the gradient descent and the Gauss-Newton method [3]. The algorithm adjusts the parameters of the model iteratively to reduce the sum of the squared residuals.

- In regions where the parameters are far from their optimal values, the algorithm behaves like gradient descent, making large steps in the parameter space.
- As the solution converges to the optimal values, the algorithm switches to the Gauss-Newton method, which takes smaller, more precise steps.

The algorithm uses a damping factor to control the step size and direction. This hybrid approach allows it to converge more quickly and robustly compared to other optimisation methods, making it suitable for a wide range of curve-fitting applications.

2.2 Molecular dynamics

Molecular dynamics (MD) is a computational simulation method used to study the physical movements of atoms and molecules. By simulating the interactions of particles under various conditions, MD provides insights into molecular behaviour, thermodynamics, and kinetics at the atomic scale. The technique originated in the mid-20th century, with the pioneering work by Alder and Wainwright [4, 5] in the late 1950s and the subsequent development of algorithms by Rahman [6] in the 1960s, who performed one of the first MD simulations of a liquid system using a Lennard-Jones potential. Today, MD simulations are used in conjunction with experimental research to study systems such as polymer, where quantum mechanical effects can be ignored. Molecular dynamics are used in the simulation of poly(ethylene bromine) growth in Chapter 5 of this thesis.

MD methods can be broadly categorised into two main types, based on the model and mathematical framework used to represent a physical system. In the classical mechanics approach to MD simulations, molecules are modelled as classical objects, similar to the ball and stick representation often used in chemistry. Here, atoms are represented as soft spheres, and bonds are depicted as elastic connectors between these spheres. The motion and interactions of these particles are governed by the laws of classical mechanics . In contrast, the quantum mechanical (also referred to as first-principles) MD simulations, developed in the 1980s by Car and Parrinello [7], incorporate the quantum nature of chemical bonds. These simulations compute the electron density for the valence electrons, which are responsible for bonding, using quantum mechanical equations. Meanwhile, the dynamics of the ions (nuclei and their core electrons) are still treated using classical mechanics. Quantum MD simulations provide a significant advancement over the classical approach by offering more accurate insights into the behaviour of electrons and chemical bonds. However, they are computationally intensive and require significantly more resources. As such, in this thesis the simulation that is done is from the classical approach and for the purposes of this discussion, MD will refer specifically to the classical MD approach.

2.2.1 Nose-Hoover Thermostat and Barostat

The **Nose-Hoover thermostat** is a deterministic method used in molecular dynamics (MD) simulations to maintain a constant temperature by mimicking the interaction of the system with a heat reservoir [8, 9]. It introduces an extended system Hamiltonian by coupling the system's degrees of freedom to an additional variable, ξ, representing the thermal reservoir. The equations of motion for the system are:

$$\frac{d\mathbf{r}_i}{dt} = \frac{\mathbf{p}_i}{m_i}, \quad \frac{d\mathbf{p}_i}{dt} = \mathbf{F}_i - \xi \mathbf{p}_i, \quad \frac{d\xi}{dt} = \frac{1}{Q}\left(\sum_i \frac{\mathbf{p}_i^2}{2m_i} - \frac{3Nk_BT}{2}\right). \tag{2.2}$$

where $\mathbf{r}_i$ and $\mathbf{p}_i$ are the position and momentum of particle i, m_i is its mass, $\mathbf{F}_i$ is the force acting on it, T is the target temperature, N is the number of particles, k_B is the Boltzmann constant, and Q is a parameter determining the coupling strength between the system and the thermostat.

The **Nose-Hoover barostat**, an extension of this approach, allows pressure control by introducing a degree of freedom η to couple the system's volume to an external pressure reservoir [10]. The volume V changes dynamically, and the system's equations of motion are modified to include a scaling factor λ related to η:

$$\frac{dV}{dt} = 3V\eta, \quad \frac{d\eta}{dt} = \frac{1}{W}\left(P - P_{\text{ext}}\right), \tag{2.3}$$

where P is the instantaneous pressure, P_{ext} is the target pressure, and W is a coupling parameter analogous to Q. The combined use of the Nose-Hoover thermostat and barostat ensures accurate sampling of the isothermal-isobaric (NPT) ensemble.

2.2.2 Langevin thermostat

The **Langevin thermostat** is a stochastic method that uses random forces to simulate the effect of a heat bath [11]. It modifies the equations of motion by introducing a frictional force and a random noise term:

$$\frac{d\mathbf{r}_i}{dt} = \frac{\mathbf{p}_i}{m_i}, \quad \frac{d\mathbf{p}_i}{dt} = \mathbf{F}_i - \gamma \mathbf{p}_i + \mathbf{R}_i, \tag{2.4}$$

where γ is the friction coefficient, and $\mathbf{R}_i$ is a Gaussian random force with zero mean and variance satisfying the fluctuation-dissipation theorem:

$$\langle \mathbf{R}_i(t) \cdot \mathbf{R}_j(t') \rangle = 2\gamma k_B T \delta_{ij} \delta(t - t'). \tag{2.5}$$

This thermostat effectively maintains the system at a target temperature while introducing a damping effect. The strength of the coupling is controlled by γ, where high values increase damping and reduce temperature fluctuations, potentially disrupting dynamics.

2.2.3 Berendsen barostat

The **Berendsen barostat** is a weak-coupling approach that scales the system's volume to maintain the desired pressure [12]. Unlike the Nose-Hoover barostat, it does not aim to sample the exact NPT ensemble but provides smooth and computationally efficient pressure control. The change in volume is governed by:

$$\frac{dV}{dt} = \frac{\beta}{\tau_p}(P_{\text{ext}} - P)V, \tag{2.6}$$

where β is the isothermal compressibility, τ_p is the barostat relaxation time, and P_{ext} and P are the external and instantaneous pressures, respectively. The parameter τ_p determines the strength of the coupling; a small value results in tight control but can distort dynamics.

2.2.4 The coupling strength

The coupling strength in these methods determines how quickly the system responds to deviations from the target temperature or pressure. In general:

- For the Nose-Hoover methods, the coupling parameters Q and W need to be chosen carefully to balance responsiveness with maintaining physical dynamics.
- For the Langevin thermostat, the friction coefficient γ governs the balance between thermalisation and preserving natural dynamics.
- In the Berendsen barostat, τ_p acts as a relaxation time, controlling how gently or aggressively the volume adjusts to pressure fluctuations.

2.2.5 Optimized Potentials for Liquid Simulations

OPLS is a force field used in molecular dynamics (MD) simulations to model the interactions between atoms and molecules. Force fields provide the mathematical framework for calculating forces and energies within molecular systems, which in turn determines their behaviour over time [13]. The OPLS force field is specifically designed to simulate liquid systems and is often used for organic molecules, polymers, and biomolecules.

OPLS was developed to strike a balance between accuracy and computational efficiency. It describes bonded interactions (such as bond stretching, angle bending, and dihedral torsions) and non-bonded interactions (such as van der Waals forces and electrostatic interactions) between atoms [13]. One feature of OPLS is the ability to accurately model conformations and energetic states, especially by providing an adjustable torsional potential. This makes it particularly useful for studying flexible molecules like polymers, where rotational barriers around bonds are key to understanding behaviour like crystallisation.

2.2.6 All-Atom Molecular Dynamics

All-atom molecular dynamics simulations model systems at the level of individual atoms. The atoms in the system interact through force fields or potential energy functions, which approximate the forces between particles. The most commonly used potentials in atomistic MD simulations include the Lennard-Jones potential, Coulombic potentials for electrostatics, and bonded potentials such as bond-stretching, angle-bending, and dihedral angle terms to account for the bonded interactions . These force fields, such as CHARMM, AMBER, GROMOS, and OPLS, are parameterised based on quantum mechanical calculations and experimental data to accurately represent various molecular interactions .

Atomistic MD provides a detailed picture of molecular interactions at the atomic level, capturing the dynamics of every atom in a molecule. This allows for the accurate modelling of structural changes, such as conformational shifts. The high level of detail in atomistic MD simulations requires significant computational resources, especially for large systems or long timescales. Simulations are often limited to nanoseconds to microseconds, which may not be sufficient for observing slower processes such as crystallisation. Due to the computational cost, it can be challenging to achieve adequate sampling of the conformational space, which is necessary for statistically meaningful results.

2.2.7 Coarse-grained Molecular Dynamics

Coarse-grained MD is an approach that reduces the complexity of molecular simulations by grouping atoms into larger units, known as beads. These beads represent a collection of atoms or a functional group, reducing the degrees of freedom and the number of interactions that need to be computed. The choice of how to group atoms into beads depends on the level of resolution desired and the specific application of the simulation. The interactions between beads are defined by effective potentials that are derived to reproduce the essential features of the system's behaviour, such as structural, thermodynamic, or dynamic properties. Often smaller scale atomistic simulations are ran to configure the potentials concerning the group of atoms or functional groups that are to be grouped, and then they are mapped onto effective potentials for the coarse-grained model. A similar approach is taken in this work in Chapter 5, where a coarse-grained model of poly(ethylene bromine) is simulated.

2.2.8 Velocity-Verlet algorithm

During the simulations the position, $r_i(t)$ and velocity $v_i(t)$, of the particles at a time t are recorded and stored. The forces acting upon them are calculated according to the chosen potential that best describes their interactions. The resulting equations of motions are then integrated over the chosen time-step Δt using an appropriate algorithm to compute the position of the particles at time t + Δt. In this work the Large-scale Atomic/Molecular Massively Parallel Simulator (LAMMPS)is used whose default algorithm is the Velocity-Verlet algorithm. The Velocity-Verlet algorithm [14] is a second-order accurate, time-reversible algorithm that conserves energy well over long run . To understand how it works we derive the algorithm by two third-order Taylor expansions for the particle i positions, one forward and one backward in time,

$$r(t + \Delta t) = r(t) + v(t)\Delta t + \frac{f(t)}{2m}\Delta t^2 + \frac{\Delta t^3}{3!}\dddot{r} + \mathcal{O}(\Delta t^4) \tag{2.7}$$

,

$$r(t-\Delta t) = r(t) + -v(t)\Delta t + \frac{f(t)}{2m}\Delta t^2 - \frac{\Delta t^3}{3!}\dddot{r} + \mathcal{O}(\Delta t^4) \tag{2.8}$$

.

Where f(t) is the acceleration of the particle at time t and $\dddot{r}(t)$ is the the rate of change of an object's acceleration over time (jerk). By adding equations 2.7 and 2.8, and rearranging we get,

$$r(t+\Delta t) = 2r(t) - r(t-\Delta t) + \frac{f(t)}{m}\Delta t^2 + \mathcal{O}(\Delta t^4) \tag{2.9}$$

.

Equation 2.9 provides a way to compute the new position ($r(t+\Delta t)$) using the current position ($r(t)$), the previous position ($r(t-\Delta t)$), and the current acceleration ($f(t)$). It also has an intrinsic error of order δt^4 that is independent of the time step. If we derived the velocity in a similar manner it would only be accurate to the order of δt^2. Instead, we want to incorporate information about the acceleration change over the time step which gives a more accurate estimate of the velocity over the interval. We first update the position using:

$$r(t+\Delta t) = r(t) + v(t)\Delta t + \frac{f(t)}{m}\Delta t^2 \tag{2.10}$$

,

After computing the new position $r(t+\Delta t)$, we calculate the new acceleration $f(t+\Delta t)$ at this updated position. To update the velocity, we use the average of the acceleration at the current and next time steps:

$$v(t+\Delta t) = v(t) + \frac{f(t+\Delta t) + f(t)}{2m}\Delta t \tag{2.11}$$

.

This velocity update uses the fact that the acceleration (force divided by mass) changes smoothly between time steps, so averaging the two accelerations gives a more accurate estimate of the velocity over the interval. By using both the current and future accelerations to update the velocity, the Velocity-Verlet algorithm efficiently balances computational cost with accuracy, making it one of the most widely used methods in molecular dynamics.

2.2.9 Boltzmann Inversion

Boltzmann inversion is a method used to derive coarse-grained (CG) potentials from detailed all-atom molecular simulations. In CG models, groups of atoms are represented by fewer particles (beads) to reduce the complexity of simulations [15]. Boltzmann inversion helps translate the atomistic behaviour of the system into these simplified models.

The process works by taking distribution functions, such as the distribution of distances or angles between atoms in the all-atom model, and converting them into effective potentials for the CG model. These distribution functions represent the probability of different configurations occurring at a given temperature. According to Boltzmann's law, the potential energy ($U(r)$) between particles can be related to the probability distribution ($P(r)$) of their distances (or angles) by the equation:

$$U(r) = -k_B T \ln P(r) \tag{2.12}$$

where $U(r)$ is the potential energy, k_B is the Boltzmann constant, T is the temperature, $P(r)$ is the probability distribution of the distance r.

In reality $U(r)$ is a free energy and is temperature dependent because $P(r)$ is calculated at a specific temperature. However, given the temperature range that is study in Chapter 5, it is not expected that this will have a great effect on the results. This method has been used successfully in several similar simulations in the past [16, 17, 18].

By applying this equation, the potential energy is inverted from the probability distribution, creating a CG potential that captures the essence of the atomistic interactions.

2.3 Monte Carlo Dynamics

Monte Carlo (MC) simulations are a class of computational algorithms that rely on repeated random sampling to obtain numerical results. The name "Monte Carlo" is derived from the famous casino in Monaco, reflecting the method's reliance on random chance, much like gambling. These simulations are widely used in various fields, including physics, chemistry, finance, engineering, and biology, to model complex systems and processes. In the context of polymer simulations, MC methods are particularly valuable for studying the statistical and thermodynamic properties of polymers, which can be computationally prohibitive to investigate using deterministic methods because of the system's high dimensionality and the complex potential energy landscapes involved.

MC methods utilise random numbers to sample the states of a system according to some prob-

ability distribution. The fundamental idea is to generate a large number of random configurations of the system and calculate an average property over these configurations. The accuracy of the result improves with the number of samples, thanks to the law of large numbers. Many MC methods, especially those used in statistical physics and polymer simulations, are based on Markov chains. A Markov chain is a stochastic process that moves through a sequence of states, where the probability of each state depends only on the state immediately preceding it (the Markov property). This property is leveraged in MC methods to generate new states from old ones using a transition probability.

There are several algorithms used in MC simulations; however, in this thesis only two algorithms are implemented. The first is the Metropolis-Hastings algorithm [19], and the second is the Glauber dynamics [20].

2.3.1 Metropolis-Hastings Algorithm

The Metropolis-Hastings algorithm is a widely used Markov Chain Monte Carlo (MCMC) method [19]. It generates a sequence of states according to a desired probability distribution (often the Boltzmann distribution in physical systems). The algorithm does this by proposing a new state based on the current state and accepting or rejecting the new state with a probability that ensures convergence to the target distribution. It works as follows:

- Start with an initial state, X_0 chosen randomly or based on prior knowledge of the system. This initial state does not need to be in equilibrium.
- Generating a new state X' from the current state X_i using a proposal distribution.
- Calculate the acceptance probability $A(X_i -> X')$ for moving from state X_i to X'.
- Generate a random number r ($r \in [0, 1)$). If $r < A(X_i -> X')$, accept the new state. Otherwise, reject the move and keep the current state $X_{i+1} = X_i$

The algorithm is adapted to the work in Chapter 6, where the transition probabilities are set.

2.3.2 Glauber Dynamics

Glauber dynamics is another MCMC method, but it is specifically designed for discrete-state systems, such as spin systems like the Ising model in statistical physics. It is also used in lattice gas models and for systems with discrete states such as lattice-based polymer models. The focus of Glauber dynamics is on flipping individual states based on the configuration of neighbouring states and thermal fluctuations. How it works:

- Start with an initial configuration of the system.
- Choose a lattice site i at random.
- Calculate the energy change ΔE that would result from the flipping of the state at site i. The energy change is calculated considering only the local environment of site i.
- Calculate the probability Pi of changing the state at i using the change in energy.
- Generate a random number r ($r \in [0, 1)$) and change the state only if $r < P_i$, otherwise, keep it the same.

2.3.3 Depth-First Search

Depth-First Search (DFS) is a fundamental algorithm in computer science and mathematics that is used to traverse or search through tree or graph data structures. It is particularly useful in applications requiring a complete examination of all vertices and edges, such as pathfinding, topological sorting, and detecting connected components within graphs [21]. The approach of DFS is characterised by its systematic traversal, starting at a specified node (often referred to as the "source" or "root" node) and exploring as far as possible along each branch before backtracking. This behaviour is akin to the depth-first approach in which the algorithm seeks to delve deep into one path until it can no longer continue, then retracts to explore other unvisited paths.

At its core, the DFS algorithm is based on the principles of recursion. It employs a *stack*-like structure, whether explicitly or implicitly, for managing the sequence of visited nodes. In the recursive version, this stack structure is inherent within the function calls on the program's call stack. In the iterative version, an explicit stack data structure is used to track the nodes awaiting exploration. When visiting a node, DFS marks it as "visited," then recursively or iteratively proceeds to each unvisited adjacent node, storing each encountered node within the stack. If a node has no unvisited adjacent nodes, DFS will *backtrack* to the last node in the stack with unvisited neighbours and continue from there.

The algorithm can be formally described as follows: given a graph

$$G = (V, E) \tag{2.13}$$

where V is the set of vertices and E the set of edges, DFS begins at an arbitrary source node $s \in V$. From s, DFS recursively explores each adjacent node $v \in V$ until no further nodes are reachable. The pseudocode for DFS can be summarised as:

$$\text{DFS}(v) : \begin{cases} \text{mark } v \text{ as visited} \\ \text{for each adjacent node } u \text{ of } v \\ \text{if } u \text{ is not visited, call DFS}(u) \end{cases} \tag{2.14}$$

The complexity of DFS depends on the graph structure. The time complexity is $O(V + E)$, where V is the number of vertices and E the number of edges. This is because DFS must examine each vertex and each edge in the worst case. The space complexity, particularly in recursive implementations, is determined by the depth of recursion and is $O(V)$ due to the storage of nodes in the call stack. In iterative versions, the stack size grows in proportion to the maximum depth of the graph.

2.4 The Linear Electric Quadrupole

The electric quadrupole is a higher-order multipole expansion used to describe the potential and electric field distribution generated by a system of charges that is more complex than a simple monopole (single charge) or dipole (two charges of opposite sign). The quadrupole consists of either four charges or an arrangement of charges with zero net charge and zero dipole moment but with a non-zero quadrupole moment.

The linear electric quadrupole consists of three point charges arranged linearly with the middle charge opposite in sign to the two outer charges. If we consider charges $+q, -2q$, and $+q$ separated by distances d, the quadrupole moment tensor for such a configuration is aligned along the axis of the charge arrangement.

For a linear quadrupole oriented along the z-axis, the quadrupole moment tensor ϕ_{ij} has a non-zero component $\phi_{zz} = 2qd^2$, assuming the system has symmetry about the z-axis. The interaction energy between two linear quadrupoles ($E_{\phi-\phi}$) falls off more rapidly with distance than a dipole's (decreasing as $1/r^3$). It is given by,

$$E_{\phi-\phi} = \frac{A\phi^2}{{r_{12}}^5} \tag{2.15}$$

where A given below, is a complicated equation that is in terms of Euler angle β and α defines as in figure 2.1 and r_{12} is the distance between the centres of interacting quadrupoles [22, 23].

$$A = \frac{3}{2}(3\cos^2(\beta_1) - 1)(3\cos^2(\beta_2) - 1) - 12\sin(\beta_1)\sin(\beta_2)\cos(\beta_1)\cos(\beta_2)\cos(\alpha_2 - \alpha_1) + \frac{3}{4}\sin^2(\beta_1)\sin^2(\beta_2)\cos 2(\alpha_2 - \alpha_1) \tag{2.16}$$

For quadrupoles restricted to a plane ($\alpha = 0$) A can be rewritten as,

$$A = 3\cos(2\beta_1 + 2\beta_2) + \frac{9}{16}\cos 2\beta_1 \cos 2\beta_2 + \frac{15}{16}\cos 2\beta_1 + \frac{15}{16}\cos 2\beta_2 + \frac{9}{16} \tag{2.17}$$

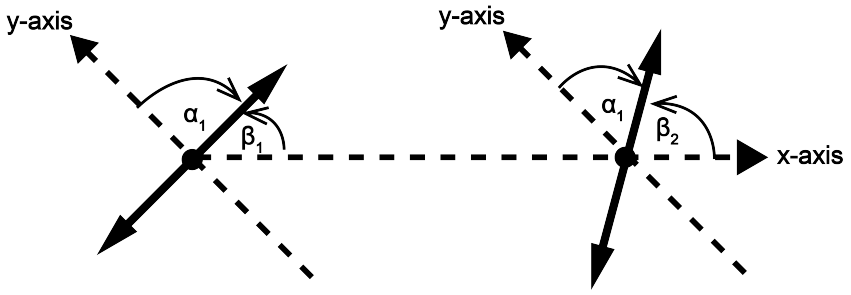

Figure 2.1: The interaction between two linear quadrupoles a distance r_{12} apart, with a quadrupole moment ϕ, and with their orientation defined by angles β_1, β_2, α_1, and α_2.

The electric quadrupole interactions will be used in Chapter 7 to quantify the interactions of a liquid crystal due to the similarity in interactions.

References

[1] Kenneth Levenberg. "A method for the solution of certain non-linear problems in least squares". In: *quarterly of applied mathematics.* (2 1944), pp. 164–168.

[2] Donald W. Marquardt. "An Algorithm for Least-Squares Estimation of Nonlinear Parameters". In: *Journal of the Society for Industrial and Applied Mathematics* 11.2 (1963), pp. 431–441.

[3] R Fletcher. *Practical methods of optimization.* Chichester ; New York: Wiley-Interscience, 1987.

[4] B. J. Alder and T. E. Wainwright. "Phase Transition for a Hard Sphere System". In: *The Journal of Chemical Physics* 27 (5 1957), pp. 1208–1209.

[5] B. J. Alder and T. E. Wainwright. "Studies in Molecular Dynamics. I. General Method". In: *The Journal of Chemical Physics* 31 (2 1959), pp. 459–466.

[6] A. Rahman. "Correlations in the Motion of Atoms in Liquid Argon". In: *Phys. Rev.* 136 (2A 1964), A405–A411.

[7] R. Car and M. Parrinello. "Unified Approach for Molecular Dynamics and Density-Functional Theory". In: *Phys. Rev. Lett.* 55 (22 1985), pp. 2471–2474.

[8] Shuichi Nosé. "A unified formulation of the constant temperature molecular dynamics methods". In: 81.1 (1984), pp. 511–519.

[9] William G. Hoover. "Canonical dynamics: Equilibrium phase-space distributions". In: *Phys. Rev. A* 31 (3 1985), pp. 1695–1697.

[10] Glenn J. Martyna, Douglas J. Tobias, and Michael L. Klein. "Constant pressure molecular dynamics algorithms". In: *The Journal of Chemical Physics* 101.5 (1994), pp. 4177–4189.

[11] T. Schneider and E. Stoll. "Molecular-dynamics study of a three-dimensional one-component model for distortive phase transitions". In: *Phys. Rev. B* 17 (3 1978), pp. 1302–1322.

[12] H. J. C. Berendsen et al. "Molecular dynamics with coupling to an external bath". In: *The Journal of Chemical Physics* 81.8 (1984), pp. 3684–3690.

[13] William L. Jorgensen, David S. Maxwell, and Julian Tirado-Rives. "Development and testing of the OPLS all-atom force field on conformational energetics and properties of organic liquids". In: *Journal of the American Chemical Society* 118 (45 1996), pp. 11225–11236.

[14] Nicos S. Martys and Raymond D. Mountain. "Velocity Verlet algorithm for dissipative-particle-dynamics-based models of suspensions". In: *Phys. Rev. E* 59 (3 1999), pp. 3733–3736.

[15] D. Reith, M. Pütz, and F. Müller-Plathe. "Deriving Effective Mesoscale Potentials from Atomistic Simulations". In: *J. Comput. Chem.* 24 (2003), pp. 1624–36.

[16] H. Meyer et al. "Static Rouse Modes and Related Quantities: Corrections to Chain Ideality in Polymer Melts". In: *Eur. Phys. J. E* 26 (2008), p. 25.

[17] William S Fall et al. "Role of Short Chain Branching in Crystalline Model Polyethylenes". In: *Macromolecules* 55 (2022), p. 8438.

[18] William S Fall et al. "Molecular Simulations of Controlled Polymer Crystallization in Polyethylene". In: *ACS Macro Letters* 12 (2023), pp. 808–813.

[19] Nicholas Metropolis et al. "Equation of State Calculations by Fast Computing Machines". In: *The Journal of Chemical Physics* 21 (6 1953), pp. 1087–1092.

[20] Roy J. Glauber. "Time-Dependent Statistics of the Ising Model". In: *Journal of Mathematical Physics* 4.2 (1963), pp. 294–307.

[21] Thomas H. Cormen et al. *Introduction to Algorithms*. 3rd. Cambridge, MA: MIT Press, 2009.

[22] A D Buckingham. "Molecular quadrupole moments". In: *Quarterly Reviews, Chemical Society* 13 (3 1959), pp. 183–214.

[23] C Hosticka, T K Bose, and Jerzy S Sochanski. "Generalized treatment of the quadrupole-quadrupole interaction of low symmetry molecules and its effect on the second dielectric virial coefficient". In: *The Journal of Chemical Physics* 61 (7 1974), pp. 2575–2579.

3 Quantitative Modelling of the Growth Rate Minima in Poly(ethylene Brassylate)

The work in this Chapter is aimed at developing a model to explain the double minima in PEB as discussed in the introduction and [1]. It is adapted from the 1D HU model that was developed for the growth rate poisoning in long chain n-alkanes. The results of this work have been published in [2].

3.1 Introduction

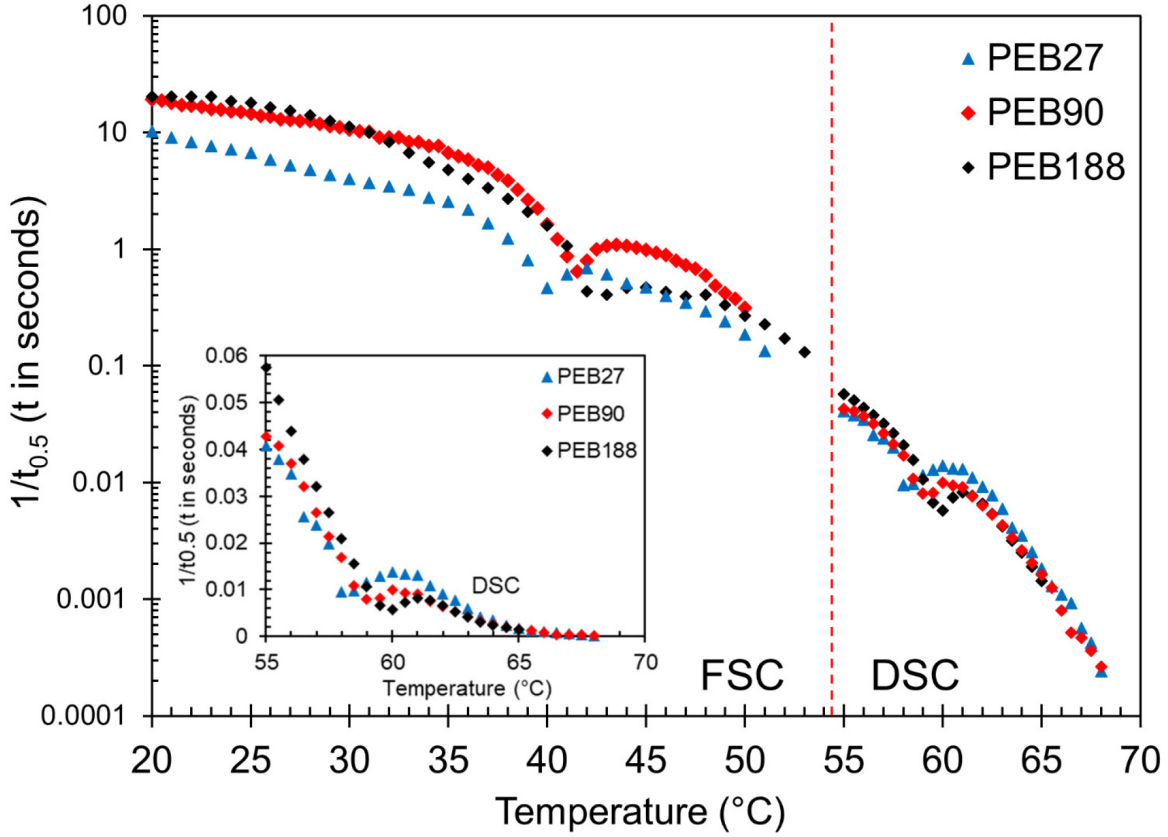

Figure 3.1: Overall isothermal crystallisation rate, represented by the inverse of the exothermic peak crystallisation time vs crystallisation temperature for PEB with different molecular weight. The vertical dashed line demarcates data obtained by conventional DSC and data obtained via fast scanning calorimetry (FSC). The high-temperature minimum of the crystallisation rate data is emphasized in the inset, where the rate is plotted in Cartesian coordinates [1].

3.1 Introduction

A study of the isothermal crystallisation kinetics of three homopolymers of poly (ethylene brassylate) PEB recently revealed an unusual behave. When PEB27, PEB90 and PEB188 where studied by DSC and FSC, their heat flow curves showed two peaks around $40°C$ and $60°C$, and melted around $70°C$ [1]. Optical microscopy of their crystals also revealed that they were small and irregular around the same temperatures that showed the peaks. The SAXS data showed that the average lamellae spacing increased by one repeating unit of the polymer chain at both minima temperatures compared to neighbouring temperatures. More specifically, from $60°C$ to $61°C$ the the average lamella spacing increased from an average of 3 repeating units to 4, where each repeating unit is around $21.19\mathring{A}$. The minima at $40°C$ was inferred from the calorimetric data to be for a change between 2 and 3 repeating units. The overall crystallisation rate of the three PEB polymers showed two minima as a function of temperature, coming near the melt-recrystallisation event temperatures.

The behaviour of these polymers is similar to that of the poisoning of the growth of the extended form by the once-folded form in the long chain alkanes [3], [4] and the poly(ethylene oxide) fractions [5]. The WAXS confirmed that the structure of the crystal was the same at all temperatures, it was suggested that this behaviour was due to the poisoning of the growth of the crystals of the longer stems by the shorter. In particular, at higher temperatures ($> 60°$C) the growth of the more stable crystal with lamellar of four repeating units is poisoned by the growth of the three repeating units crystal [1]. As the temperature decreases and approaches the melting temperature ($T_{m,3}$) of the three repeating units crystal, non-integer stems, between three and four repeating units long, are deposited at the growth of the four repeating unit crystal. Though their crystal is not stable yet, their presence inhibits further growth of the longer stems as they do not get converted or removed quicker than the next non-integer stems are deposited. This results in the growth rate minimum. Below $T_{m,3}$ the crystal of the three repeating unit long stems is more stable and takes over. The second minimum arises in a similar way although from poisoning of the three repeating unit crystal growth by the non-integer stems near the melting temperature ($T_{m,2}$) of the two repeating unit crystal.

The HU model, discussed in depth in the introduction Chapter, was developed to explain the minimum observed in the growth rate of long chain n-alkanes [6]. It was assumed that the growth of the more stable extended form was poisoned by the growth of the less stable once-folded form closer to the melting pointing of the latter. The model had the extended form growing via a two step process at the growth front. Initially, half a stem would be deposited with attachment rate A, and then another half a stem would be attached at the same rate (figure 3.2(c)i). A half-crystallised stem deposited at the growth front would be unstable above the melting temperature of the once-folded form as the detachment rate, B, would be larger than the attachment rate A. However, while unstable there can be many short-lived half stems deposited at the edge of the growth front and this number increases as the temperature approaches the melting point of the once-folded form leading to them blocking the growth of an extended chain (figure 3.2(b)). Then the growth rate of the extended form drops to zero. By introducing a conversion rate, D, for covered half stems near the growth front of the extended form it is possible to have a nonzero minimum. After the minimum, it is the growth rate of the

once-folded form that continuous to grow (Figure 3.2(c)iii).

In this Chapter, an analytical 1D model for self-poisoning due to quantised lamella thickness is developed from the 1D HU model for long chain n-alkanes. The next section of this Chapter will outlining the model, its assumptions and how it differs from the HU model. Then the rates used in the model are defined, with the PEB90 used to visualise the different options. The model is then parameterised to PEB specifically, including fitting the parameters to explicitly obtain the rates and hence the growth rate. The results of the model are then discussed before the Chapter is concluded by summarising the model, its assumptions and shortcomings.

3.2 The Model

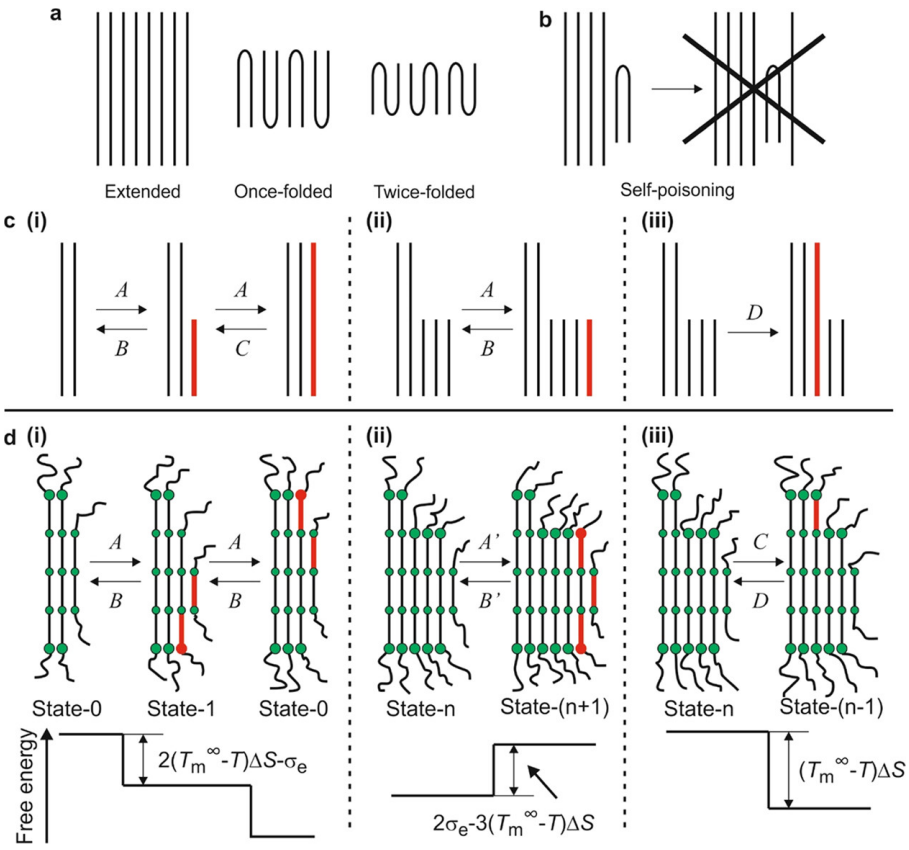

Figure 3.2: Self-poisoning in long-chain n-alkanes and in PEB. (a) In integer-folded forms, long-chain n-alkanes fold precisely in two or three sections, with chain folds tightly packed and chain ends located at the crystalline layer surfaces. (b) Growth of the extended chain form can be "poisoned" when unstable, single-folded chains frequently attach at the growth front, blocking further growth of the extended form [6]. (c) An earlier model of extended-chain growth factored in self-poisoning effects. (d) Growth stages in PEB are depicted with double ester units as circles and free energy differences shown schematically. For simplicity, only chain ends are illustrated at the amorphous lamellar surface, excluding chain folds. (i) Growth of the F_4 unit proceeds via an intermediate F_3 stem formation at the growth front. Once an F_4 stem forms in state-0, it's automatically covered by an F_2 stem, as no new crowded end surfaces are required. The rate-limiting step is the crystallisation of two end segments with a forward rate (A) and a backward rate (B). Crystallisation of one end segment results in an intermediate F_3 stem (state-1); completing the other end segment returns the system to state-0. (ii) The formation of F_3 stem sequences occurs with deposition of a further F_3 stem at rate ((A') (state-n) to state-(n + 1), where (n > 1)), with detachment at rate ((B') (state-(n + 1) to state-(n), where (n > 1)). (iii) A covered F_3 stem at the F_4 growth front may convert to an F_4 stem at a slower conversion rate (C), with an even lower back-conversion rate (D). Taken from [2]

The same line of thought is adopted in this research in order to qualitatively explain the minima in PEB crystallisation rates. Unlike in the HU model where a stem is split in half, here a stem corresponds to the monomer that makes up PEB. And similar to the HU model the crystal grows in one dimension and thus there is no consideration of lateral surface energy. A general model for the poisoning of an N repeating units thick lamellae by an $(N-1)$ repeating units thick lamellae is developed and applied to PEB to reproduce the experimentally observed data. All the while using $N = 4$ and PEB90 to provide visual aid at different stages of developing the model. Herein, crystals of a lamellar thickness equal to N repeating units, will called be F_N forms, as each lamella consists of N crystalline sublayers. The melting temperature ($T_{m,N}$) of the forms will depend on the number of sublayers. The model is applied in the area where F_N grows at a higher temperature to F_{N-1}, their melting temperatures are such that $T_{m,N} > T_{m,N-1}$ and the effects of the poisoning are mostly expressed close to $T_{m,N-1}$ from above.

In the schematics shown in figure 3.2(d) with $N = 4$, the smallest growth/melting step is the deposition/detachment of a chain of one repeating unit and this is done at rate A. The rate limiting step is the formation of the crystalline-amorphous interface, specifically the terminal or folded surfaces of newly deposited stems at the growth front. Overcrowding at this interface, due to high concentrations of stem ends, results in either a decrease in the amorphous stems' entropy or an increase in energy due to forced tight folding. Consequently, an F_N is considered to be readily covered with a F_{N-2} unit as it would not create a crowded state. This is the state-0.

The F_N stem grows by two steps from the F_{N-2} stem at the growth front, first growing into a F_{N-1} by having a stem deposited at the end, and forming a new end surface with the neighbouring F_N stem (State 1 in figure 3.2(d)i). The new F_{N-1} stem is readily covered with an F_{N-3} stem. The growth of the F_N stem is completed by the deposition of a further stem at the other end of the F_{N-1} in State 1, and the F_{N-3} stem also grows into an F_{N-2} stem. The growth kinetics of the two steps, from State 0 to State 1 and back to State 0, are considered to be exactly the same with the formation a new end surface and growth of half of a F_N stem and reduces the free energy of the system by $(N/)(T_{m,\infty} - T)\Delta S - \sigma_e$, where $T_{m,\infty}$ is the melting temperature of an infinitely thick crystal, σ_e the surface energy and ΔS the change in melting entropy per repeat unit. The rates responsible for the forward and reverse are A and B, respectively and act in the same way.

While the crystallisation temperature is well above the melting point of F_{N-1} form $T_{m,N-1}$, the above kinetics fully describe the growth dynamics between the two forms. As the temperature approaches $T_{m,N-1}$ from above, though unstable, the deposited F_{N-1} stems begin to build up at the growth front, interrupting the growth of F_N. The depositing of the F_N stems at the growth front, state-n to state-n+1, and the reverse are described by the rates A' and B', respectively 3.2d,ii. The free energy change of the system associated with the process is $(N-1)(T_{m,\infty} - T)\Delta S - 2\sigma_e$ and is positive above $T_{m,N-1}$, since $B' > A'$. For an F_N stem covered by n F_{N-1} stems, the F_{N-1} stem adjacent the F_N growth front can convert to an F_4 stem by converting an amorphous chain to a stem. The conversion occurs at a rate C and the

reverse at rate D 3.2d,iii. The conversion will be significantly slower than deposition of a stem on an uncovered F_{N-1} stem and decreases the system energy by $(N-1)(T_{m,\infty}-T)\Delta s$ with no overall surface energy change.

Let the probability that a surface is covered by n F_{N-1} stems be P_n, with P_0 the probability of having a clean surface with no F_{N-1} stems.A steady state growth model is employed with the conditions:

$$\sum_{n=0}^{\infty} P_n = 1 \tag{3.1}$$

,

$$\frac{dP_n}{dt} = 0 \tag{3.2}$$

.

The growth equations are and their solution given by,

$$\frac{dP_0}{dt} = P_1(A+B) - P_0(A+B) = 0 \quad so \quad P_1 = P_0 \tag{3.3}$$

,

$$\frac{dP_1}{dt} = P_2(B+C) - P_1(A+D) = 0 \quad so \quad P_2 = \frac{(A+D)}{(B+C)}P_0 \tag{3.4}$$

,

$$\frac{dP_n}{dt} = P_{n+1}(B+C) - P_n(A+D) = 0 \quad so \quad P_n = \frac{(A+D)^n}{(B+C)}P_0 \tag{3.5}$$

.

F_N grows through the attachment of a stem to F_{N-1} by the attachment rate A, and through the conversion of an amorphous chain of an F_{N-1}C stem. This grow is reduced by the detachment rates B of a stem back to F_{N-1}. Using this information, a the growth rate equation for F_N can be derived as

$$G_N = (A-B)P_0 + (1-2P_0)C - (1-P_0)D \tag{3.6}$$

.

Below $T_{m,N-1}$, the F_{N-1} becomes stable and its growth takes over as that of F_N is poisoned. The growth rate is just the difference between the attachment rate and detachment of a F_{N-1} stem,

$$G_{N-1} = A' - B' \tag{3.7}$$

.

The transition between the growth of the F_N and F_{N-1} forms takes place at the temperature when $P_n = P_{n+1}$, where,

$$B' - C = A' - D \tag{3.8}$$

.

3.3 Estimation of Parameters

The pairs of rates A and B, C and D, and A' and B', are related by the free energy change associated with both the process and its reverse. Let the melting temperature of the infinitely long polymer be $T_{m,\infty}$, σ_e be the energy needed to form a new a surface and ΔS the entropy of melting each stem. For both the two steps involved in growing an F_N stem from a F_{N-2} stem, i.e. from state-0 to state-1 and from state-1 to state-0, the free energy difference for each repeating unit at temperature T is $(T_{m,\infty} - T)\Delta S$. The energy cost for the surface end created is σ_e, then the free energy decreases by

$$\Delta F_{0-1} = (N/2)(T_{m,\infty} - T)\Delta S - \sigma_e \tag{3.9}$$

,

$$\Delta F_{0-1} = 2(T_{m,\infty} - T)\Delta S - \sigma_e \quad for \quad N = 4 \tag{3.10}$$

.

And then,

$$B = Aexp(-\Delta F_{0-1}/kT) \tag{3.11}$$

.

The melting point of F_N, $T_{m,N}$, is then calculated when A=B.

$$T_{m,N} = T_{m,\infty} - \frac{2\sigma_e}{N\Delta S} \tag{3.12}$$

.

The free energy from depositing F_{N-1} at the growth front is given by

$$\Delta F_{n-(n+1)} = (N-1)(T_{m,\infty} - T)\Delta S - 2\sigma_e \tag{3.13}$$

,

$$\Delta F_{n-(n+1)} = 3(T_{m,\infty} - T)\Delta S - 2\sigma_e \quad for \quad N = 4 \tag{3.14}$$

.

With,

$$B' = A' exp(-\Delta F_{n-(n-1)}/kT) \tag{3.15}$$

.

For an F_{N-1} stem cover by other n F_{N-1} stems, in state-n, converting to an F_N stem, one surface is created and one surface is destroyed, which cancel out the surface energy cost and the free energy for crystallising one stem is

$$\Delta F_c = (T_{m,\infty} - T)\Delta S \tag{3.16}$$

.

So,

$$D = C exp(-\Delta F_c/kT) \tag{3.17}$$

.

To fit the model to the experimental data, the values of $T_{m,\infty}$, ΔS, and σ_e are estimated from the melting temperatures of F_N, F_{N-1}, and F_{N-2}, which are derived from the experimental observations. For PEB, the highest temperature at which growth of F_N is observed is 69°C, taken as $T_{m,4}$, while the melting temperatures of F_{N-1} and F_{N-2} are assumed to be a few degrees lower than the observed minima at 58–60°C (near $T_{m,3}$) and 40–43°C (near $T_{m,2}$). The ultimate melting points, $T_{m,\infty}$, were adjusted to be as close as possible, ensuring that $T_{m,4}$, $T_{m,3}$, and $T_{m,2}$ were consistent with experimental data and provided the best fit to the crystallisation rate measurements. The best-fit melting temperatures for PEB90 and PEB188 are 95.4°C, while for PEB27, it is slightly lower at 95.0°C, likely due to its higher proportion of chain ends, which increases the melt entropy [7].

By substituting $N = N - 1$ and $N = N - 2$ into equation 3.12 gives

3.3 Estimation of Parameters

$$T_{m,N-1} = {T_m}^{\infty} - \frac{2\sigma_e}{(N-1)\Delta S} \tag{3.18}$$

and,

$$T_{m,N-2} = {T_m}^{\infty} - \frac{2\sigma_e}{(N-2)\Delta S} \tag{3.19}$$

,

respectively. Combining and rearranging these gives the ultimate melting temperature as,

$${T_m}^{\infty} = (N-1)T_{m,3} - (N-2)T_{m,2} \tag{3.20}$$

.

Polymer	ΔH(Jg^{-1})	ΔS($JK^{-1}mol^{-1}$) $\Delta\bar{S} = 119$	σ_e($Jmol^{-1}$) $\bar{\sigma_e} = 6327$	$T_m{}^{\infty}$ (°C)	$T_{m,4}$ (°C)	$T_{m,3}$ (°C)	$T_{m,2}$ (°C)
PEB27	82.3	121	6230	95.0	68.0	59.0	41.0
PEB90	70.8	104	5600	95.4	68.9	60.0	42.0
PEB188	90.6	132	7150	95.4	68.9	60.0	42.0

Table 3.1: Melting Enthalpy ΔH (Values Taken from [1]) and Melting Entropy ΔS of One Repeating Unit, Surface Energy σ_e, Best-Fit Melting Points of Polymers with Infinite Fold Length (${T_m}^{\infty}$) and F_4 ($T_{m,4}$), F_3 ($T_{m,3}$), and F_2 Forms ($T_{m,2}$) Used in the Fitting of Experimental Crystallisation Data. [2]

The change in entropy of each stem, ΔS, was estimated from the melting enthalpy (ΔH) and by assuming that the polymers have a 0.5 crystallinity from the following equation;

$$\Delta S = \frac{\Delta H \times M}{0.5 \times {T_m}^{\infty}} \tag{3.21}$$

,

where M is the molar mass of the repeating unit, 270.36$gmol^{-1}$. The resulting difference in the ΔS for each polymer is due to the fact that they probably all have differing crystallinities than the assumed 0.5. The crystallinity of PEB90 was measured to be the lowest of the three by WAXS, about 0.39–0.44, depending on crystallisation temperature, while that for PEB188 is 0.50–0.59. Because of this disparity in the crystallinity and ultimately in the ΔS, an averaged $\Delta\bar{S}$ was used in the fittings instead. The surface energy σ_e was then calculated from equation

3.12 using the ${T_m}^{\infty}$ and ΔS. And for similar reasons to the entropy, an average surface energy $\bar{\sigma_e}$.

To fit the experimental data to the model, explicit equations describing how A, A' and C each depend on temperature need to be derived. The simplest choice is to have all the three rates be constant, and though this scenario does produce a minimum, it does not fit the experimental curves well at lower temperatures 3.3. This can be seen in the case of F_4 growing in the presence of F_3 used in figure 3.3. A better fit is obtained from assuming that for the rates A and A' the minimum amount of energy ($\Delta F_{B,N}$) required for a chain of form F_N, decreases with an increase in the undercooling $\Delta T_{m,N} = T_{m,N} - T$, and that this barrier is proportional to the driving force $\Delta T_{m,N} \Delta S$. This then means that,

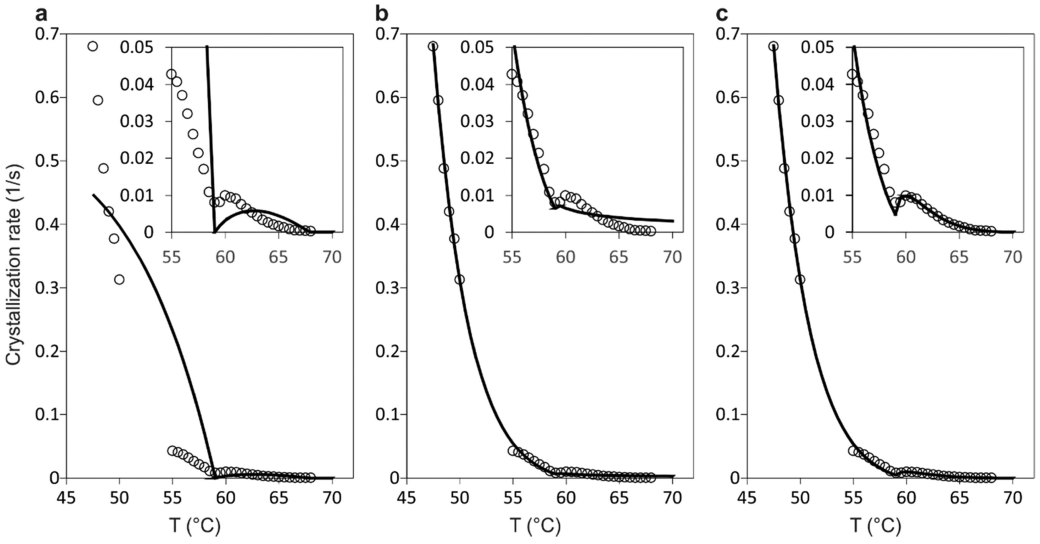

Figure 3.3: Comparison between best-fit theoretical growth rates to that of the experimental data for PEB90 between 45 and 70 $°C$ (from DSC data above 54.5 $°C$ and FSC data below 50 $°C$), subject to different choices of T-dependence of the fitting parameters [1]. The melting points of 3- and 4-layer forms used are 59 and 68 $°C$ for (a), 62 and 72 $°C$ for (b), and 60 and 69 $°C$ for (c). (a) Constant A and A', $C = 0$. (b) Both A and A' are exponentially proportional to crystallisation driving force, with C remaining constant. (c) Both A and A' are exponentially proportional to the crystallisation driving force, and C is proportional to A. Taken from [2]

$$A = A_N exp(\Delta F_{B,N}/kT) = A_N exp(u_N(T_{m,N} - T)/kT) \tag{3.22}$$

$$A' = A_{N-1} exp(\Delta F_{B,N-1}/kT) = A_{N-1} exp(u_{N-1}(T_{m,N-1} - T)/kT) \tag{3.23}$$

where A_N and A_{N-1} are the respective attachments rates at the respective melting temperatures, and u_N and u_{N-1} link the driving force to the free energy barrier for each respective form. The assumption that the free energy barrier decreases with decreasing T can be justified by the fact that at larger supercooling, the stem does not have to be fully crystallised in order to be stable, i.e., a partial attachment already counts toward crystal growth. Therefore, it is understandable that the entropy barrier for a molten stem to extend sufficiently will decrease with decreasing temperature.

More specifically, equations 3.22 and 3.23 can be rewritten for PEB with $N = 4$ as,

$$A = A_4 \exp\left(u_4(T_{m,4} - T)/kT\right) \tag{3.24}$$

$$A' = A_3 \exp\left(u_3(T_{m,3} - T)/kT\right) \tag{3.25}$$

Figure 3.3(b and e) show that indeed when $C = 0$ the crystallisation rate drops to zero, instead of a small non-zero value. In fact this is similar to what was observed in the HU model until covered once-folded stems near the growth front of the extended crystal were allowed to grow into extended stems. In that model this rate of conversion of covered chains was taken to be proportional to attachment of the second half stem into an extended stem. The same approach is adopted in this study with C being proportional A, with the restriction that the conversion rate for the covered F_{N-1} stems into F_N stems be less than A otherwise there would be no poisoning effect. Only a fraction of the covered F_{N-1} chains at the growth front of the F_N crystal would eventually convert to F_N. The conversion rate is then given by

$$C = C_N A \tag{3.26}$$

$$C = C_4 A \quad for \quad N = 4 \tag{3.27}$$

The dynamics for the growth of the F_3 crystal in the presence the F_2 form are capture and fitted by a similar set of equations.

$$A = 2A_3 \exp\left(u_3(T_{m,3} - T)/kT\right) \tag{3.28}$$

$$A' = A_2 \exp\left(u_2(T_{m,2} - T)/kT\right) \tag{3.29}$$

$$C = C_2 A \tag{3.30}$$

In the previous case, the F_3 form grew via a single attachment step, whereas in the latter case it grows via two attachment steps from an F_1 stem. To account for this, there is a factor of two multiplying the attachment rate in equation 3.27.

3.4 Results and Discussion

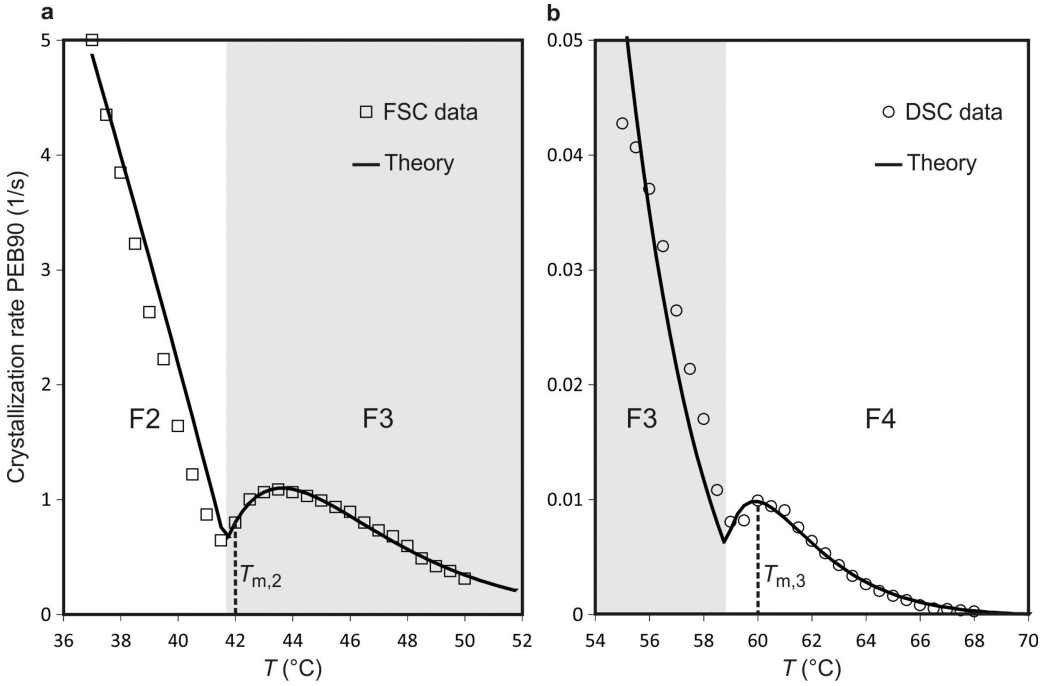

Figure 3.4: Individual fittings of experimental data. (a) Fit of the model to the growth curve between the F_3 and F_2 forms and (b) between the F_4 and F_3 forms of PEB90. The temperature regions for F_3 growth are shaded in gray. Taken from [2]

The model was calibrated to the experimental data by using the curve fitting function in Python module SciPy that fits a given set of observations, and it needs a defined mapping function. The curve fitting function provides optimum parameters for the mapping function that fit the observations, as detailed in Chapter 2. The fitting is done separately for the lower temperature region, growth between F_3 and F_2 forms, and the higher temperature region, growth between F_4 and F_3 forms. The two regions can be fitted independently because the minima are far away enough that the effects of F_4 can be ignored in the lower temperature region and similarly, in the high temperature region the F_2 growth can be ignored.

The model does a good job in capturing the general features of the experimental plots. The melting temperature are about 1 to 2°C below the minima, and this is to be expected because of the conversion rate that allow the covered F_3 stems to convert to F_4 even below $T_{m,3}$ and

similarly for F_2 converting to F_3. The fitting of the two regions does not overlap completely where F_3 is growing, even with PEB90 where the model fits the experimental data with an overall of root mean squared error of 0.91 (figure 3.4). This deficiency may be brought on by the fact that the experimental data was measured using two different methods (DSC and FSC, respectively). Another possible explanation for this inconsistency could be the fact that the contribution of the growth of F_3 from F_2 were included in the low-temperature (red) curves, but not the high-temperature (blue) ones. Then the two regions were consolidated by using weighted averages of A_3 and u_3 to construct the plots.

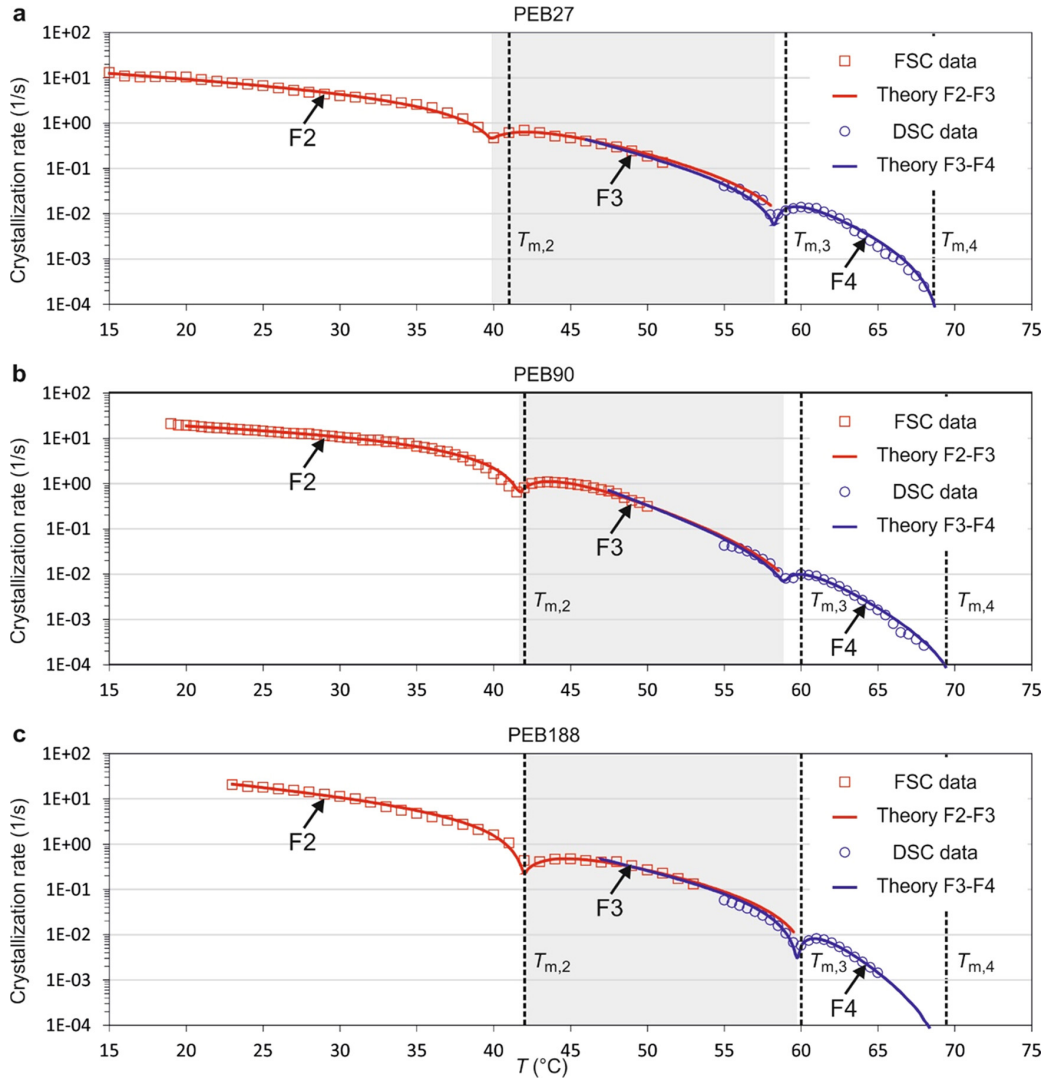

Figure 3.5: Experimental (squares and circles) and best-fit theoretical (solid curves) crystallisation rate curves on a logarithmic scale. There are two theoretical curves for each polymer, one covering the growth of F_4 and F_3 forms and the other the growth of F_3 and F_2 forms. As for the blue curves, no conversion from F_2 is considered for the growth of F_3, leading to differences in the parameters used in the red and blue curves if fitted separately. Therefore, the same weighted averages of parameters A_3 and u_3 for the growth of the F_3 form are used for the blue (F_4/F_3) and red (F_3/F_2) theoretical curves. The melting points of F_4, F_3, and F_2 forms are shown by vertical dashed lines. Panels (a), (b), and (c) show the experimental crystallisation rate and the two theoretical curves for the overall growth of PEB27, PEB90, and PEB188, respectively. The temperature regions for the growth of F_3 form are shaded in gray. Taken from [2]

From table 3.2 there is no clear trend between the parameters according to molar mass, except

for u_4 which increases with molar mass. This might be related to the fact that crystallisation rates do not show a dependence on molar mass and as such none is inherited by the fitting parameters. For instance, the medium molar mass PEB90 shows the highest crystallisation rate in F_3 and upper F_2 regions.

Polymer	u_2	u_3	u_4	$A_2(/s)$	$A_3(/s)$	$A_4(/s)$	$C_3 \times 100$	C_4
PEB27	0.912	3.90	7.95	4.17	0.217	7.34	7.26	0.100
PEB90	0.611	5.71	9.01	11.0	0.143	2.34	3.97	0.174
PEB188	1.35	3.41	11.6	7.21	0.312	1.97	4.63	0.043

Table 3.2: Best-Fit Parameters to Experimental Growth Curves of PEB27, PEB90, and PEB188. A_2, A_3, and A_4 are the attachment rates for F_2, F_3, and F_4 forms at their respective melting points, and u_2, u_3, and u_4 define the temperature dependence of the attachment rates on undercooling. C_3 and C_4 are the ratios between the conversion rates C and attachment rates A, for F_2 to F_3 and F_3 to F_4 conversion, respectively.

It should be noted that the current model is highly simplified. For example, the growth of the polymer crystal is considered as a 1D process, the attachment/detachment of a monomer repeating unit is treated as a single thermodynamic step, and the details of the formation of the crystal–amorphous surface are ignored. The effect of nucleation (primary as well as secondary) and their possible different dependencies on supercooling are not considered either. However, satisfactory quantitative fitting to the experimental data has been achieved with reasonable fitting parameters, and the current model does have the advantage that it can be solved analytically. It would be desirable to develop a model in which the presence of all three different stem lengths could be taken into account at the same time, even though it is most likely that numerical methods would be required.

3.5 Conclusion

We have developed a simple theory that enabled us to explain quantitatively the multiple crystal growth rate minima observed in polymers with regularly spaced substituent groups. Our work confirms in a quantitative way the qualitative mechanism proposed by Marxsen et al [1]. in their experimental work on PEB, also based on similar ideas in the previous studies on long alkanes [8, 9, 6]. The reason behind the abnormal temperature dependence of the growth rate is confirmed to be self-poisoning resulting from temporary attachment to the growth surface of stems that are too short to be stable. Such a model will also contribute to a better general understanding of the complex process of polymer crystallisation and identify and determine the key parameters controlling crystal growth rates. Since in more conventional polymers crystal layer thickness changes continuously with crystallisation temperature T_c, discrete rate minima are not seen. Nevertheless, self-poisoning is undoubtedly operative there too. At each T_c there is a minimum thickness l_{min} below which the crystal cannot grow, but this does not prevent

stems slightly shorter than l_{min} attaching, lingering at the growth surface and obstructing productive growth with $l > l_{min}$. Ma et al. [10] provided direct evidence of this effect using Monte Carlo simulations, showing that folded stems at the growth front can persist temporarily, delaying chain extension and causing growth rate minima due to self-poisoning. Consideration of the self-poisoning effect at a polymer growth front is needed for the development of a more realistic analytical theory of polymer crystallisation. A considerable step in the right direction was made by Sadler with his roughness-pinning theory [11] which, however, failed to reproduce most polymer crystal habits.

References

[1] Stephanie F Marxsen et al. "Crystallization Rate Minima of Poly(ethylene brassylate) at Temperatures Transitioning between Quantized Crystal Thicknesses". In: *Macromolecules* (2022).

[2] Kutlwano Gabana et al. "Quantitative Model of Multiple Crystal Growth Rate Minima in Polymers with Regularly Spaced Substituent Groups". In: *Macromolecules* (2024).

[3] Goran Ungar and Andrew Keller. "Time-resolved synchrotron X-ray study of chain-folded crystallization of long paraffins". In: 27 (12 1986), pp. 1835–1844.

[4] G Ungar and A Keller. "Inversion of the temperature dependence of crystallization rates due to onset of chain folding". In: *Polymer* 28 (11 1987), pp. 1899–1907.

[5] Stephen Z D Cheng and Jianhua Chen. "Nonintegral and integral folding crystal growth in low-molecular mass poly (ethylene oxide) fractions. III. Linear crystal growth rates and crystal morphology". In: *Journal of Polymer Science Part B: Polymer Physics* 29 (3 1991), pp. 311–327.

[6] Paul G Higgs and Goran Ungar. "The growth of polymer crystals at the transition from extended chains to folded chains". In: *The Journal of Chemical Physics* 100 (1 1994), pp. 640–648.

[7] P. J. Flory and A. Vrij. "Melting Points of Linear-Chain Homologs. The Normal Paraffin Hydrocarbons". In: *Journal of the American Chemical Society* 85.22 (1963), pp. 3548–3553.

[8] G Ungar, XB Zeng, and SJ Spells. "Non-integer and mixed integer forms in long n-alkanes observed by real-time LAM spectroscopy and SAXS". In: *Polymer* 41.25 (2000), pp. 8775–8780.

[9] G Ungar et al. "The effect of self-poisoning on crystal morphology and growth rates". In: *Interphases and Mesophases in Polymer Crystallization I* (2005), pp. 45–87.

[10] Yu Ma et al. "Understanding self-poisoning phenomenon in crystal growth of short-chain polymers". In: *Journal of Physical Chemistry B* 113 (41 2009), pp. 13485–13490.

[11] David M Sadler. “On the growth of two dimensional crystals: 2. Assessment of kinetic theories of crystallization of polymers”. In: *Polymer* 28 (9 1987), pp. 1440–1454.

4 Competition between Different Fold-lengths or Crystal Forms: A Quantitative Study of Self-Poisoning Mechanisms in Precisely Bromine-Substituted Polyethylene

In this Chapter results from applying the model from Chapter 3 [1] to PEBr is compared with a model of self-poisoning due to different forms. A paper detailing the results of the study is under preparation.

4.1 Introduction

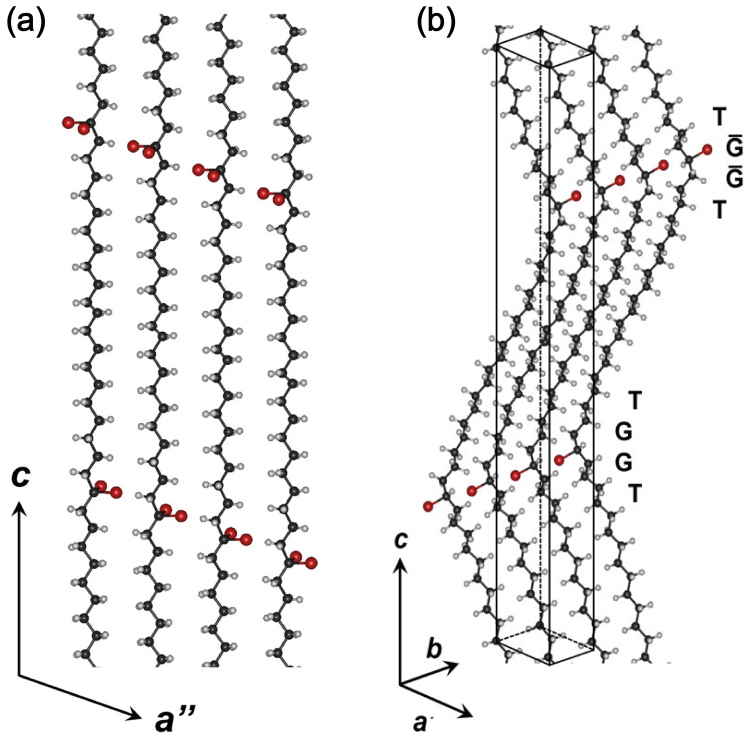

Figure 4.1: Crystal structure model of PE21Br form I and II crystal obtained by energy minimisation. (a) The polymer chains in form I are planar zig-zagging at every carbon, similar to the conventional polyethylene structure. The bromines are embedded within the bulk of the crystal. (b) Form II chains are also planar, however the bend at the carbons with the bromine and in between the chain is linear. The bromines stick out at the bends and are aligned. Courtesy of [2]

Poly(ethylene bromine) (PEBr) is a precision polymers formed by replacing one hydrogen with one bromine every m methylene groups. PEBr is known to crystallise forming two distinct crystals structures, Form I and Form II. Form I is seen to be favoured by faster cooling rates than Form II and has all-trans planar conformation (figure 4.1(a)) [2]. Form II on the other hand an all-trans configuration occurs along the m long methyl groups and then bends at the carbon with a bromine (figure 4.1(b)) [2]. Form I ($T_{m,I}$)has lower melting point that Form II ($T_{m,II}$). Form I was found to have more nuclei per unit volume during the crystallisation process than Form II [3].

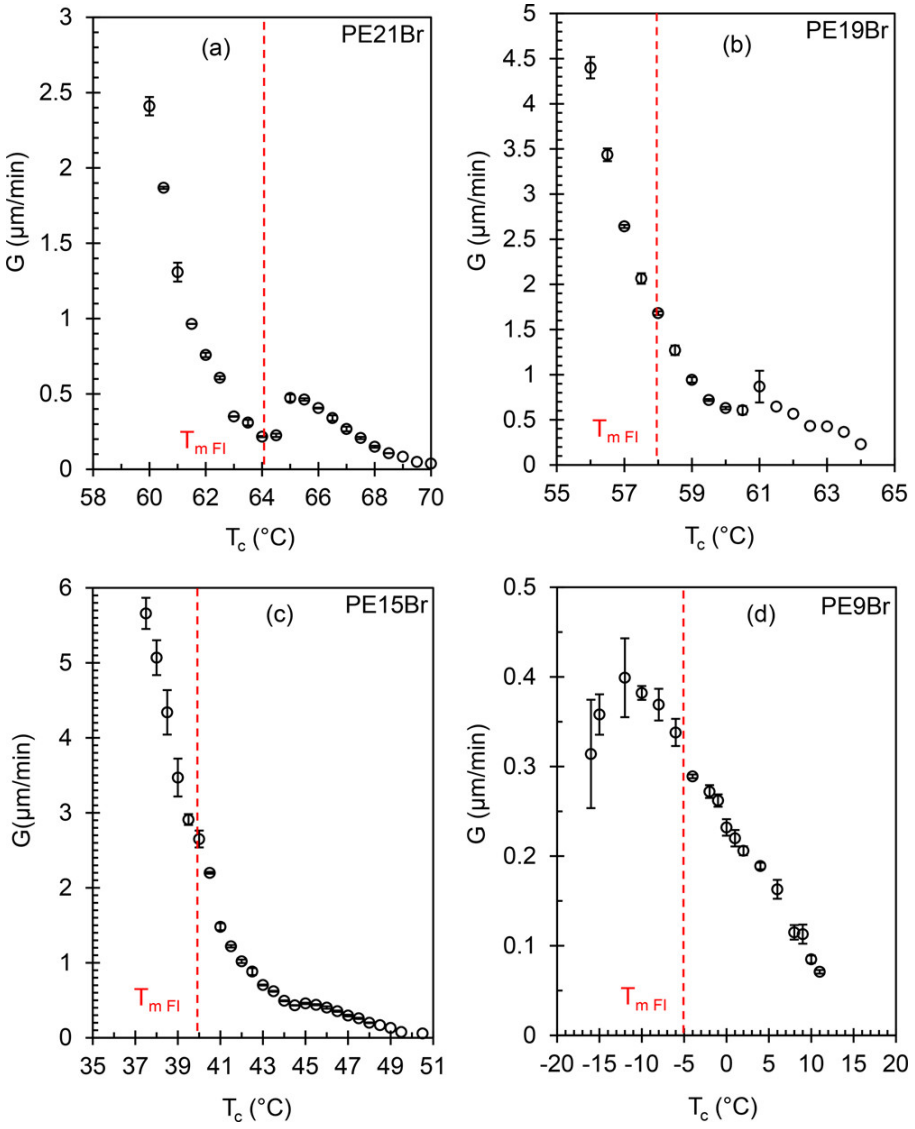

Figure 4.2: Linear growth rates of Form II as a function of crystallisation temperature. The red dashed lines indicate the melting temperature of Form I. Experimental error bars are added. (a) PEBr21 shows the most pronounced minimum, followed by (b) PEBr19, then (c) PEBr15, while (d) PEBr9 does not show any poisoning. Taken from [3]

4.1 Introduction

Optical microscopy data of three out of four PEBr polymers studied by Zhang et al [3] has shown a minimum in the linear spherulitic growth decreasing temperature of Form II. This observation was made in PEBr15, -19, and -21, while PEBr9 which was also studied did not show this minimum (figure 4.2). The growth was seen to increase with undercooling initially, then near $T_{m,I}$ it decreased to a none zero value. This led the authors of the research to conclude that the minimum was a result of the growth of Form I poisoning Form II. They argued that above the melting point of Form I, frequent but unstable attachment of Form I chains on the growth front of the Form II crystal leads to momentary blocking of the growth of the crystal until the chains detach. Here Form I and Form II are analogous to the once folded and extended chains of the long chain n-alkanes, respectively.

WAXS results showed the crystal structure both below and above $T_{m,I}$ were of Form II. This result brings into question the explanation of poisoning in PEBr as a result of the growth of Form I impeding Form II. This explanation looks even more unlikely given that solid-to-solid recrystallisation of Form I to Form II was not found and therefore the idea that Form I might grow below the poisoning temperature and then subsequently change to Form II from the time the sample is moved to it being analysed is ruled out. It was found experimentally that Form I only converts to Form II by completing melting and recrystallising.

According to Whitelam et al [4], the minimum requirement for self-poisoning for the molecule to attach in more than one way to a crystal, that those ways not be energetically equivalent and they have different attachment rates. In the previous cases of self-poisoning that are known, the more stable form grows at higher temperatures and the poisoning occurs near the melting temperature of the other form, before the crystal of the less stable form takes over the growth at the lower temperatures. This is the case with the long chain n-alkanes with growth between the extended and the once-folded forms [5], [6]. Similarly in PEB the poisoning results from growth between the four and repeating unit forms at the higher temperatures, and the three and two repeating unit forms at the lower temperatures [7]. These facts coupled with the experimental observation of Form II growing both above and below the poisoning [3] brings into doubt any explanation formed on the basis the poisoning in the PEBr compounds is due to Form II growth being poisoned by Form I attachment. This research suggests the poisoning is due to the growth of Form II with two different lamellar thicknesses instead. At higher temperatures Form II crystal grows with a longer lamellar thickness, and its growth is poisoned by the attachment of the chains of shorter lamella form, before it takes over at lower temperatures where it becomes stable.

The aim of this Chapter is to examine two quantitative models that are developed from the aforementioned schools of thought concerning the mechanism behind this poisoning. The first section looks at applying the model of poisoning due to quantised thicknesses developed in Chapter 3 to PEBr. Then the Chapter then proceeds to develop a 1D model based on poisoning of Form II growth by Form I. Then the Chapter concludes by discussing the merits and shortcomings of both models in explain the growth of PEBr.

4.2 Quantised Crystalline Layer Thickness

In this section of the Chapter it is argued that the same model that was developed to explain the self-poisoning in PEB can be readily adopted to also explain the poisoning observed for PEBr. Each stem is considered a repeating unit with m methyl groups between the bromine-substituted carbons. The polymer crystallises with a layer thickness corresponding to Nm, where N is an integer and m can be 21, 19, or 15. This crystalline form is referred to as the F_N form. The growth of this form is poisoned by F_{N-1}. The F_N form grows in the higher temperature region and F_{N-1} grows at the lower temperature, with the melting points of the two satisfying the inequality $T_{m,N} > T_{m,N-1}$. F_{N-1} stems can deposit at the growth front of the F_N crystal, however the F_N stems cannot be deposited at the F_{N-1} growth front because of the difference in length. Away from $T_{m,N-1}$, the lifetime of these chains is short as they are unstable, however as the temperature approaches $T_{m,N-1}$ from above the lifetime becomes longer. As with the poisoning in PEB and the long chain n-alkanes, the unstable F_{N-1} chains can deposit on other F_{N-1} stems that are unconverted, further preventing the growth of the longer chains and producing a more pronounced minimum as seen here.

The experimental data showed a lamella thickness of 200 Å in these polymers, corresponding to between 5 and 9 repeating units [3]. Based on this an assumption was made that the polymers had 0.5 crystallinity and that $N = 5$, without any loss in generality. However, it is possible to get fits that are as good with other N, such as 6, and different optimal parameters. A model that has Form II crystal growing both above and below the poisoning minimum is consistent with the experimental results seen. It should be noted that this model is based on there being a change in lamella thickness which was not observed in the region around the poisoning. One possible explanation for this may be a decrease in crystallinity for F_4, where an increased amorphous layer thickness has made up for the thinner F_4 crystal. Another concern of this model is the treatment of the melting point of Form I near the poisoning as a coincidence. Even with these drawbacks the model of two competing lamellae thicknesses does a good job of fitting the experimental data.

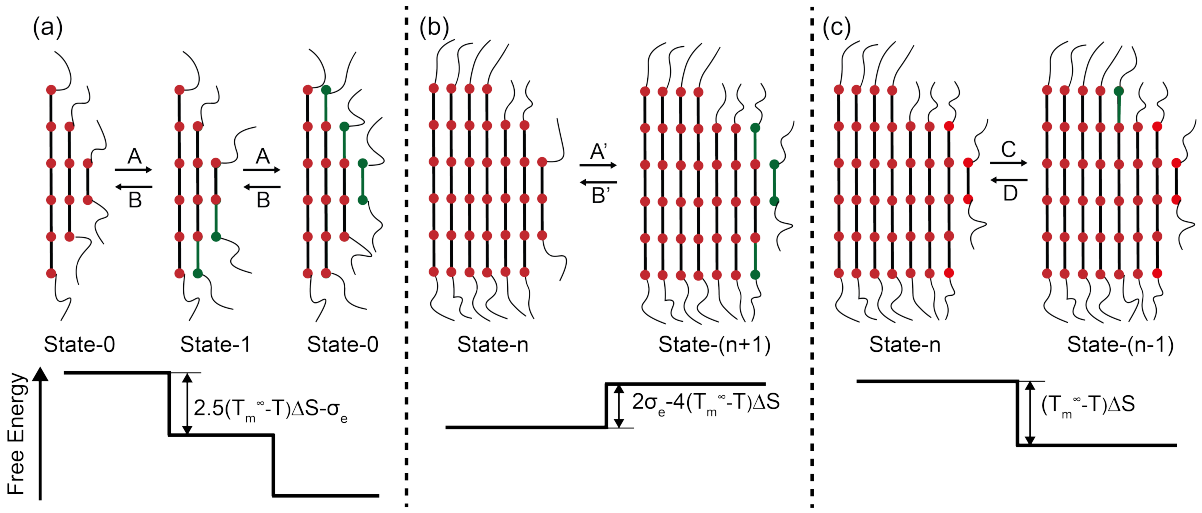

Figure 4.3: Schematic drawings of the growth steps in precision polymer PEBr. The Br atoms are shown as red circles. The free energy differences between different states are shown under their schematics. (a) The growth of F_5 through the intermediate formation of an F_4 stem at the growth front. The rate limiting steps of the growth an F_5 stem are the crystallisation of the two end segments, with forward rate A and backward rate B. (b) Formation of a sequence of F4 stems at the growth front, with deposition rate of a further F_4 stem as B′, and the reverse detachment rate as A′. (c) A covered F_4 stem at the growth font of F_5 can convert to a F_5 stem, with conversion rate C, which is a fraction of A, and the back-conversion rate is D.

The mechanism through which F_5 form grows at high temperature, how its growth is then poisoned by the F_4 form, which eventually dominates the growth at lower temperatures is captured by figure 4.3. The rate limiting step in this process is one where a chain is deposited at the ends of a chain resulting in the formation of a crystalline-amorphous interface and a higher free-energy. A consequence of this is that an F_5 form is readily covered by a F_3 stem that would not lead to overcrowding at the ends, and thus F_5 is readily covered by an F_3 stem, which in turn is covered by F_1. At high temperatures, a F_5 stem grows in two steps, firstly by growth of F_3 to F_4 , from State 0 to State 1, then by extension of the F_4 into F_5 back to State 0. In the first step, the newly formed F_4 chain forms a new surface with the existing F_5 stem paying a surface energy σ_e, and in the second step another surface is formed at the other end of F_5 stem, still paying the surface energy σ_e. The F_1 that covered the F_3 stem grew into an F_2 stem in the first step then finally into an F_3 stem covered by an F_1 in the second step. Because of this, the two steps are equivalent and happen at a forward A, with reverse B.

As the temperature approaches $T_{m,4}$, the melting point for the F_4 form, more of its chains are attached at the growth front cover the already existent F_4 chains, and this accumulation slows down the growth of the F_5. This further deposition is done at rate A', with reverse B', and creates one surface, creating State n from State (n+1). Above $T_{m,4}$, the growth of the F_5 does not slow down to a halt, instead some of the covered F_4 chains at the growth front of

the F_5 can extend to F_5 through rate C, reverse D, with no overall change in surfaces made or destroyed. This conversion rate is much slower than the growth through the attachment of the stem because of the restriction to the movement of the covered chain. The conversion rate prevents the growth plummeting to zero at the poisoning minimum. Below its melting point, the F_4 crystal becomes stable and it takes over the growth, with the rate of growth being proportional to the difference between the attachment and detachment.

The fitting parameters are shown in table 4.1 for all three polymers where the melting points for N = 4, 5 are related to $T_{m,\infty}$ by $T_{m,N} = T_{m,\infty} - \frac{2\sigma}{n\Delta S}$. The melting points of F_5 and F_4 decrease with decreasing methylene group numbers m between Br atoms along the chain, as expected by the disruptive effect of a large bromine atom to the regular PE lattice, as well as end surface free energy. The conversion rate C increases with decreasing m, i.e. decreasing length of the repeating unit, also as expected. Most fitting parameters changes monotonically with m, with the exception for the attachment rates A and A', which is always highest in PEBr19 instead of PEBr15. This slow-down of the attachment rates in PEBr15 is probably linked to the fact that in PEBr15 the melting temperatures of F_5 and F_4 are 15 degrees lower than that in PEBr19, bringing them closer to the glass transition temperature of the polymer hence its increased viscosity in the melt.

Bromine atoms are large, and their presence along the polyethylene backbone can affect how closely the chains pack in the crystalline region. When the bromine atoms are closer together, the steric hindrance between adjacent bromines might interfere more with tight packing, resulting in less efficient crystal formation and potentially a lower surface energy. This might explain why the surface energy is different for the three polymers, with the surface energy increasing with the increase in the distance between the bromine. Similarly, the greater distance between the bromines means greater flexibility of the chains. Then upon crystallisation there would be a great change in entropy. This could also explain why PEBr21 has the highest entropy change and PEBr15 has the lowest. Overall the quality of fit to the experimental data is satisfactory and the best-fit parameters physically sensible and follows the expected trend.

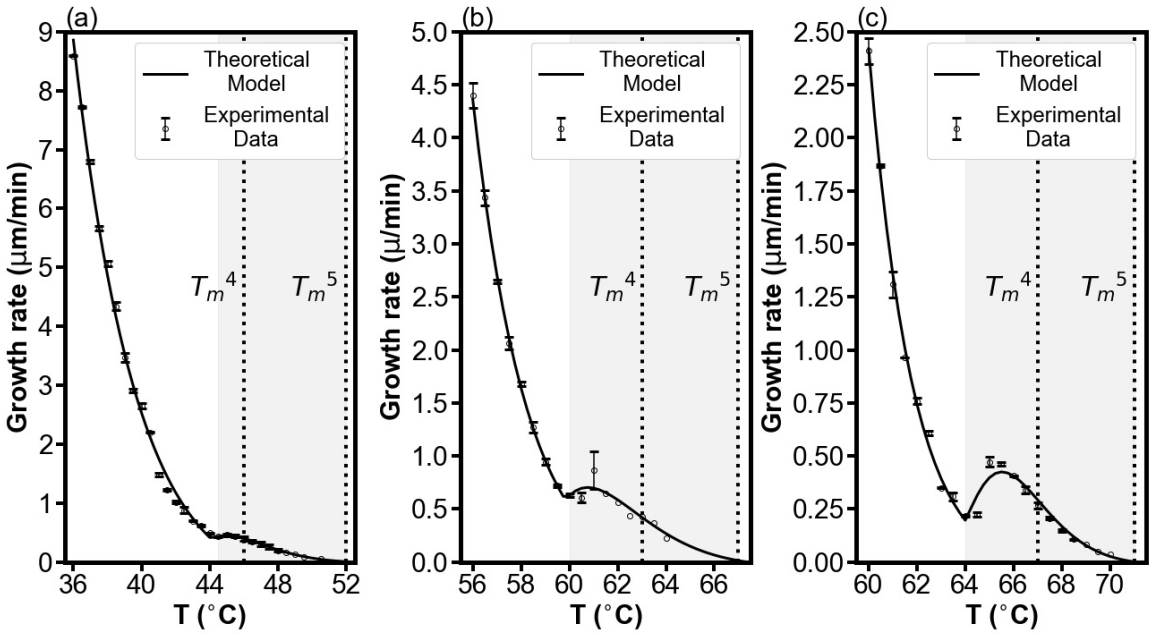

Figure 4.4: Comparison of experimental and theoretical growth rate data, according to model 1, of PEBr21 (a), -19 (b) and -15 (c). The experimental data is shown as circles and the theoretical model as solid lines. The two vertical dashed lines show $T_{m,4}$ and $T_{m,5}$ respectively.

PEBr	$T_{m,4}$ ($^\circ C$)	$T_{m,5}$ ($^\circ C$)	$T_{m,\infty}$ ($^\circ C$)	ΔS ($JK^{-1}\text{mol}^{-1}$)	σ_e (J)	u_4	u_5	A_4 (μm/min)	A_5 (μm/min)	C_0
15	46.0	52.0	76.0	74.5	4470	7.85	15.4	1.32	0.596	0.035
19	63.0	67.0	83.0	131	5220	8.17	9.16	0.383	0.829	0.048
21	67.0	71.0	87.0	144	5780	9.52	1.32	0.099	0.339	0.009

Table 4.1: Fitting parameters to experimental growth curves of PEBr15, PEBr19, and PEBr21. The melting temperatures of the F_4 and F_5 forms ($T_{m,4}$ and $T_{m,5}$, respectively), the ultimate melting temperature of the polymers with infinite fold length ($T_{m,\infty}$), melting entropy per repeating unit (ΔS), and surface energy σ_e. A_4 and A_5 are the attachment rates for F_4 and F_5 forms at their respective melting points, and u_4 and u_5 define the temperature dependence of the attachment rates on undercooling, and C_0 is the ratio of covered F_4 stems at the F_5 growth front that convert to F_5.

4.3 Poisoning of Form II growth by Form I

The fact that the PEBr polymers crystallise in two different conformations, with one of them being more stable, coupled with the fact the melting point of the Form I is very close to the

growth minimum of Form II make for a compelling case for assuming that the poisoning arises from Form I hindering the growth of Form II. In this section an alternative one-dimensional model is explored that works off this assumption. It is initially assumed that it is always Form I that attaches to the growth front at a rate A and detaches at rate B, From state-0 to state-1. Form II then only grows by conversion from Form I at the rate C and can convert back to Form-I at rate D, from state-1 back to state-0. As more Form I chains attach to the growth front closer to the melting point of Form I, this momentary build up slows down the growth of Form II. Some of these Form I chains at the interface with Form II can convert to Form II by C^* which is smaller than C, and can convert to back at the rate D^*. For this model to hold credibility it is further assumed that all Form I crystal will eventually convert to Form II.

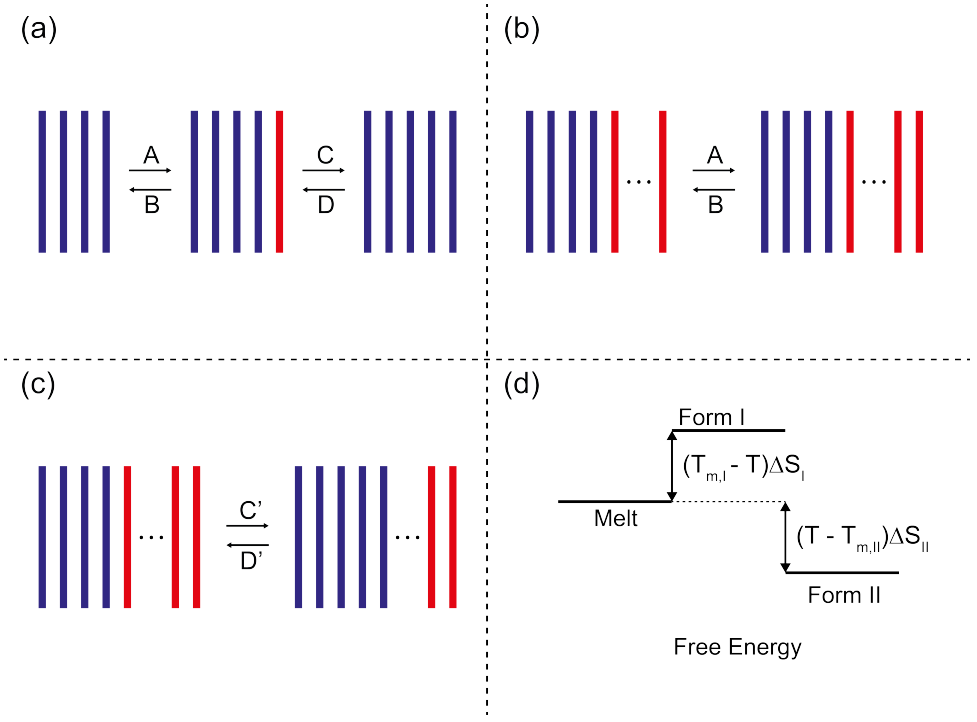

Figure 4.5: Schematic steps of growth of Form II (blue) poisoned by Form I (red). (a) The growth of a Form II chain happens by deposition first of a Form I chain (forward rate A, reverse rate B), followed by its conversion (forward conversion rate C, backward rate D). (b) Further deposition of Form I chains to the growth front, and conversion of the first Form I chain to Form II happens at a slower rate (forward rate C^*, reverse rate D^*). (d) The free energy landscape of the melt, Form I and Form II above the melting temperature of Form I.

PEBr21 is used as an example during the development of the model, to demonstrate how the model and its parameters should be adjusted to fit the experimental data. To develop a quantitative model the relations of the parameters A and B governing the growth of Form I, and C and D (C^* and D^*) governing growth of Form II need to be explicitly derived from the change in free energy. Then these can be used to further find the growth rates of the two forms

to later calibrate the model to the experimental results. The deposition of a Form I chain at the crystal surface depends on the difference in free energy between the Form I crystal and the melt (ΔF_I), and is

$$\Delta F_I = (T_{m,I} - T)\Delta S_I \tag{4.1}$$

,

where $T_{m,I}$ is the melting temperature of Form I and ΔS_I is the melting entropy of a Form I chain. Then,

$$B = A \exp\left(-\Delta F_I / RT\right) \tag{4.2}$$

.

The conversion of a Form I chain to a Form II chain depends on the difference in free energy between the two crystals of the two forms. This holds for both uncovered and covered Form I chains at the interface of the two crystals.During the conversion the free energy (ΔF_c) decreases by

$$\Delta F_c = (T_{m,II} - T)\Delta S_{II} - (T - T_{m,I})\Delta S_I \tag{4.3}$$

.

Where $T_{m,I}$ is the melting temperature of Form II and ΔS_I is the melting entropy of a Form II chain. Thus,

$$D = C \exp\left(-F_c / RT\right) \tag{4.4}$$

,

$$D^* = C^* \exp\left(-F_c / RT\right) \tag{4.5}$$

.

The melting entropy of Form II, ΔS, of each segment can be estimated from the measured mass melt enthalpy ΔH (assuming a 0.5 crystallinity), and that of Form I estimated by a further reduction due to lack of registry of the Bromine positions along the chain R,

$$\Delta S_{II} = \frac{\Delta H \times M}{0.5 T_{m,II}} \tag{4.6}$$

,

$$\Delta S_I = \Delta S_I - R \log m \tag{4.7}$$

.

Where M is the molar mass of the polymer, ΔH is the melting enthalpy of the polymer, and m is the number of carbons between the bromine atoms.

PEBr	$T_{m,I}(^\circ C)$	$T_{m,II}(^\circ C)$	$\Delta S_I(JK^{-1}mol^{-1})$	$\Delta S_{II}(JK^{-1}mol^{-1})$
15	47.0	52.0	57.8	80.3
19	65.0	69.0	112	137
21	67.0	71.0	126	151

Table 4.2: The melting temperatures of form I and form II ($T_{m,I}$ and $T_{m,II}$, respectively), the melting entropy of form I (ΔS_I), and the melting entropy of form II ($\Delta S_I I$)

The probability of having a Form II surface that is not covered by a Form I chain, in State 0, is P_0, and that of having a Form II covered by n Form I chains, in State n, is P_n, where n is a natural number. Using this information we can set up steady state equations of how the probabilities evolve, with the conditions that $\sum_{n=0}^{\infty} P_n = 1$ and $\frac{dP_n}{dt} = 0$. Then we obtain,

$$\frac{dP_0}{dt} = P_1(B + C) - P_0(A + D) = 0 \quad so \quad P_1(B + C) = P_0(A + D) \tag{4.8}$$

,

$$\frac{dP_1}{dt} = P_2(B + C^*) - P_1(A + D^*) = 0 \quad so \quad P_2 = \frac{(A + D^*)}{(B + C^*)} P_1 \tag{4.9}$$

,

$$\frac{dP_n}{dt} = P_{n+1}(B + C^*) - P_n(A + D^*) = 0 \quad so \quad P_n = \frac{(A + D^*)^n}{(B + C^*)} P_1 \tag{4.10}$$

.

By combing the equations 4.8 to 4.10 and the fact that probability adds to unity we have,

$$P_0 + \sum_{n=1}^{\infty} \frac{(A + D^*)^n}{(B + C^*)} P_1 = 1 \tag{4.11}$$

,

$$P_1 = \frac{(A + D)(B + C^* - A - D^*)}{(B + C^*)(A + D) + (B + C^* - A - D^*)(B + C)} \tag{4.12}$$

,

$$P_0 = \frac{(B+C)(B+C^*-A-D^*)}{(B+C^*)(A+D)+(B+C^*-A-D^*)(B+C)} \tag{4.13}$$

.

Form II grows through conversion of Form I chains at the interface of the two crystals by rate C for the uncovered and C^* for the covered ones. Form II chains at the interface can also be converted back to Form I by D and D^*, leading to a reduction in the Form II crystal. Therefore, the growth rate of Form II is found to be,

$$G_{II} = P_1C + (1-P_0-P_1)C^* - (1-P_0)D^* - P_0D \tag{4.14}$$

.

Form I crystal grows by according to the difference in the deposition of chain at the growth front and how fast they detach, leading to a growth rate of,

$$G_I = A - B \tag{4.15}$$

.

At higher temperatures Form I chains that are deposited at the growth front are either converted to Form II or quickly detach as they are unstable, and the probability of having an uncovered Form II surface, P_0, is high. However, as the temperature decreases their lifetime at the surface, as chains are deposited on top of existing Form I chains before they can convert or detach. This increases especially closer to the Form I melting temperature and P_0 decreases and eventually drops to zero at the growth rate minimum. Here Form II growth does not drop to zero only because a proportion of the covered chains can still convert. The temperature at which this occurs is T^* which is when $P_0 = 0$ and occurs when

$$B + C^* = A + D^* \tag{4.16}$$

.

This can be rearranged to produce,

$$C^* = \frac{A-B}{1-\frac{D^*}{C^*}} \quad at \quad T = T^* \tag{4.17}$$

A is determined by fitting the growth below the growth rate minimum to the growth rate of

Form I. Due to the reduced motion of the covered chains, C^* must be less than C and figure 4.6 shows a range of fittings with different ratios of C to C^*

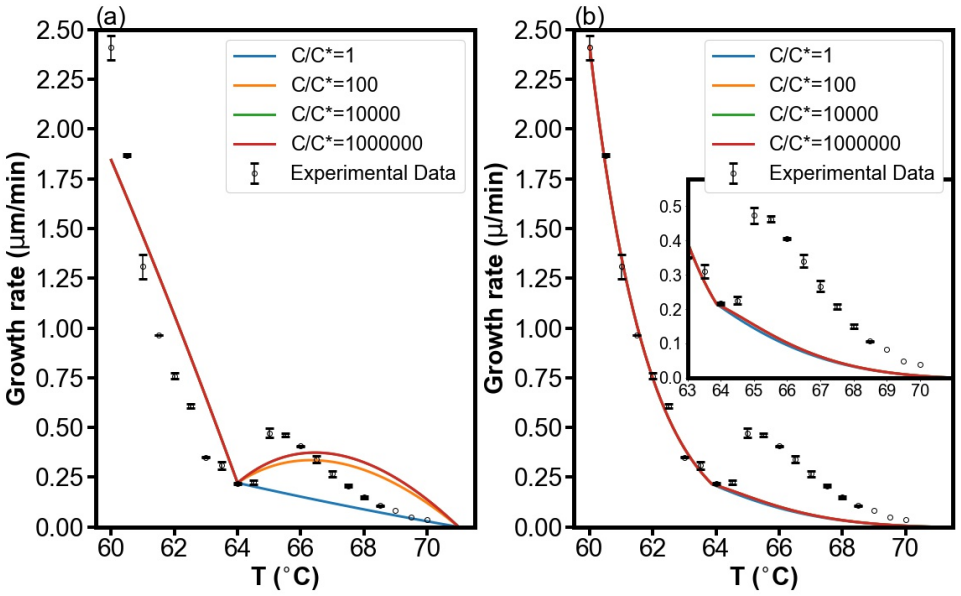

Figure 4.6: A plot of the model for Form II growing from Form I and being poisoned by Form I for PEBr21. The solid line represents the theoretical model data, and the circles are the experimental data. (a) represents the fitting with a constant A, while (b) is the plot where A has a temperature dependence. In both cases the ratio between C to C* was varied from 1, to 100, then 10000 and finally 1000000. When the two are equal the poisoning disappears, but as the ratio becomes bigger all the lines seem to merge into one and the line produce is not affected by how big the ratio becomes. There is also a general decrease in the growth rate from the model when A becomes temperature dependent in fitting of the high temperature data.

Figure 4.6(a) shows a plot of the growth rate fitted with a temperature independent A and it is unable to fit the lower temperature well. The energy required for a Form I chain to attach to the surface is proportional to the driving force and using this fact a temperature dependence can be introduced to A. This improves the fit of the model to the experimental data and gives A as,

$$A = A_0 \exp\left(u_I \Delta S_I (T_{m,I} - T)/RT\right) \tag{4.18}$$

.

Here the attachment rate at the melting point $T_{m,I}$ is given by A_0, and the driving force and the free energy are related by u_I.

Though a temperature dependent A improves the lower temperature fitting, it greatly hinders

the rate at higher temperatures and the poisoning effect. Changing the ratio of C to C^* from 1 to 10000, so that only a few covered chains can convert, does not to change the effects of the poisoning by much. In fact, making C/C^* bigger only increases the poisoning to a point beyond which it has no effect. According to figure 4.6, once $C/C^* \geq 10000$, then increasing the ratio has no effect on the fit, therefore C/C^* is fixed to be 10000 for the rest of the fits of the model. This surprising fact about the model shows that it cannot explain the poisoning by having Form II grow by conversion only.

As previously discussed, the inclusion of direct attachment of Form II violates the initial assumption posited in this model. This assumption is based on the higher entropy of Form I compared to Form II, and as such an increased chance of attachment to the a Form II growth front. However, in order to reconcile the experimental observations, it becomes necessary to accommodate an independent direct attachment of Form II chains to the growth front. This attachment only happens on clean Form II surfaces as the grow of Form II requires registry of the bromine and does not disrupt the equilibrium among all state-n states. If it is assumed that Form II chains from the melt deposit on the surface of Form II crystal at rate E and detach at rate F, with F being related to E by the free energy difference between the melt and Form II crystal, then the growth rate equation for Form II can be rewritten as,

$$G_{II} = P_1 C + (1 - P_0 - P_1)C^* - (1 - P_0)D^* - P_0(D + F - E) \tag{4.19}$$

Figure 4.7 shows that the model fits the data better when E has a temperature dependence similar to that of A, rather than for a constant E.

$$E = E_0 \exp\left(u_{II}\Delta S_{II}(T_{m,II} - T)/RT\right) \tag{4.20}$$

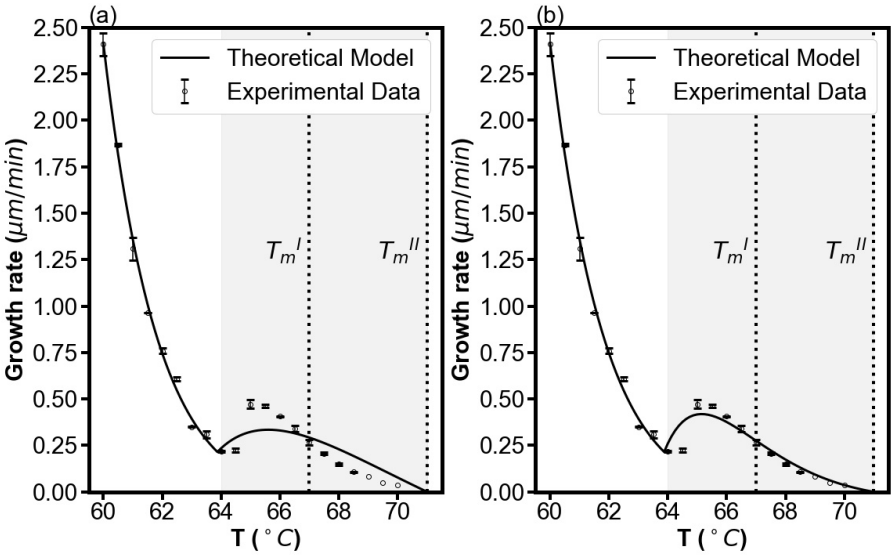

Figure 4.7: A plot of the growth rate of PEBr21 with direct attachment of Form II chains. (a) Best fit when a constant direct attachment E of Form II is assumed. It increases the total growth in the higher temperature region but does not fit the overall shape. (b) Introducing a temperature dependence E produces a much better fit.

Figure 4.8 was constructed by fitting the model to the data for PEBr15, -19 and -21 using a temperature dependent attachment rate A for Form I, and also a temperature dependent direct attachment rate E for Form II. The model fits the general detail of the experimental curves well.

PEBr	$A_0(\mu$m/min)	$E_0(\mu$m/min)	u_I	u_{II}	$C*(\mu$m/min)
15	4.22	0.205	9.16	22.2	2.66
19	0.508	0.186	9.05	11.5	2.78
21	0.434	2.82	9.52	4.78	0.994

Table 4.3: Fitting parameters to experimental growth curves of PEBr15, PEBr19, and PEBr21 for the model of self-poisoning of form II by form I. A_0 and E_0 are the attachment rates for form I and form II at their respective melting points, and u_I and u_{II} define the temperature dependence of the attachment rates on undercooling, and $C*$ is the ratio of covered form I stems at the form II crystal that convert to form II.

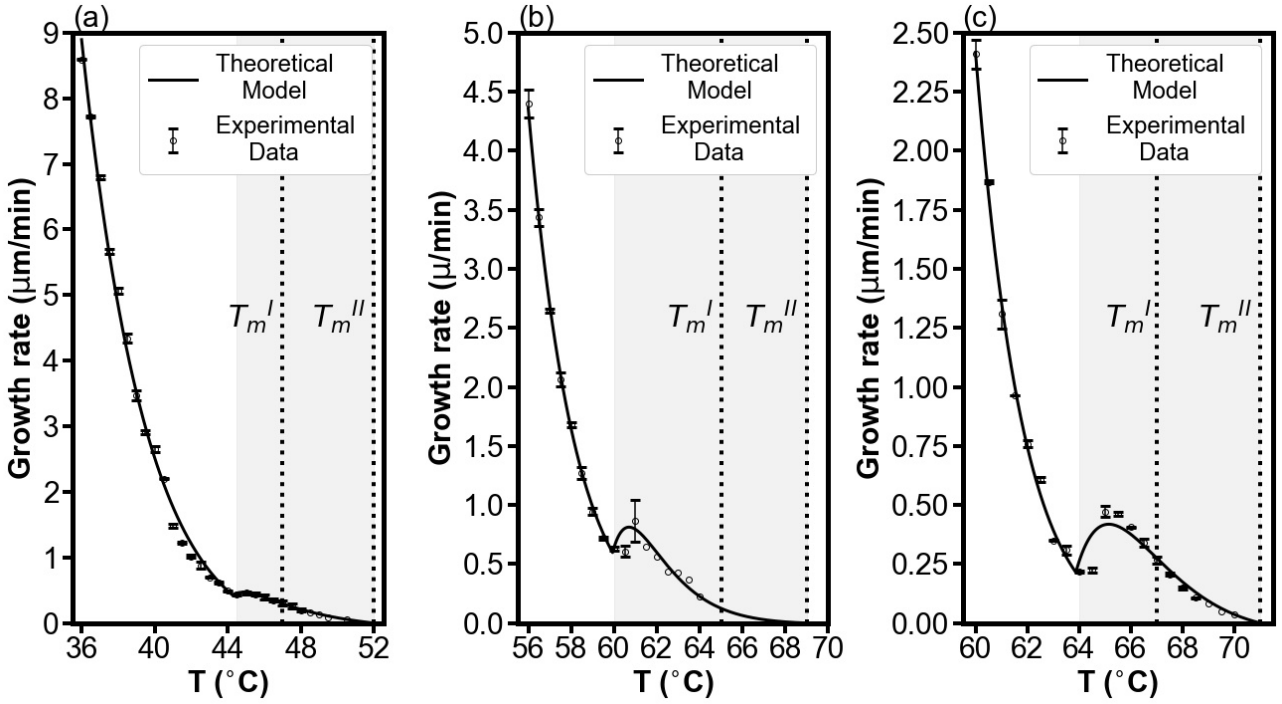

Figure 4.8: The overall growth of (a) PEBr21, (b) -19, and (c) -15 experimental data and theoretical line as produced by the model of a competition between Form I and Form II. The solid red line represents the theoretical curve from the model and the black circles the experimental data. The vertical lines represent $T_{m,I}$ (on the left), and $T_{m,II}$ (right).

For a Form II chain to attach to the growth front from the melt, E takes into consideration deposition and the bromine being in the correct registry. Whereas for a Form I chain, because of the reduced level of order there is a smaller entropy barrier to overcome. It is then expected that the rate A would be higher than E. However, on closer inspection of the rates A and E, as shown together below in figure 4.9 for the different polymers, the best-fit parameters show that E is in fact much bigger than A (several orders of magnitude) in PEBr21 and PEBr19,

and also higher around the poisoning point for PEBr15. This adds to the problems that come with model 2.

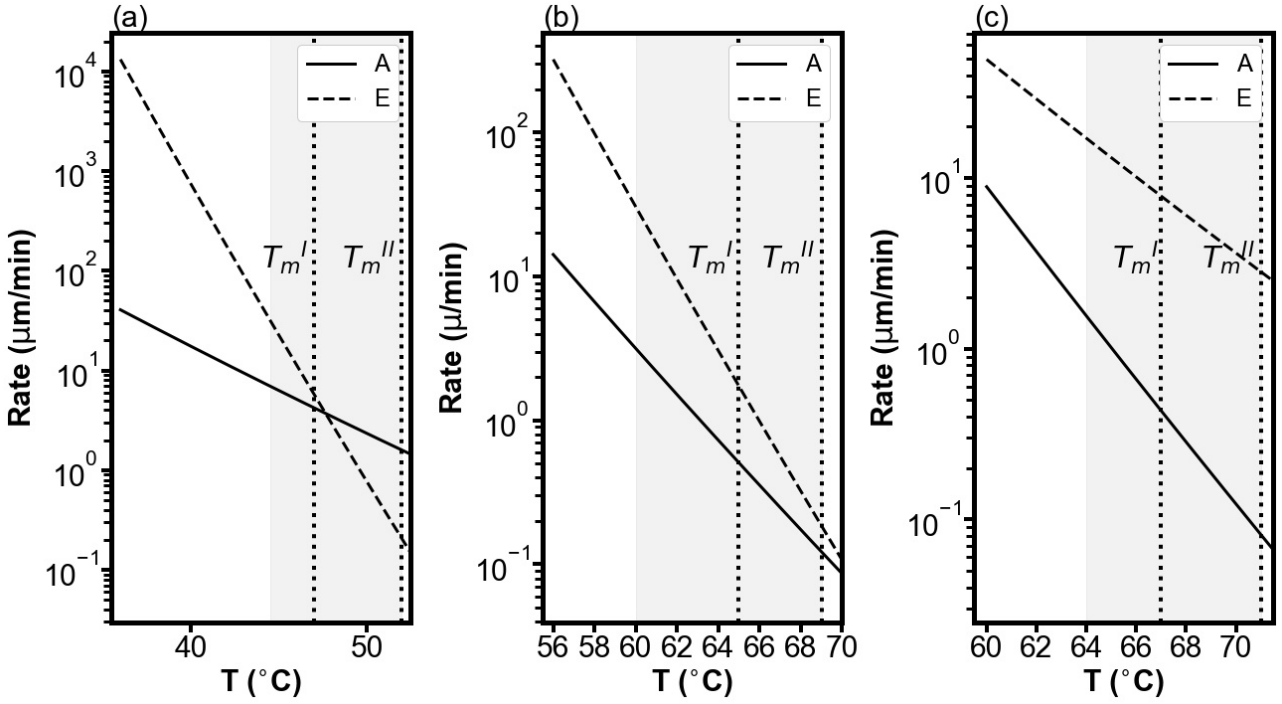

Figure 4.9: Plot of the attachment rate of Form I ,A, (solid line) and the direct attachment of Form II, E, (broken line) as functions of temperature for the three polymers. The plot shows that E is always larger than A below the poisoning in (a) PEBr15, and always larger by several orders of magnitude for (b) PEBr19 and (c) PEBr21 within the area of interest. The Plot of E is in blue, and that of A is in black. The two vertical lines show the respective melting temperatures of Form I and Form II.

4.4 Conclusion

The model of different lamellar thicknesses does a good job of producing curves that fit the trend and shapes of the curves very well. Most of the fitting parameters follow a trend, except maybe for PEBr19 which seems to have a big uncertainty at the maximum before the poisoning and that may affect the overall fitting.

An explanation of the self-poisoning in the PEBr compounds based on poisoning between Form I and Form II is very unlikely as the model fails to reproduce the experimentally observed curves unless unphysical assumptions were made. When A is temperature independent, the lower temperature fit is poor, whereas when a temperature dependency is included, the higher temperature is compromised, having a small kink instead of a clear minimum. Only by allowing

Form II chains to attach directly on a clean Form II substrate, the fitting can be improved drastically. However, this comes with an unphysical condition where the attachment rate of a more ordered Form II is much faster than that of less ordered Form I. Adding to the difficulties are the experimental observation that there is no solid-solid transition of Form I to Form II below the melting point of Form I, while our model relies on the fact Form I must convert to Form II below the poisoning point to be consistent with experimental observation that only Form II crystals were observed both above and below the poisoning point.

It is worth acknowledging that the proposed alternative depends on treating the fact the melting temperatures of Form I comes close to the poisoning region as a coincidence, and that the model does not take Form I growth into consideration. Experimentally, further x-ray diffraction (XRD) work for more accurate measurement of the crystallinity of the crystal forms formed at different temperatures and determination of the crystalline layer thickness, may in the end provide the evidence to distinguish between the two models. Molecular dynamics can also be used to complement the experimental data and study the form of the crystal produce in the polymer crystallisation of PEBr.

References

[1] Kutlwano Gabana et al. "Quantitative Model of Multiple Crystal Growth Rate Minima in Polymers with Regularly Spaced Substituent Groups". In: *Macromolecules* (2024).

[2] Masafumi Tasaki et al. "Polymorphism and phase transitions of precisely halogen-substituted polyethylene. (1) Crystal structures of various crystalline modifications of bromine-substituted polyethylene on every 21st backbone carbon". In: *Macromolecules* 47 (14 2014), pp. 4738–4749.

[3] Xiaoshi Zhang et al. "Effect of Self-Poisoning on Crystallization Kinetics of Dimorphic Precision Polyethylenes with Bromine". In: *Macromolecules* 51 (4 2018), pp. 1386–1397.

[4] Stephen Whitelam, Yuba Raj Dahal, and Jeremy D Schmit. "Minimal physical requirements for crystal growth self-poisoning". In: *Journal of Chemical Physics* 144 (2016), p. 64903.

[5] Goran Ungar and Andrew Keller. "Time-resolved synchrotron X-ray study of chain-folded crystallization of long paraffins". In: 27 (12 1986), pp. 1835–1844.

[6] G Ungar and A Keller. "Inversion of the temperature dependence of crystallization rates due to onset of chain folding". In: *Polymer* 28 (11 1987), pp. 1899–1907.

[7] Stephanie F Marxsen et al. "Crystallization Rate Minima of Poly(ethylene brassylate) at Temperatures Transitioning between Quantized Crystal Thicknesses". In: *Macromolecules* (2022).

5 Molecular Simulations of Quantised Lamellar Thickening in Polyethylenes with Regularly Spaced Brominated Groups

The work in this Chapter follows from Chapter 4, where it was suggested that the self-poisoning of PEBr -15, -19 and -21 is due to quantised lamellar thickness and not two competing forms. As no experimental results have been seen to suggest quantisation of lamellar in PEBr, molecular dynamics studies are carried out in this Chapter to study these systems further using PEBr21. The results of this work have been accepted for publication in *Macromolecules*, with the preprint available at [1].

5.1 Introduction

Polyethylene (PE) is one of the most ubiquitous and simplest homopolymers and as a result is widely studied in both academia and industry. Its straightforward structure, a linear chain of repeating ethylene units, serves as an ideal model system for understanding polymer behaviour. The simplicity of the polyethylene backbone, combined with its tunable molecular weight and degree of branching, makes it a fundamental reference for the study of polymer physics, chemistry, and material science. One of the intriguing aspects of polyethylene is its role as a precursor for functionalised derivatives. By introducing chemical groups into the polyethylene backbone, researchers can tailor the properties of the polymer for specialised applications.

A notable example of these polyethylene derived polymers is poly(ethylene bromine) (PEBr) (studied in Chapter 4), where bromine atoms are substituted in place of hydrogen every m carbons along the backbone [2], [3]. It was found that PEBr15, -19 and -21 crystallise with a minimum in a plot of their growth rate with supercooling [3]. Though it was originally suggested that the minimum was due to the growth of Form I poisoning Form II, experimental results have suggested otherwise. Form II crystal is seen to grow both below and above the poisoning, which would be unexpected if indeed Form I growth was poisoning it at high temperatures. In the previous Chapter, Chapter 4, it was suggested that the self-poisoning phenomenon arises due to quantised lamellar growth, where Form crystals of shorter stems are deposited at the growth front of Form II crystal with longer stems. A model developed to explain self-poisoning in due to quantised lamellar thickness in poly(ethylene brassylate) (Chapter 3) [4] fit the experimental data of the three PEBr polymers very well compared to one developed for self-poisoning due to different forms. However as no experimental results have shown quantisation of the lamellar thickness in PEBr, this is all just theoretical.

While experimental studies like these provide valuable insights into PEBr crystallisation, understanding the detailed molecular structure of the crystals remains a challenge. This difficulty

arises due to the semi-crystalline nature of PEBr, which consists of coexisting crystalline and amorphous regions. Structures are often inferred rather than directly observed, and traditional experimental techniques, such as X-ray scattering, provide only averaged information, lacking the resolution to capture individual chain conformations within the crystals. Furthermore, critical phenomena in polymer crystallisation such as nucleation, growth, and chain folding, are dynamic processes that remain difficult to capture experimentally, especially given the rare events like nucleus formation or defect generation.

To address these limitations, computer simulations have emerged as a powerful tool to explore the large-scale structures formed by long polymer chains [5, 6]. Advances in polymer models, high-performance molecular simulation codes [7], and computational power have enabled researchers to simulate polymer behaviour with increasing accuracy. In the case of polyethylene systems, all-atom models have been successful in reproducing the orthorhombic crystalline unit cell [8], but scaling these models to large systems remains challenging. Simulating long-chain PE crystallisation, particularly nucleating crystals from the melt, requires long run times and high computational resources, making all-atom simulations impractical for large systems. As a result coarse-grained united-atom (UA) models, in which hydrogen atoms are grouped onto into the heavier carbon atoms to reduce the number of interactions have been adopted. They offer a simplified but computationally efficient representation of the polymer chain. However, this simplification comes at the cost of not reproducing the exact crystalline unit cell of PE [9]. Despite these limitations, UA models have been widely used to study the crystalline properties of PE systems [8, 10, 11, 12]. For large-scale structures, such as semi-crystalline lamellae upwards of 10 nm, even more heavily coarse-grained models, like united-monomer models, are employed to overcome computational bottlenecks.

In this Chapter of the thesis, a united-monomer model for PEBr is developed from an existing model that was originally developed for poly-vinyl alcohol PVA [13, 14, 15, 16, 17, 18, 19] and used in several studies since. A more recent study by Fall et al. [20, 21], using a modified CG-PVA model, showed successful control over the lamellar thickness in regularly branched PE by growing crystals using a technique known as self-seeding. Their model will serve as a basis for the one used here with modifications of adding two bromine atoms every 21st carbon. The aim of the study is to investigate how the presence of regularly placed bromine atoms affect the crystallisation behaviour and semi-crystalline morphology of monodisperse PEBr21. This is to be studied by two different crystallisation methods, continuous-cooling and self-seeding, for a series of different cooling rates and crystallisation temperatures. Then the results are to be compared with current experimental results [22, 2, 23, 24].

The Chapter outlines the model development, the coarse-graining process, simulation conditions, and the two crystallisation protocols used in the study. Analytical techniques are used to compare the simulation results with experimental observations.

5.2 Model & Methods

The united-monomer model employed in this work is an extension of the renowned united-monomer model originally adapted for poly-vinyl alcohol (PVA) by Meyer and Müller-Plathe [13], and later used to capture the behaviour of a variety of macromolecules [13, 25, 20, 21]. Here C_2H_4 and $CHCBr_2$ are represented by single coarse-grained beads as denoted by the blue and red species in figure 5.1(a). The coarse-graining (CG) used in this method uses every second backbone carbon as the distribution centre, as suggested by Vettorel and Meyer [26]. By choosing this mapping scheme, instead of the centre-of-mass, cross-correlations between angles and bonds are minimised, ensuring that the angular configurations of the coarse-grained model directly correspond to those in the all-atomistic simulations [15].

5.2.1 All-Atom Simulations

The coarse-grained potentials of the CG-PE model from [20] are unchanged because the bond and radial distribution functions closely align. However, introducing bromide dimer (CH_2CBr_2) required new all-atom simulations. Like in CG-PE, the Optimized Potentials for Liquid Simulations (OPLS) force field from Jorgensen et al [27] was employed with the modification that the leading torsional term was reduced from 1.76 to 0.8 kcal/mol. This modification came about to address the well known problem that OPLS all-atom (OPLS-AA) simulations overestimates crystallisation temperatures due to its elevated gauche energy for backbone torsions, which favours the extended conformation. The AA simulations of $C_{10}H_{21}CBr_2C_9H_{19}$ were conducted identically to those of the CG-PE model at 500K, well above the melting point. The bromide dimers were adjusted only in terms of the size of Br units and $C-Br$ bond lengths, based on halogen parameters from Jorgensen and Schyman [28], while the modified torsional potential of OPLS-AA was applied across the entire backbone.

5.2.2 Coarse-Grained Model Development

In the united-monomer model, each bead is linked to its adjacent beads through harmonic bond potentials, described by the equation:

$$U_{\text{bond}} = k_{\text{bond}}(l - l_0)^2 \tag{5.1}$$

where U_{bond} represents the change in potential energy as the bond between the beads stretches or compresses. Here, k_{bond} is the spring constant, l is the current bond length, and l_0 is the bond's equilibrium length. The parameters used for the model in this study can be found in table 5.1

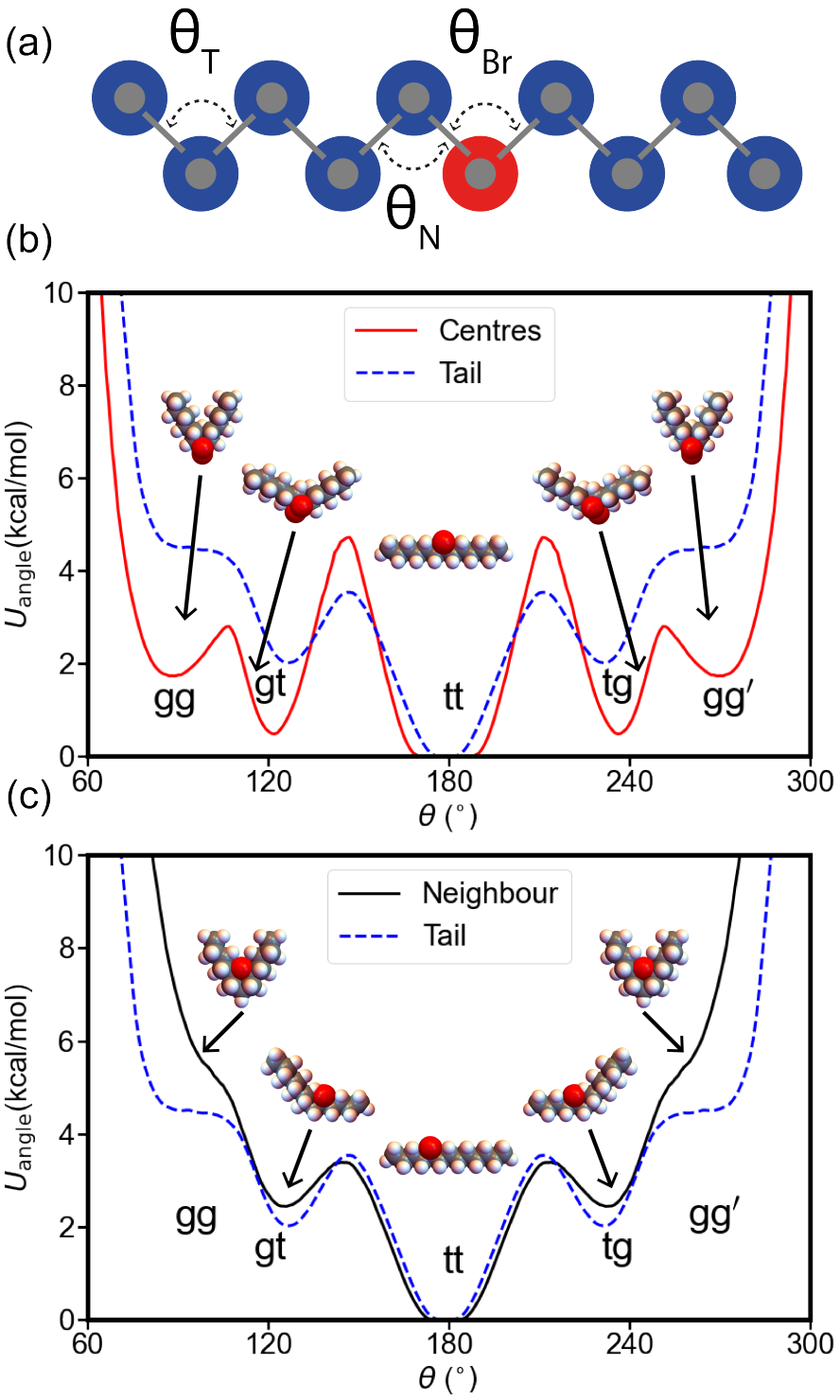

Figure 5.1: Coarse-grained model and angular potentials. (a) Schematic representation of the coarse-grained model for PE, blue and red beads represent C_2H_4 and CH_2CBr_2 CG centres respectively. Different bending potentials considered between bromine centres, their immediate neighbours and tails, namely θ_{Br}, θ_N and θ_T are drawn in. (b-c) Mapping from an all-atom torsional potential to CG tabulated angular potential, for the bromine centres ($U(\theta_{Br})$, red curve) and their neighbours ($U(\theta_N)$, black curve) respectively shown alongside the potential of the tail groups. Note the angular potential of the tails ($U(\theta_T)$, dashed blue curve) is identical to that of regular polyethylene reported previously [20]. The minima of the CG potentials map to real all-atom conformers of precision PE chains as depicted in the inset artistic representations at each of the respective minima. Taken from [1]

	Interaction	Form	Parameters
Bonds	(C_2H_4)-(C_2H_4) (CH_2CBr_2)-(C_2H_4)	$U_{\text{bond}}(l)$	k_{bond}=53.69 (kcal/mol/Å^2) l_0=2.225 (Å)
Angles	(C_2H_4)-(C_2H_4)-(C_2H_4)	Tabulated	figure1(b,c)-Tails (blue)
	(C_2H_4)-(C_2H_4)-(CH_2CBr_2)	Tabulated	figure1(c)-neighbours (black)
	(C_2H_4)-(CH_2CBr_2)-(C_2H_4)	Tabulated	figure1(b)-Centres (red)
Non-Bonded	$(C_2H_4)\leftrightarrow(C_2H_4)$	$U_{\text{LJ}}^{(9\text{-}6)}$	ϵ_0=0.348 (kcal/mol) σ_0=4.45 (Å) $r_c = (3/2)^{\frac{1}{3}}\sigma_0$
	$(CH_2CBr_2)\leftrightarrow(C_2H_4)$		ϵ_0=0.44 (kcal/mol) σ_0=5.19 (Å) $r_c = 1.5^{\frac{1}{3}}\sigma_0$
	$(CH_2CBr_2)\leftrightarrow(CH_2CBr_2)$	$U_{\text{LJ}}^{(12\text{-}6)}$	ϵ_0=0.45 (kcal/mol) σ_0=5.66 (Å) $r_c = 2^{\frac{1}{6}}\sigma_0$

Table 5.1: Potential forms and parameter values for the united-monomer model of PE with dibromo groups in real units. [1]

As in the PE paper [20], the bending valences in this work were derived from the Boltzmann inversion (described in Chapter 2) of the bond angle distribution, $P(\theta)$, observed between coarse-grained (CG) centers in all-atom simulations. This method inverts the bond angle probability distribution $P(\theta)$ to generate the bending potential

$$U_{\text{angle}}(\theta) = -k_B T \ln\left[P(\theta)/\sin(\theta)\right] \tag{5.2}$$

Consequently, torsional angles from the atomistic model are converted into effective angular potentials between every three consecutive CG beads, leading to the tabulated potential displayed as the dashed blue line in figure 5.1(b) and (c). The inclusion of additional dibromo groups necessitated the introduction of two new angular distributions: one centred on the dibromo group itself and the other adjacent to it (referred to as 'Centres' and 'Neighbours'), in addition to the standard PE chain (referred to as 'Tails'), whose properties are already established in the united-monomer model of PE. Notably, further angular distributions were unnecessary, as the bond angle distribution quickly reverted to that of standard PE with increasing distance from the Br group. The angular potentials in proximity to the Br dimer preserve the characteristic triple-well structure of the standard PE model, though the gauche-gauche configuration is more strongly disfavoured, marked by a pronounced shoulder at lower angles in the black curve in figure 5.1(c).

A key variation arises at the Br group itself, which exhibits a quintuple-well potential, as shown by the red curve in figure 5.1(b), with a deeper minimum at the gauche-gauche state and a larger torsional barrier between the trans-gauche and trans-trans states. This leads to a greater likelihood of chain bending at the Br group while disfavouring such conformations

at neighbouring monomers. This result aligns with experimental observations of chevron-like crystal structures, which feature consistent Br atom counts between adjacent chevrons, indicating a strong propensity for bending at CBr_2 units [2, 3]. These findings are corroborated by inspecting the conformations along the atomistic chain, as depicted in the inset diagrams in Figs. 5.1(b) and (c). It's noteworthy that gauche-gauche and gauche-trans conformations near the dibromo group push neighbouring hydrogen atoms further from the bulky Br group, whereas when the Br group is positioned on a neighbouring monomer, the H and Br atoms are forced closer together in a gauche-gauche conformation, which explains the prominent shoulder at smaller angles.

Beads that are not directly bonded along the chain, as well as those from different chains, interact through either a 9-6 or 12-6 Lennard-Jones (LJ) potential, see table 5.1 for the fitting parameters. The equations for the 9-6 and 12-6 LJ potentials, respectively are:.

$$\mathrm{U}_{\mathrm{LJ}}^{(9\text{-}6)} = 4\epsilon_0 \left[\left(\frac{\sigma_0}{\mathrm{r}} \right)^9 - \left(\frac{\sigma_0}{\mathrm{r}} \right)^6 \right], \quad \mathrm{r} \leq \mathrm{r_c}, \tag{5.3}$$

$$\mathrm{U}_{\mathrm{LJ}}^{(12\text{-}6)} = 4\epsilon_0 \left[\left(\frac{\sigma_0}{\mathrm{r}} \right)^{12} - \left(\frac{\sigma_0}{\mathrm{r}} \right)^6 \right], \quad \mathrm{r} \leq \mathrm{r_c}, \tag{5.4}$$

where ϵ_0 is the depth of the potential well, σ_0 is the particle size (or zero-crossing distance), r is the distance between particles, and r_c is the cutoff distance.

The exclusion of 1-2 interactions arises from the tubular configuration of the backbone, which is a direct consequence of the choice of CG centers during coarse-graining. Neighbouring beads overlap, and including 1-2 non-bonded interactions would result in large, unphysical forces, so these interactions are switched off. Additionally, 1-3 interactions are omitted because the steep barriers in the bending potential at small angles prevent the beads from coming close enough to interact (see figure 5.1(b)).

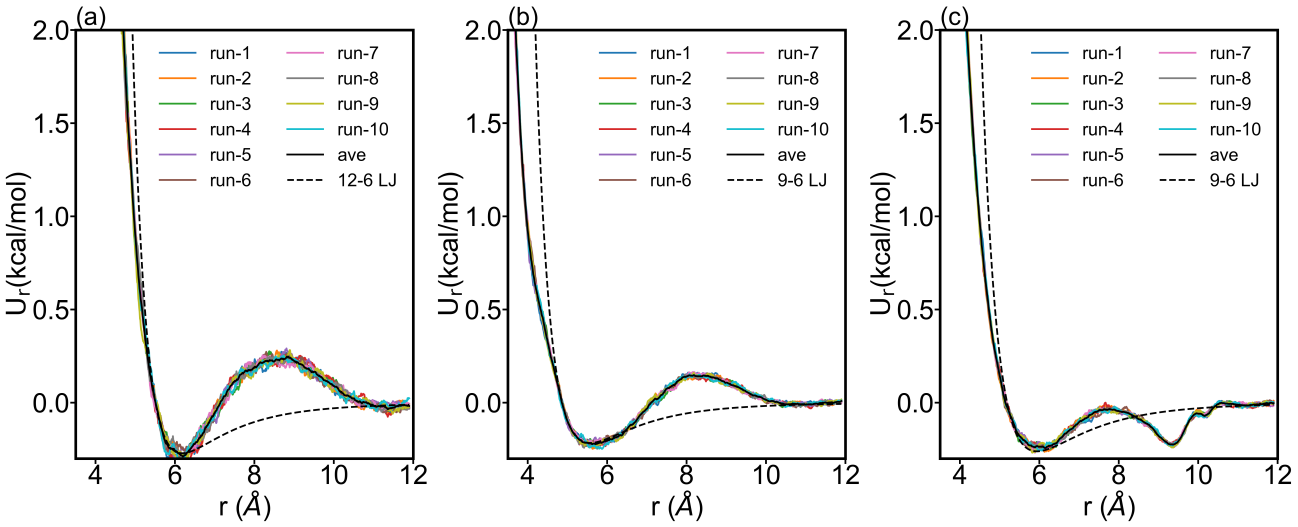

Figure 5.2: Non-bonded beads Lennard-Jones. (a) A Plot of the Boltzmann inverted non-bonded interaction potentials between bromine centres, while (b) shows that between the bromine centres and the carbon chain without the bromine, and lastly, (c) shows that between the carbons without the bromine. The average potential was calculated from the iterative runs (labelled run in the plot), and then the the Lennard-Jones fitted accordingly (shown as a broken line). The well is deepest for the bromine-bromine interactions and shallowest for the mixed interaction. Taken from [1]

Both the standard polyethylene (PE) chain (tails) and the mixed interactions between brominated (centre) and PE (tail) groups are represented by pairwise 9-6 LJ potentials 5.3. These potentials are largely similar, though the mixed interactions between Br and PE groups have a slightly deeper minimum that is shifted to larger distances to account for the larger size of the Br atoms. A 9-6 LJ potential is chosen to model the softer effective interactions between united-monomers. For interactions between two brominated groups, a 12-6 LJ potential is more suited, which provides a more accurate representation of the CH_2CBr_2 CG units, compared to C_2H_4, with a deeper potential minimum and a larger equilibrium separation. Both the 9-6 and 12-6 potentials are cut and shifted to zero at their respective cutoff distances r_c, as shown in table 5.1, ensuring only repulsive interactions between the CG beads are considered.

This methodology has been proven effective for crystallisation studies, where only the repulsive portion of the potential is used. It has been successfully applied to quiescent systems [16, 17, 13, 14, 20], and recent simulations have reported the largest multi-lamella polymer crystals to date for PE [21]. We follow this well-established approach here. Electrostatics are not included explicitly in the model, as the monomer carries no net charge. While more precise potentials could be generated for specific state points via iterative Boltzmann inversion with tabulated potentials, this was not pursued in the current study. It is possible that brominated units may behave differently below the 500 K temperature at which this model was parameterised. Nevertheless, the crystallisation temperatures of the brominated PE chains in this study align

closely with experimental results [2, 3], as we will demonstrate in the next section. This indicates that the model successfully captures the essential physical behaviour of brominated PE crystallisation.

5.2.3 The Simulations

The simulations comprise 96 chains, each consisting of 200 coarse-grained (CG) units, with bromide units inserted at every 10th or 11th CG unit along the chain. This specific arrangement was selected to maintain a direct correspondence between the CG chain and the all-atomistic conformations of PEBr21, as outlined in [3], in anticipation of future studies where atomistic monomers may be reintroduced into the large-scale structures obtained here. Initial topologies were derived from simulations of polyethylene melts detailed in, ensuring that they were already well equilibrated. Bromide units were subsequently introduced regularly along the linear backbone. It was demonstrated in [20] for the insertion of small butyl branches, that the addition of a few small units causes minimal perturbation.

All equilibration and crystallisation runs were conducted using the Large-Scale Atomic/Molecular Massively Parallel Simulator (LAMMPS) [7, 29]. Following the insertion of bromide monomers into the existing PE melt, a brief equilibration run was carried out to allow the chains to fully relax in the NPT ensemble (where the number of chains (N), the pressure (P), and the temperature (T) are all constant) using a Langevin thermostat with a coupling constant $\Gamma = 0.5$ $(1/\tau)$ and a Berendsen barostat with $P_{\text{damp}} = 100.0$ (τ). The integration timestep used throughout was 0.005 τ, where the LJ-time unit $\tau = \sqrt{m\sigma^2/k_{\text{B}}T_0}$ corresponds to 2.7 ps (m = 27.3881 g/mol), and the temperature was maintained at $\text{T}_0 = 500K$ or 227°C (T = 1.0 in reduced units). A high pressure of P = 8.0 $(k_{\text{B}}T_0/\sigma^3)$ was applied to achieve the desired density. During crystallisation runs, a Nosé-Hoover thermostat and barostat were employed for cooling and self-seeding runs, with $T_{\text{damp}} = 2.0$ (τ) and $P_{\text{damp}} = 100.0$ (τ), respectively.

The initial all-atom simulations were ran on High Performance Computing Center CAIUS of the University of Strasbourg, with 24 CPU cores for 135 ns over 100 hours in real life. The subsequent coarse-grained isothermal and cooling (heating) runs were performed on the now decommissioned ShARH HPC cluster on 16 CPU cores. The isothermal and cooling runs were done using multiple packages, each with taking over 15 hours in real life.

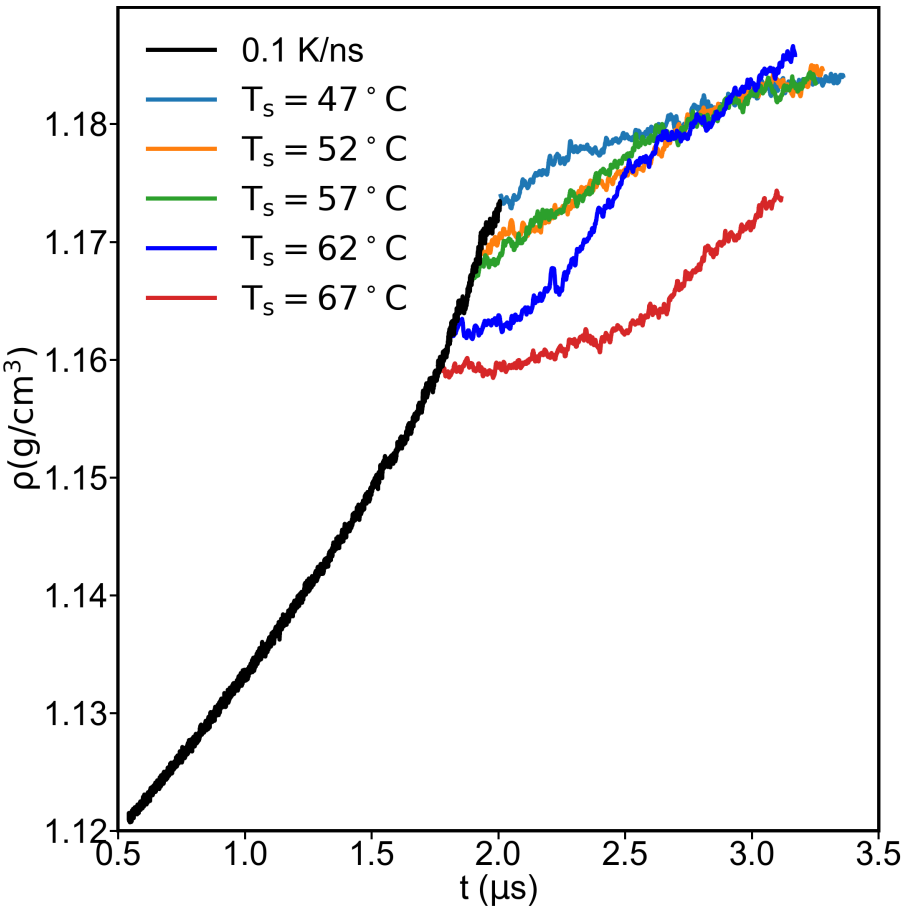

Figure 5.3: Density - time curves for potential seeding temperatures.

This study employed two methods of crystallisation to generate crystal structures: continuous-cooling and self-seeding. The continuous cooling protocol involves rapidly cooling the melt from a higher temperature to a lower temperature at a specified rate. In this case, a well-equilibrated melt at 227°C was quenched to 0°C at rates of 0.1 K/ns and 0.4 K/ns, respectively. Additionally, slower cooling rates of 0.04 K/ns and 0.01 K/ns were employed from a melt cooled to 127°C at 0.4 K/ns. Continuous cooling is suitable for short-chain polymers; however, when long chains are present, it can result in multiple nuclei and several disordered amorphous regions, leading to poor crystal structure.

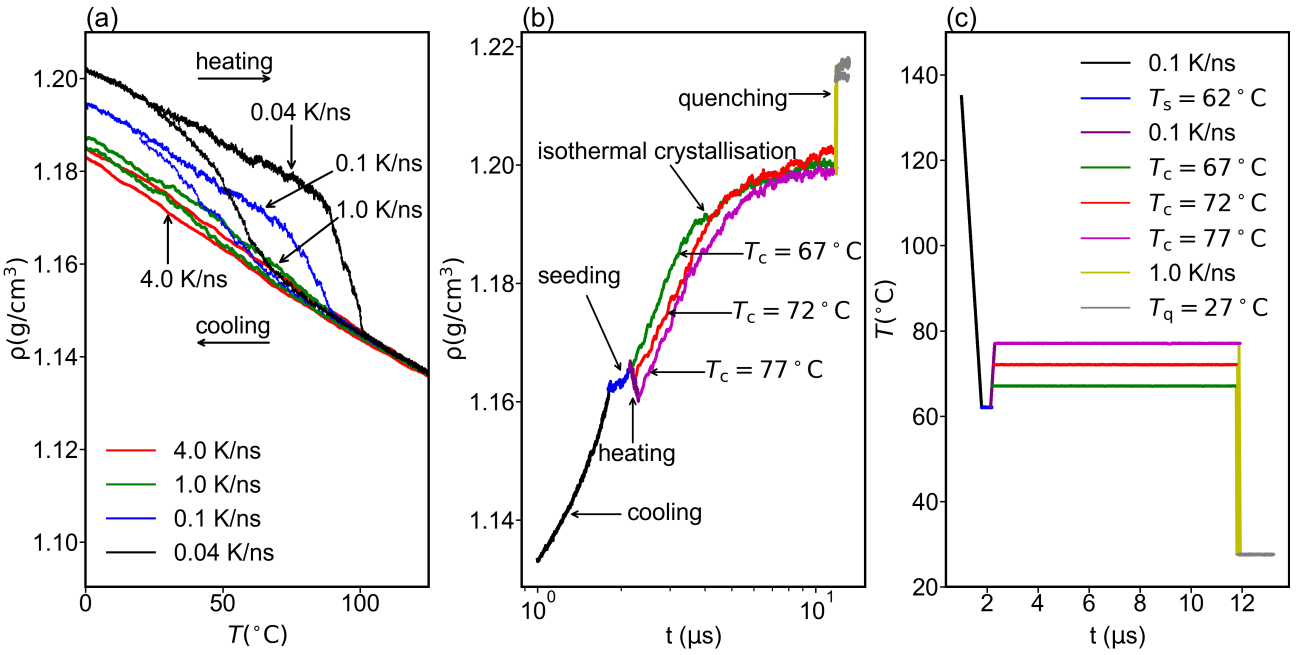

Figure 5.4: Density curves for all systems during the self-seeding and continuous-cooling simulations. (a) Density-temperature curves for the continuous-cooling starting from 125°C to 0°C with four different rates and their corresponding heating curves. The 0.1 K/ns and 0.04 K/ns cooling were bifurcated from the 1.0 K/ns cooling at 127 °C. (b) Density-time curves during the self-seeding procedure. Each respective cooling, seeding, heating, crystallisation or quenching stage is indicated in the figure with arrows. The seeding (blue) curve is bifurcated from the 0.1 K/ns cooling (black) curve at $T_s = 62$ °C. This is followed by a 0.1 K/ns heating (purple curve) to a series of crystallisation temperatures $T_c = 67$°C, 72°C and 77°C (green, red and pink curves) respectively at which the systems are held for 0.4μs and then quenched (yellow curve) to 27°C at 1.0 K/ns. Note the 0.1 K/ns cooling curve begins at $\sim 1\mu$s due to bifurcation from the faster 1.0 K/ns cooling at 127 °C for computational expedience. The corresponding time-temperature protocol is similarly shown in panel (c). From [1]

The second method, self-seeding, was used to address the shortcomings of continuous cooling. This process initiates crystallisation through existing crystalline structures within the polymer. The time-temperature protocol for self-seeding employed in this study is depicted in Fig 5.4 (c). Initially, the system is cooled steadily at a rate of 0.1 K/ns (represented by the black curve) until it reaches the seeding temperature, T_s. At this point, the system is held at a constant temperature (blue curve) for several hundred nanoseconds, allowing crystallisation to begin. Various temperatures were initially tested for isothermal crystallisation by branching from the cooling curve 5.3. The most effective crystallisation occurred at 62°C, which was thus selected as the seeding temperature.

Once sufficient nuclei had formed, the system was heated at a constant rate of 0.1 K/ns (purple

curve) to a set of crystallisation temperatures T_c, causing most of the nuclei to melt. Following this, another isothermal crystallisation step was conducted for several microseconds until the system's density stabilised, indicating that the remaining nuclei had fully grown and filled the simulation box. After crystallisation at the various T_c, the systems were quenched to room temperature ($T_q = 27°C$ at a rate of 1.0 K/ns to gather data for statistical analysis. This self-seeding method enabled the growth of highly pure crystals, which allowed for a direct comparison with recent experimental findings on competing polymorphs in periodically spaced PEBr polymers.

5.3 Results & Discussion

Figure 5.4(a) displays the density-temperature profiles obtained during continuous cooling for all cooling rates tested, spanning two orders of magnitude. The fastest cooling rate of 4.0 K/ns (red curve) shows minimal hysteresis, which implies the absence of crystalline regions and an almost fully amorphous structure. This is in contrast to simulations of linear PE chains [20, 14], where rapid cooling induces at least some crystallisation. The presence of regularly spaced Br units along the PE chains makes nucleation significantly more difficult. With a slower cooling rate of 1.0 K/ns (green curve), some slight hysteresis emerges, indicating limited crystallisation and the lack of well-defined crystalline structures, that is, the chains have not adopted an orderly arrangement. Only at the slowest cooling rates feasible within simulation timescales, 0.1 K/ns and 0.04 K/ns, does significant hysteresis become apparent, as shown by the blue and black curves in Fig 5.4 (a). The density gradually increases as the cooling rate slows down, consistent with previous simulation studies [20]. However, the crystals formed via continuous cooling remain of poor quality. To address this and to grow PEBr crystals that closely resemble those observed experimentally, a self-seeding crystallisation approach is employed in this work.

As detailed earlier, self-seeding was used to carry out isothermal crystallisation for over 4 μs at three different temperatures: 67 °C, 72 °C, and 77 °C, as shown by the green, red, and purple curves in Figure 5.4(b), respectively. The crystals obtained through continuous cooling were inferior in quality when compared to those grown using self-seeding. The density and degree of crystallinity achieved at the crystallisation temperature closely match those of continuously cooled systems measured at room temperature. The self-seeding process also leads to a more rapid crystallisation, as indicated by the sharp change in the slope of the density curves. Furthermore, upon quenching to room temperature, the density of the self-seeded crystals surpasses that of the continuously cooled systems, which is an indicator of improved crystallisation quality.

5.3.1 Snapshots of the Systems

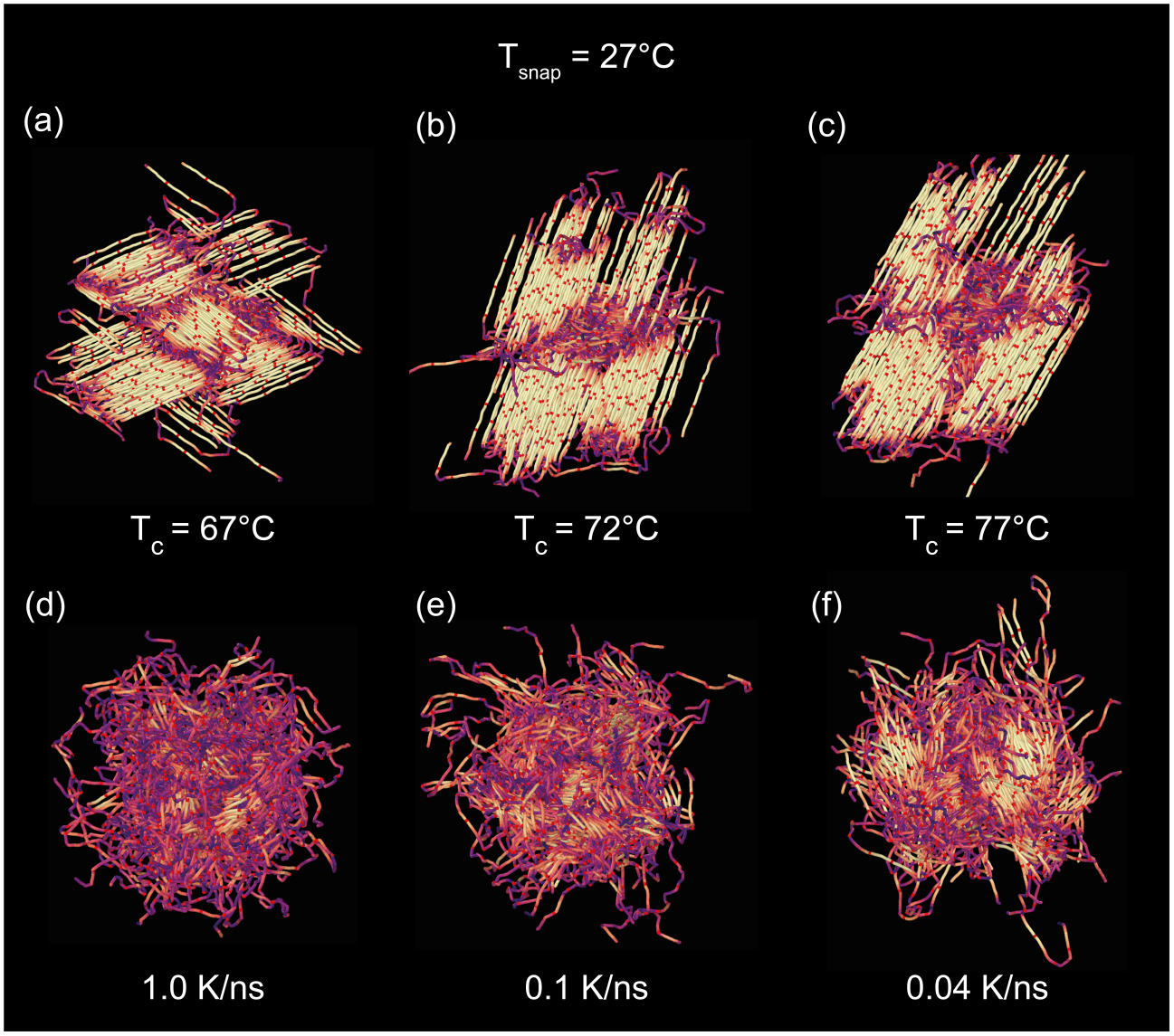

Figure 5.5: Snapshots of the continuously cooled and self-seeded systems at 27 °C. Panels (a-c) show the self-seeded crystals, grown at 67 °C, 72 °C and 77 °C respectively, after quenching. Panels (d-f) show the crystals grown by continuous-cooling. Polymer chains are coloured continuously according to their local P_2 order parameter from $P_2 = 0$ (purple, amorphous) to $P_2 = 1$ (yellow, crystalline) and the bromine species is shown in red. Adapted from [1]

The distinction between the two crystallisation protocols becomes clearer when we compare the final snapshots from the simulations, depicted in figure 5.5. In these images, the polymer

chains are colour-coded based on their local P_2 order parameter, which quantifies the degree of alignment in the system. Mathematically, P_2 is defined as the second Legendre polynomial of the cosine of the angle between a particle's orientation and a reference axis:

$$P_2 = \frac{\langle 3\cos^2\theta - 1\rangle}{2} \tag{5.5}$$

Here, the angular brackets $\langle\rangle$ denote an average over all particles in a given local region. The colour gradient used to represent P_2 ranges from $P_2 = 0$ (purple, indicating amorphous regions) to $P_2 = 1$ (yellow, indicating crystalline regions), with bromine atoms marked in red as used in [21].

In the continuous-cooling protocol (figure 5.5(d-f)), large disordered regions are observed, particularly at the faster cooling rates, as shown in the snapshot for 1.0 K/ns in panel (d). These disorganised structures likely form due to multiple nuclei growing in different directions and interfering with each other, preventing further crystalline growth. Additionally, because the cooling rate is so rapid, nucleation tends to occur at lower temperatures, where chain mobility is significantly reduced, leading to suboptimal crystallisation. In the case of the system cooled at 1.0 K/ns, the cooling rate seems to have been fast enough to nearly suppress nucleation entirely. Slower cooling rates, such as 0.1 K/ns and 0.04 K/ns, result in improved crystallinity, as evident in panels (e) and (f), respectively. This trend is expected, as slower cooling provides the chains more time to rearrange into ordered structures. The slowest cooling rate, 0.04 K/ns, produces the most crystallised regions with some chain alignment, but the overall structure remains largely amorphous.

Interestingly, in previous studies of linear PE chains, crystallisation began at much higher temperatures, around 105°C, whereas the brominated PE chains in this study only start crystallising below 70°C [20]. This observation aligns well with experimental data, which report peak crystallisation temperatures around 52°C and melting temperatures near 70°C. Considering the coarse-grained nature of the model and the finite-size effects commonly encountered in polymer crystallisation simulations, it is noteworthy that the characteristic temperatures reported here agree closely with experimental findings, as shown in figure 5.4(a) and (b).

The snapshots from the self-seeding protocol shown in panels (a-c) show a big jump in difference, with highly organized lamellar structures with large crystalline chain stems and distinct amorphous regions at the edges. For the systems crystallised at 72°C and 77°C (panels b and c), the crystal structure nearly occupies the entire simulation box, and the crystalline chain stems are globally aligned in the same direction. However, at 67°C (panel a), two large crystalline regions appear to have grown simultaneously but in perpendicular directions. This suggests the presence of two large nuclei after the system was heated from the seeding temperature, which grew in different orientations and eventually collided, preventing one region from fully consuming the simulation cell.

5.3.2 Stem Length Distribution

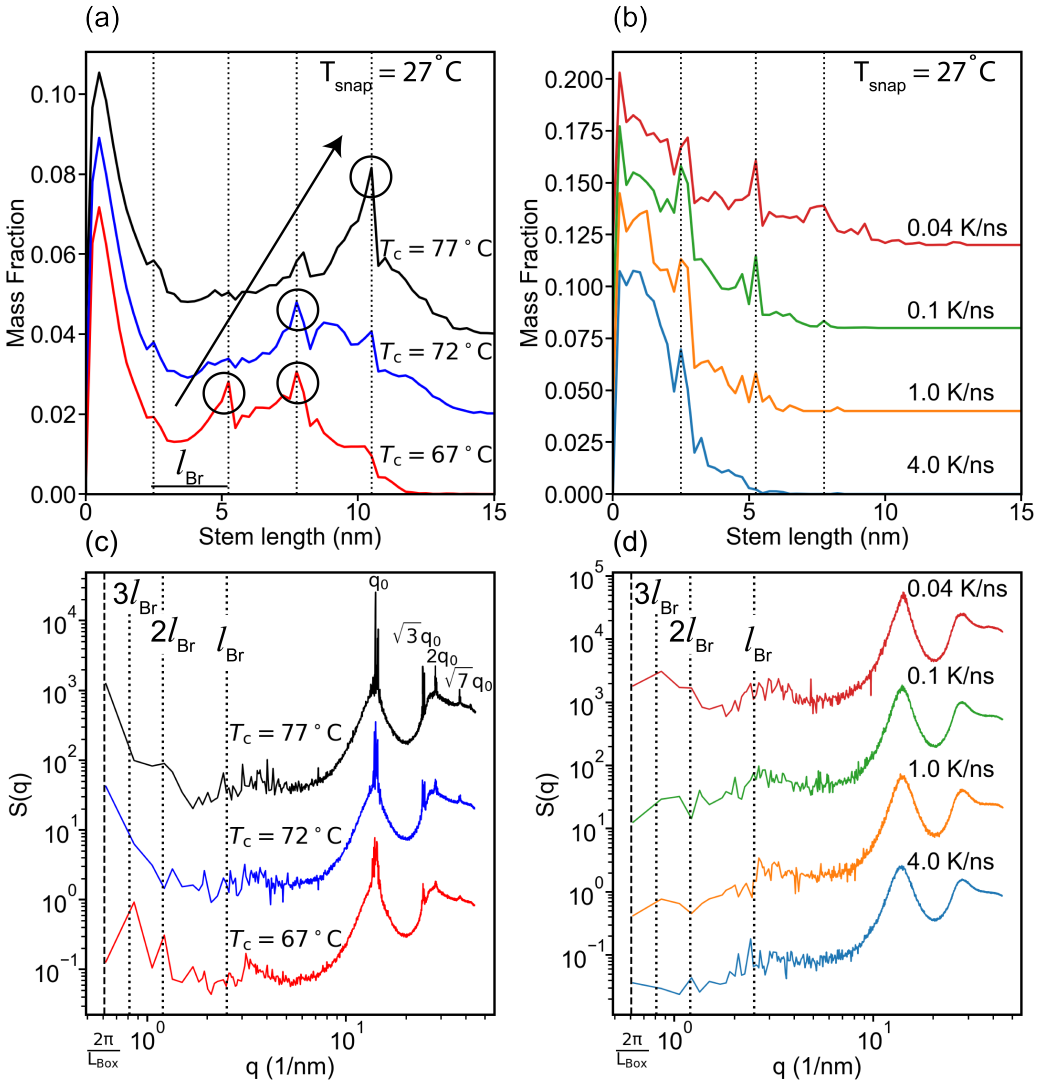

Figure 5.6: Stem length distributions and static structure factors for all systems at the end of the continuous-cooling and for the self-seeding runs at 27°C. Panels (a) and (b) show stem length distributions of all systems at the end of the self-seeding and continuous-cooling protocols respectively. The dotted lines represent the distance between neighbouring bromines l_{Br}, along the chains. Panels (c) and (d) show the static structure factors after self-seeding and continuous-cooling at 27 °C respectively. The dashed line represents the limit of the simulation box corresponding to $2\pi/L_{box}$, dotted lines indicate the distance between neighbouring bromines l_{Br} in the SAXS region of the structure factor and q_0 the hexagonal lattice parameter. From [1]

To further analyse the crystallisation behaviour of different systems, the distribution of stem lengths and their structure factors are assessed, as shown in figure 5.6. The stem length distributions are determined by evaluating the local bond vector alignment using the local P_2 order parameter, a common tool in simulations of polyethylene crystallisation to assess chain ordering [21]. These distributions represent the number of consecutive bonds that remain unbroken in nearly straight chain segments, where the bond angle falls within a range of approximately 150° to 180°. This analysis highlights differences between systems crystallised at various temperatures and contrasts the crystallisation outcomes between the self-seeding and continuous-cooling methods.

Figures 5.6(a) and (b) illustrate the stem length distributions for the self-seeded and continuously cooled systems, respectively. For clarity, each curve is vertically offset on the y-axis by intervals of 0.02 for easier comparison. A key observation is that these distributions display distinct peaks, corresponding to integer multiples of the spacing between neighbouring dibromos, indicated by vertical dotted lines. Additionally, as the crystallisation temperature increases, the stem lengths shift to longer values, reflecting the traditional lamellar thickening associated with higher crystallisation temperatures, but now in discrete steps. For example, the system crystallised at $T_c = 67°C$ (red curve) shows two peaks, at 2 and 3 bromine segments, approximately 5 nm and 7.5 nm in length, respectively. This likely results from the presence of two differently oriented crystalline domains, as seen in the snapshots in figure 5.5 (a).

When the crystallisation temperature is raised to $T_c = 72°C$, the stem lengths increase, as shown by the blue curve. The most prominent peak shifts to 3 bromine segments (around 7.5 nm), with a secondary, smaller peak at 4 bromine segments (around 11 nm). This trend is consistent with the stabilisation of longer stems at higher crystallisation temperatures, a process that appears to be governed by preferential folding at bromine groups along the chain. While chain entanglements typically influence lamellar thickness, their role here is likely minor due to the short, monodisperse nature of the chains. Although entanglements are present, the primary factor dictating lamellar thickness seems to be the controlled folding at bromine units, as demonstrated in both experimental studies [2, 3] and, for the first time, in simulations. At $T_c = 77°C$, most stems further extend into the 4 bromine segment range (around 11 nm), reinforcing this observation.

In contrast, the continuously cooled systems exhibit markedly different stem length distributions. Weakly defined peaks are only evident for the slowest cooling rates (<1.0 K/ns), corresponding to 1 and 2 bromine segments (approximately 2.5 nm and 5 nm). The stem length distributions in these systems drop off rapidly, following a power-law pattern, with broader and less pronounced peaks compared to those in the self-seeded systems. This indicates that fewer stems grow and that most chains form shorter, less ordered crystal domains.

Notably, this distinct quantised lamellar thickening has not been observed in previous molecular simulations. In linear PE chains, lamellar thickening usually occurs gradually, producing a Gaussian-like distribution of chain lengths rather than the discrete, quantised pattern seen

here.

5.3.3 Static Structure Factor

This behaviour is further validated by analysing the static structure factor, defined as:

$$S(q) = \frac{1}{M_{\text{tot}}} \langle \sum_{i,j=1}^{M_{\text{tot}}} \exp(i \cdot q \cdot (r_i - r_j)) \rangle_{|q|=q\pm dq}, \tag{5.6}$$

where the sum runs over all monomers in the system, with $M_{\text{tot}} = M \cdot N$, representing the total number of monomers, M being the number of chains and N the monomers per chain. The angular brackets denote averaging over all q-vectors within a range of $q \pm dq$. A running average is applied up to the box size, which is 10.3 nm. Since only q-vectors fitting within the finite simulation box are considered, accuracy decreases as inverse q approaches the box dimensions. The analysis covers both SAXS (small-angle X-ray scattering) and WAXS (wide-angle X-ray scattering) ranges to capture both large-scale crystal features and finer atomic structures. The curves are arbitrarily shifted along the y-axis on a logarithmic scale for easier comparison between systems.

In the WAXS range, sharp peaks emerge, indicating the harmonics of the hexagonal lattice. For the self-seeded systems, the first distinct peak, q_0, appears at q = 13.98, 14.1, and 14.1 nm^{-1} for T_c = 67°C, 72°C, and 77°C, respectively. These values correspond to an interchain distance of approximately 0.45 nm, which is typical for crystalline polyethylene (PE) and the hexagonal rotator phase observed in n-alkanes. Higher harmonics also appear at $\sqrt{3}, 2$, and $\sqrt{7}$ times the value of q_0.

In contrast, the hexagonal lattice is only weakly expressed in the continuously cooled systems. A single diffuse peak appears at q = 13.7, 13.98, and 14.14 nm^{-1} for the 1.0 K/ns, 0.1 K/ns, and 0.04 K/ns cooling rates, respectively. The disappearance of higher harmonics reflects the poorly ordered crystalline structures and lack of periodicity within these systems.

In the SAXS range, although the analysis becomes noisy as inverse q nears the box size, strong peaks can still be identified that correspond to different stem lengths. These peaks are particularly prominent in the self-seeded systems (panel c), where the positions of the peaks align well with those predicted by the stem length distribution. However, since stem lengths represent an average, some peaks do not match perfectly with the expected positions, which are marked by the dotted lines indicating the distances between successive bromine atoms along the polymer chains. For the slowest continuously cooled system (panel d), these peaks appear faintly, while they are entirely absent for faster cooling rates, reflecting the lack of long-range order in those systems.

5.3.4 Chain conformations

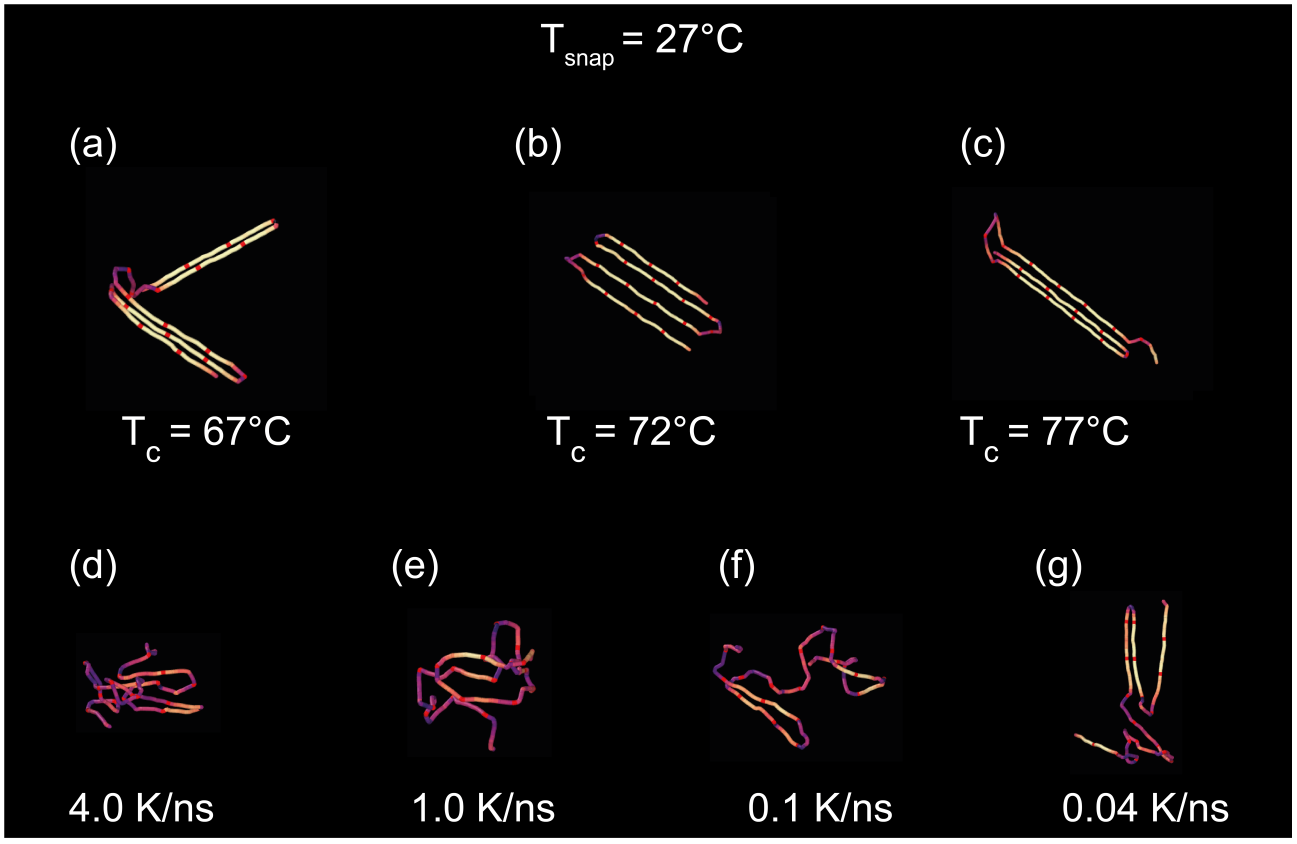

Figure 5.7: Snapshots of typical chain conformations in the self-seeded and continuously-cooled crystals at room temperature, 27°C. Panels (a-c) correspond to systems crystallised at 67°C, 72°C and 77°C and panels (d-f) correspond to cooling rates 1.0K/ns, 0.1K/ns and 0.04K/ns respectively. Polymer chains are coloured continuously according to their local P_2 order parameter from $P_2 = 0$ (purple, amorphous) to $P_2 = 1$ (yellow, crystalline) and the bromine species is shown in red. Note the pronounced folding at dibromo groups and increasing stem lengths with crystallisation temperature in panels (a-c) not present in the continuously cooled systems. Taken from [1]

The controlled folding observed in the stem length distributions and structure factors from figure 5.6 is further made clear by examining the conformations of individual chains within the crystalline domains. Representative chain conformations for all systems are shown in figure 5.7, where panels (a-c) correspond to self-seeded systems and panels (d-g) to continuously cooled systems. In panel (a), the chain from the system crystallised at $T_c = 67°C$, can be seen to be crystallised in two different configurations because it spans both crystalline regions within the simulation box. Notably, there is distinct folding at the bromine groups (highlighted in red), which act as preferred folding sites, with each stem containing four bromine segments. This

tight folding pattern is consistently seen across the self-seeded systems. At higher crystallisation temperatures, similar folding patterns are observed, but the stems are longer, with 5 bromine segments per stem at $T_c = 72°C$ and 6 bromine segments per stem at $T_c = 77°C$. Additionally, some registry between adjacent bromine units is apparent, a feature that is explored in more detail in the previous section.

Counter to this, the chain conformations in the continuously cooled systems (panels d-f) also exhibit a tendency to fold at the bromine units. However, these chains fail to fully crystallise, and the stems remain shorter and less ordered than in the self-seeded systems. The incomplete crystallisation in the continuously cooled systems reflects the disorganised nature of the folding process when rapid cooling is employed, as the chains have less time to properly align and form extended, well-ordered crystalline stems.

5.3.5 Registry of Bromine Layers in Crystalline systems

To assess the degree of registry between bromine units in the crystalline regions of the lamella, the radial distribution function (RDF) of bromine atoms was calculated for self-seeded systems at both the crystallisation temperature and room temperature, as shown in figure 5.8 (a) and (b). The crystallisation or quench temperatures are displayed in the upper right corners of the respective panels. At the crystallisation temperature, all self-seeded systems exhibit a series of repeating maxima, corresponding to successive bromine shells in the crystal, with peaks that extend until the RDF reaches half the box size, as seen in panel (a). While these peaks are pronounced, they are relatively broad, indicating that the bromine units are not perfectly aligned. For reference, the red curve shows the RDF for bromine units in the melt state, where only the first coordination shell appears, and no significant peaks are present beyond that.

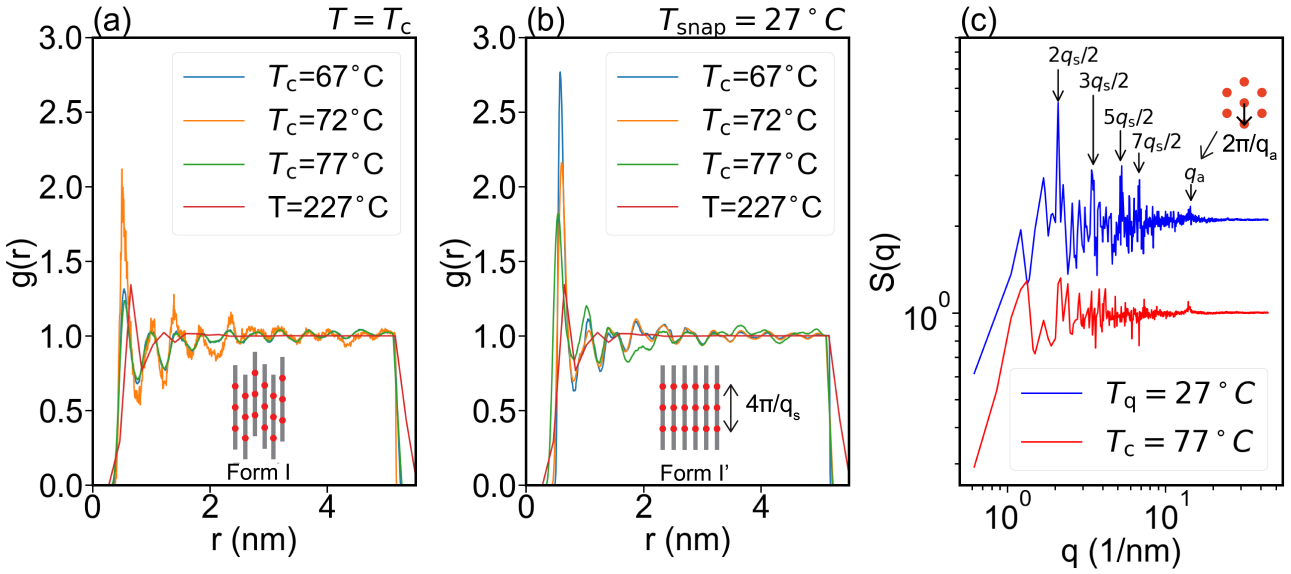

Figure 5.8: The radial distribution function calculated using only united-monomers containing bromine groups at the crystallisation temperature and quench temperature and the structure factor for the bromines in the system crystallised at 77°C, before and after quenching. (a-b) RDF calculated with 1200 bins, with a cutoff distance of 7.5nm, for the self-seeded systems at $T = T_c$ and $T = 27$°C respectively, the RDF of the melt at 227°C is shown in both panels for comparison. In panel (c) the partial structure factor is calculated using only the united-monomers containing bromine groups at the crystallisation temperature (red curve) and room temperature (blue curve). From [1]

In contrast, the RDF at room temperature, displayed in panel (b), reveals sharper and more defined peaks, suggesting stronger registry and long-range order between the bromine units. This is further supported by the partial structure factor shown in panel (c) for the system crystallised at $T_c = 77$°C. At the crystallisation temperature (red curve), the hexagonal rotator phase is evident with peaks corresponding to q_a, but no sharp Bragg peaks at low q-values. Upon quenching to room temperature (blue curve), very distinct peaks emerge, aligning with the layer spacing between bromine layers in the crystalline lamellae. These peaks occur at multiples of the fundamental layer spacing, indicating the formation of ordered bromine layers, tilted relative to the stem direction, as visualized in figure 5.4 (a-c). This behaviour resembles the Smectic-C phase seen in liquid crystals.

In the Smectic-C phase, molecules exhibit liquid crystalline positional order, with some translational entropy allowing for movement between layers. A similar phenomenon is observed here, where the bromine units in Form I can shift around an average position to minimise the energy penalty of neighbouring bromine atoms. However, upon cooling to room temperature, the bromine units become more tightly registered, forming distinct layers as observed in Form I' [2]. Due to thermal fluctuations, it is difficult to capture the full layer ordering in a single

snapshot, but the thermally averaged structure factor for bromine units reveals the quantised layers more clearly. A smaller peak at $q_a \approx 15nm^{-1}$ corresponds to the hexagonal lattice parameter of neighbouring bromine atoms within each registered layer. The tilt of the bromine layers with respect to the stem direction may be a result of finite-size effects in the simulation, a phenomenon also observed in previous simulations of linear polyethylene. The exact cause of this tilting remains the subject of ongoing investigation.

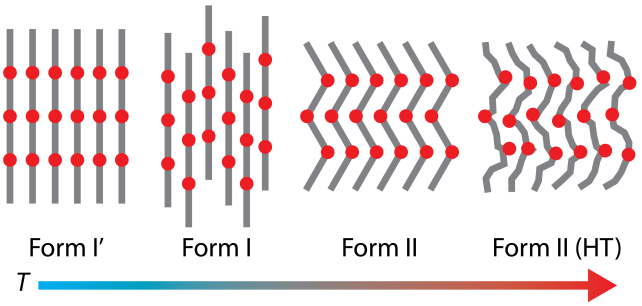

Figure 5.9: Cartoon polymorphs exhibited by precision PE chains with dibromo defects placed regularly on every 21st carbon atom. From [1]

Quantised lamellar thickening, while well-documented experimentally over the years [30, 31], it is rarely observed in simulations. This behaviour is understood within the framework of the Hoffman-Lauritzen theory, which explains lamellar thinning with increased undercooling [32]. However, quantised thickening has been observed only in a few macromolecular systems, such as ultra-long n-alkanes and some polyethylene derivatives with regularly spaced defects such as PEB [33]. Recent simulations of polyethylene chains have demonstrated stepwise thickening via folding [34, 35] or short chain branching [21, 20], but this study is the first to demonstrate quantised thickening driven by preferential fold sites along the chain.

A series of experimental studies by Tasaki et al [2] have revealed that PEBr crystallises into four distinct forms, namely Form I′, Form I, Form II and the high temperature phase (HT) see figure 5.9. Form I is obtained by rapidly quenching melt at room temperature. The polymer chains align in an all-trans conformation similar to the classical structure of PE, then they pack in a triclinic unit cell. On quenching Form I readily transforms to Form I′, which has a similar chain conformation, except that the the bromines group together into registered layers with pronounced positional order in the latter. In both forms the bromines are embedded into the bulk of the polymer as hydrogen in PE would. The positional order that comes into effect as the self-seed systems are quenched (figures 5.6 and 5.8) imply that the model is able to simulate results comparable with real life experiments [2]. This is likely due to the repulsion between neighbouring dibromo units that disrupt the layering at higher temperatures. Upon heating both Form I and I′ in the narrow temperature region of 65 - 66 °C, they transform irreversibly to form II through a melt-recrystallisation process. Because of how quick the melt and recrystallisation takes place, the resulting structures also packs in a triclinic lattice.

However, in Form II the chain structure consists of long all-trans methylene arrangements between carbons with the bromine, and then back and forth bends at the carbons with the bromine (gauche type links, see figure 5.9). The bromines also have positional order as in Form I′. Form II can also be obtained from melt by slow cooling. Further heating of Form II beyond the narrow temperature region sees a continuous phase transition to HT phase, where the chains now pack in a hexagonal phase. While the chains maintain their non-planar herringbone structure, the trans methylene groups between the bromine carbons become distorted and shorter.

Though the study has shown clear it that it is possible to have quantised lamellar thicknesses in the crystals of these PEBr polymers, no evidence of self-poisoning was observed. It is possible that the size of the simulation box may have played a part in this as well.

5.4 Conclusion

By employing a united-monomer model of polyethylene (PE) and incorporating two bromine atoms every 11th or 10th bead, it became possible to explore semi-crystalline structures at length scales typical of PE crystals. Additionally, a carefully selected crystallisation method, known as self-seeding, facilitated the growth of precision PE crystals. This approach allowed us to demonstrate quantised lamella thickening in precision PE crystals as crystallisation temperature increased, driven by the systematic placement of bromine halogens along the PE backbone. Notably, this behaviour was largely obscured when using the traditional continuous-cooling protocol, which is commonly applied in PE simulations. Rather than excluding bromine groups from the crystal, their regular placement along the backbone limited the stem length through controlled folding at each bromine group. Combined with temperature-dependent lamella thickening, this process offers a novel method to control lamella thickness in multiples of the spacing between bromine groups along the PE backbone. While bromine groups were well tolerated within the crystal at the crystallisation temperature, quenching to room temperature revealed their tendency to form registered layers within the crystalline lamella. These findings open up new opportunities to explore how modifications in molecular architecture, such as the regular placement of chemical moieties, halogens, or short chain branches, affect semi-crystalline morphology in detail.

References

[1] Kutlwano Gabana et al. “Molecular Simulations of Quantized Lamellar Thickening in Polyethylenes with Regularly Spaced Brominated Groups”. In: (2024).

[2] Masafumi Tasaki et al. "Polymorphism and phase transitions of precisely halogen-substituted polyethylene. (1) Crystal structures of various crystalline modifications of bromine-substituted polyethylene on every 21st backbone carbon". In: *Macromolecules* 47 (14 2014), pp. 4738–4749.

[3] Xiaoshi Zhang et al. "Effect of Self-Poisoning on Crystallization Kinetics of Dimorphic Precision Polyethylenes with Bromine". In: *Macromolecules* 51 (4 2018), pp. 1386–1397.

[4] Kutlwano Gabana et al. "Quantitative Model of Multiple Crystal Growth Rate Minima in Polymers with Regularly Spaced Substituent Groups". In: *Macromolecules* (2024).

[5] Thomas E Gartner III and Arthi Jayaraman. "Modeling and simulations of polymers: a roadmap". In: *Macromolecules* 52.3 (2019), pp. 755–786.

[6] X. Tang, W. Chen, and L. Liangbin. "The Tough Journey of Polymer Crystallization: Battling with Chain Flexibility and Connectivity". In: *Macromolecules* 52 (2019), pp. 3575–3591.

[7] Aidan P Thompson et al. "LAMMPS – a flexible simulation tool for particle-based materials modeling at the atomic, meso, and continuum scales". In: *Computer Physics Communications* 271 (2022), p. 108171.

[8] J. Ramos, J.F. Vega, and J. Martinez-Salazar. "Predicting experimental results for polyethylene by computer simulations". In: *European Polymer Journal* 99 (2018), pp. 298–331.

[9] Wenlin Zhang and Ronald G Larson. "Direct all-atom molecular dynamics simulations of the effects of short chain branching on polyethylene oligomer crystal nucleation". In: *Macromolecules* 51.13 (2018), pp. 4762–4769.

[10] Vaibhaw Kumar et al. "Effect of short chain branching on the interlamellar structure of semicrystalline polyethylene". In: *Macromolecules* 50.3 (2017), pp. 1206–1214.

[11] N Waheed, MS Lavine, and GC Rutledge. "Molecular simulation of crystal growth in n-eicosane". In: *The Journal of Chemical Physics* 116.5 (2002), pp. 2301–2309.

[12] Peng Yi, C Rebecca Locker, and Gregory C Rutledge. "Molecular dynamics simulation of homogeneous crystal nucleation in polyethylene". In: *Macromolecules* 46.11 (2013), pp. 4723–4733.

[13] Hendrik Meyer and Florian Müller-Plathe. "Formation of chain-folded structures in supercooled polymer melts". In: *The Journal of Chemical Physics* 115.17 (2001), pp. 7807–7810.

[14] Hendrik Meyer and Florian Müller-Plathe. "Formation of chain-folded structures in supercooled polymer melts examined by MD simulations". In: *Macromolecules* 35.4 (2002), pp. 1241–1252.

[15] Dirk Reith, Hendrik Meyer, and Florian Müller-Plathe. "Mapping atomistic to coarse-grained polymer models using automatic simplex optimization to fit structural properties". In: *Macromolecules* 34.7 (2001), pp. 2335–2345.

[16] Chuanfu Luo and Jens-Uwe Sommer. "Disentanglement of linear polymer chains toward unentangled crystals". In: *ACS Macro Letters* 2.1 (2013), pp. 31–34.

[17] Chuanfu Luo and Jens-Uwe Sommer. "Role of thermal history and entanglement related thickness selection in polymer crystallization". In: *ACS Macro Letters* 5.1 (2016), pp. 30–34.

[18] Sara Jabbari-Farouji et al. "Plastic deformation mechanisms of semicrystalline and amorphous polymers". In: *ACS Macro Letters* 4.2 (2015), pp. 147–150.

[19] Sara Jabbari-Farouji. "Static and dynamic scaling behavior of a polymer melt model with triple-well bending potential". In: *Journal of Polymer Science Part B: Polymer Physics* 56.20 (2018), pp. 1376–1392.

[20] William S Fall et al. "Role of Short Chain Branching in Crystalline Model Polyethylenes". In: *Macromolecules* 55 (2022), p. 8438.

[21] William S Fall et al. "Molecular Simulations of Controlled Polymer Crystallization in Polyethylene". In: *ACS Macro Letters* 12 (2023), pp. 808–813.

[22] Xiaoshi Zhang et al. "Effect of self-poisoning on crystallization kinetics of dimorphic precision polyethylenes with bromine". In: *Macromolecules* 51.4 (2018), pp. 1386–1397.

[23] Xiaoshi Zhang et al. "Crystallization of long-spaced precision polyacetals II: Effect of polymorphism on isothermal crystallization kinetics". In: *Macromolecules* 53.18 (2020), pp. 7899–7913.

[24] Stephanie F Marxsen et al. "Crystallization of Long-Spaced Precision Polyacetals III: Polymorphism and Crystallization Kinetics of Even Polyacetals Spaced by 6 to 26 Methylenes". In: *Polymers* 13.10 (2021), p. 1560.

[25] H. Meyer. "Structure Formation and Chain-Folding in Supercooled Polymer Melts. Some Ideas from MD Simulations with a Coarse-Grained Model". In: *Polymer Crystallization: Observations, Concepts and Interpretations*. Ed. by J.-U. Sommer and G. Reiter. Vol. 606. Lecture Notes in Physics. Berlin: Springer, 2003, pp. 177–195.

[26] Thomas Vettorel and Hendrik Meyer. "Coarse graining of short polythylene chains for studying polymer crystallization". In: *Journal of Chemical Theory and Computation* 2.3 (2006), pp. 616–629.

[27] William L. Jorgensen, David S. Maxwell, and Julian Tirado-Rives. "Development and testing of the OPLS all-atom force field on conformational energetics and properties of organic liquids". In: *Journal of the American Chemical Society* 118 (45 1996), pp. 11225–11236.

[28] William L Jorgensen and Patric Schyman. "Treatment of halogen bonding in the OPLS-AA force field: application to potent anti-HIV agents". In: *Journal of chemical theory and computation* 8.10 (2012), pp. 3895–3901.

[29] Steve Plimpton. "Fast parallel algorithms for short-range molecular dynamics". In: *Journal of Computational Physics* 117.1 (1995), pp. 1–19.

[30] James J Weeks. "Melting temperature and change of lamellar thickness with time for bulk polyethylene". In: *Journal of Research of the National Bureau of Standards. Section A, Physics and Chemistry* 67.5 (1963), p. 441.

[31] John D Hoffman and James J Weeks. "X-ray study of isothermal thickening of lamellae in bulk polyethylene at the crystallization temperature". In: *The Journal of chemical physics* 42.12 (1965), pp. 4301–4302.

[32] John D Hoffman, G Thomas Davis, JI Lauritzen, et al. "Treatise on solid state chemistry". In: *Plenum Press, New York* 3 (1976), p. 497.

[33] Stephanie F Marxsen et al. "Crystallization Rate Minima of Poly(ethylene brassylate) at Temperatures Transitioning between Quantized Crystal Thicknesses". In: *Macromolecules* (2022).

[34] Wenbing Hu. "Chain folding in polymer melt crystallization studied by dynamic Monte Carlo simulations". In: *The Journal of Chemical Physics* 115.9 (2001), pp. 4395–4401.

[35] Tuukka Verho et al. "Crystal growth in polyethylene by molecular dynamics: The crystal edge and lamellar thickness". In: *Macromolecules* 51.13 (2018), pp. 4865–4873.

6 Monte Carlo Simulation of Stereocomplex in High-Molecular-Weight Poly(Lactic Acid)

In this Chapter, we explore the claim that the formation of the poly(lactic acid) stereocomplex is stopped by random fluctuations in the melting that lead to areas of high concentration of one enantiomer and low concentration of the other [1]. The study uses a simple Monte Carlo simulation with a diffusion to mimic the Brownian motion of the enantiomers. A paper detailing the results of this work is currently in preparation.

6.1 Introduction

The stereocomplex crystal (SC) of poly(lactic acid) (PLA) is made from a mix of its enantiomers poly(L-lactic acid) (PLLA) and poly(D-lactic acid) (PDLA). In its crystal structure, the SC has helices of PDLA and PLLA paired up in an antiferromagnetic arrangement. When SC is crystallised from a high-molecular-weight ($\geq 4 \times 10^4$ g/mol) racemic mixture at temperatures below 230°C and fast cooling rates, its growth is seen to slow down [2, 3]. A differential scanning calorimetry (DSC) study of low- and high-molecular-weight PLA revealed distinct differences in their crystallisation behaviour [1]. For high-molecular-weight PLA, the DSC results displayed two peaks: one corresponding to the crystallisation of SC crystals and the other to the crystallisation of homochiral (HC) crystals. Notably, these peaks persisted even with the addition of a nucleating agent. In contrast, the DSC results for low-molecular-weight PLA showed a single peak during both cooling and heating cycles, occurring around 200°C. This single peak suggests the formation of SC crystals, as its melting point is higher than that of HC, which melts below 175°C.

This strange behaviour PLA has been likened to the self-poisoning of long chain n-alkanes, low-molecular-weight poly(ethylene oxide) fractions, poly(ethylene bromine) and poly(ethylene brassylate). Self-poisoning in polymers requires that they be able to attach to the crystal in more than one way and that those ways not be energetically equivalent. However as the racemate was polydispersed it ruled out it having quantised lamellar thickness, and with the wide-angle X-ray scattering (WAXS) not showing any change in the crystal structure, poisoning due to different forms was also ruled out. Cui et al [1] have claimed that this behaviour in the high-molecular-weight SC can be explained by a poisoning due to purity. They suggest that growth of SC is hindered by the build up of either PLLA or PDLA that remains unpaired during the formation of SC. There is an excess of one of these at the SC growth front because of fluctuations in the melt. The SC crystallisation is favoured by seeding as there are crystals remaining in the melt and that reduces the fluctuations in the melt. This allows SC crystallisation to resume at lower temperatures.

The explanation proposed by Cui et al [1] is qualitative and not quantitative. In this Chapter

a quantitative model is developed to investigate the poisoning by purity explanation. This is achieved through Monte Carlo simulations, where parameters relating to temperature and diffusion can be quantified.

6.2 The Model

Antiferromagnetic systems have been studied with lattice models for many decades now, with lattices such as the square lattice being preferred as they favour this arrangement. In this study we employ the use of a MC simulation on a 2D 50×50 square lattice as the lattice is big enough to see the effects of diffusion and the simulations run under a couple of hours and use less memory compared to much bigger lattices. Each site on the lattice corresponds to a segment of a chain in the the lamellar structure, that is either a left- or right-handed helix. The site can be amorphous or crystalline. This is because each segment is expected to be either PLLA or PDLA (not mixed), the 2D model is of course much simplified, but it is not so far from the true 3D polymer crystal.

The MC simulation is a widely used Markov Chain Monte Carlo (MCMC) method [4]. Here it is ran using the Metropolis-Hastings algorithm. It generates a sequence of states according to a desired probability distribution. It is explained in greater detail in Chapter 2 of this thesis. The lattice has periodic boundary conditions to simplify the calculations by not concerning itself with surfaces. MC simulations are ran for 100 million steps, ensuring that on average each site has a chance of being visited over 40 thousand times. The crystallisation is started with a nucleus less than or equal to 2% of the total lattice to promote crystallisation and reduce computation time.

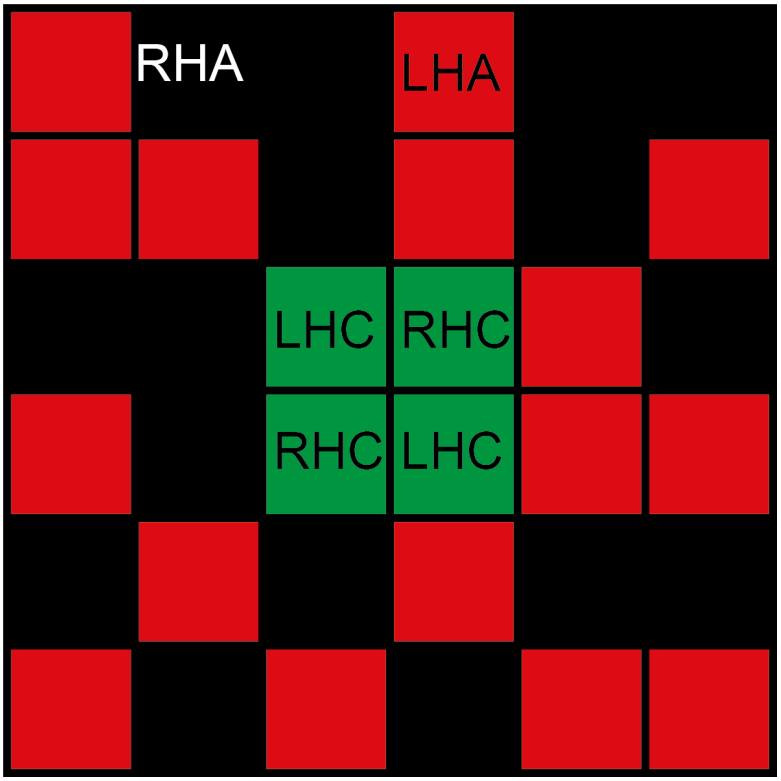

Figure 6.1: Crystallisation of PLA Stereocomplex on a square lattice. The left-handed and right-handed crystalline (LHC and RHC) are shown as by green tiles on the lattice. While, the left-handed and right-handed amorphous (LHA and RHA) sites are shown in black and red respectively on the lattice.

In the simulation, the left- and right-handed crystalline sites are referred to as LHC and RHC for short. The left- and right-handed amorphous sites are abbreviated as LHA and RHA. RHA and LHA are shown in black and red respectively on the lattice, while both LHC and RHC are shown in green, as shown in figure 6.1. When a site is chosen randomly during the MC simulation, one of its four nearest neighbours is chosen at random and inspected. If the site is amorphous it can crystallise if then chosen neighbour is a crystalline site, or swap positions with another amorphous site of the opposite hand. Crystalline site on the other hand can only melt if the chosen neighbour is amorphous. All these actions are dependent on the parameters p, q and d.

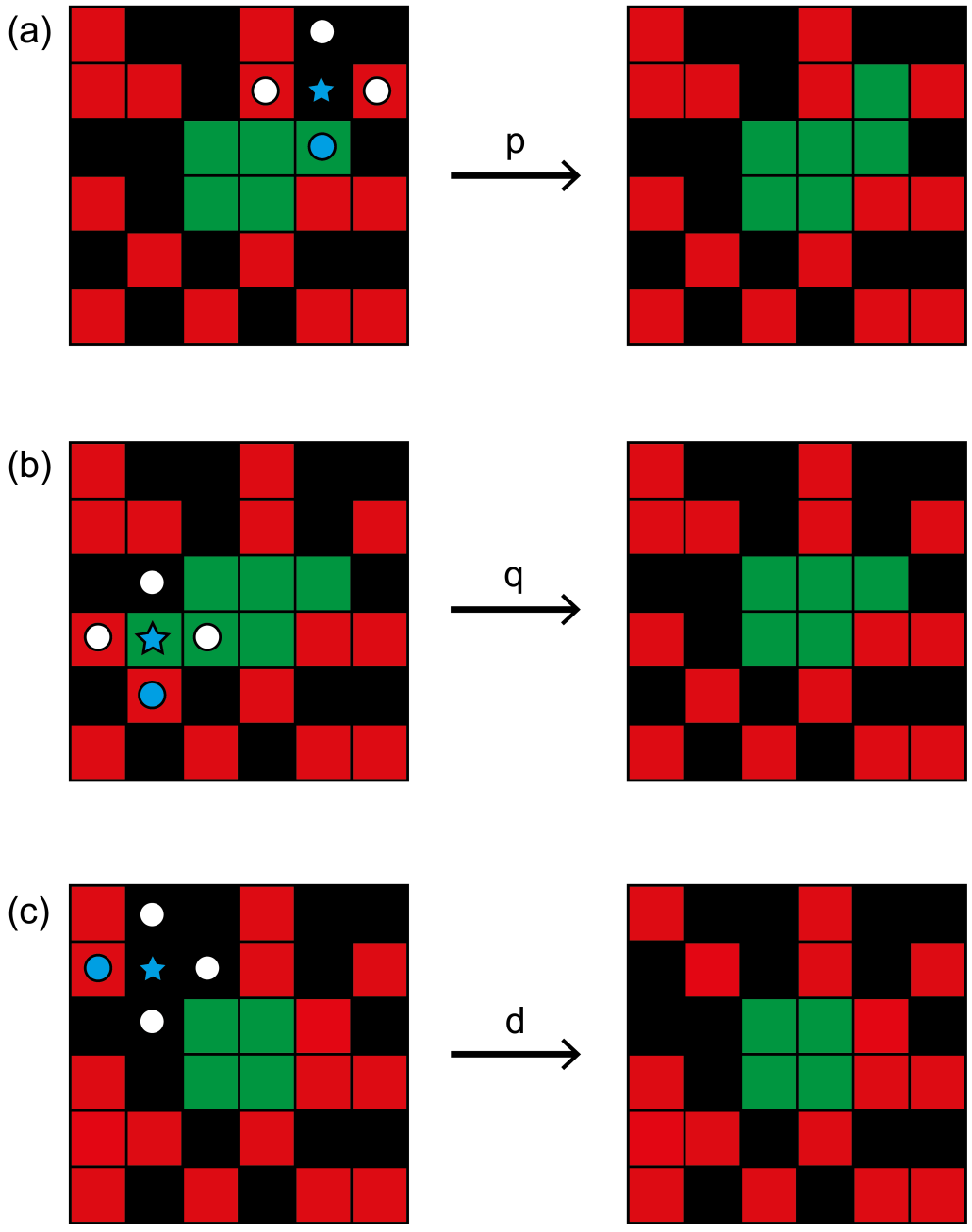

Figure 6.2: The MC simulation parameters for the PLA stereocomplex. A site is chosen at random (shown by the blue star) and one of its four neighbours is examined (shown by the blue circle). If the chosen site is (a) amorphous and the chosen neighbour is a crystalline site of the opposite handedness it can crystallise with probability p. If the chosen site is (b) crystalline and the chosen neighbour amorphous then it can melt with probability q. And if the cite chosen is (c) amorphous and the corresponding neighbour is also amorphous and of a different handedness, they two can swap positions with probability d.

An amorphous site can crystallise with probability p if it is next to a crystalline site of the opposite handedness (figure 6.2(a)). A crystalline site can melt with probability q if it next to an amorphous site (figure 6.2(b)), and two amorphous sites of different handedness can swap with probability d, simulating diffusion (figure 6.2(c)). The simulations are carried out at the same temperature; thus p, d and q are constant. Moreover, increasing (or decreasing) q and d, while simultaneously decreasing (or increasing) p is the equivalent of increasing (or decreasing) the temperature, respectively. p is set to be equal to 1 so that all sampled amorphous sites next to a crystalline site crystallise, and then d and q are to be found relative to this value of p.

We keep track of two metrics to measure the growth of the SC and to see if the rest of the polymer will separate into HC clusters. The first metric is the crystallinity of the polymer, which is measured by counting the crystalline sites as a fraction of the lattice. Because clusters of pure left- or right-handed PLA are seen experimentally, we also keep track of the clusters in the system. Amorphous lattice sites are considered to be in a cluster if they have at least one amorphous neighbour of the same handedness. The counting is done using the deep-search algorithm described in Chapter 2.

6.3 Results and Discussion

6.3.1 Parameters q and d

The parameter d controls the rate at which crystallisation proceeds. Higher d values allow the crystallisation to happen faster than with lower d values. This can be seen from figure 6.3 for constant q and different d values, where the crystallinity reaches maximum value quicker with a higher d. There is no full crystallisation without q, as some of the amorphous sites are trapped in environments where they can neither diffuse nor crystallise. Small fluctuations in the lattice of melting and re-crystallisations can help the trapped amorphous helices. For the same value of d, increasing q seems to allow melting at the growth front which in turn allows the melt to reorganise into pairs of opposite-handed helices and allows higher crystallinity. Without d the crystal grows as a fractal along the sites that are already ordered along the growth front, d can bring the right site to the growth front allowing for the crystal to spread throughout the lattice.

The combinations of q and d that favour or suppresses SC crystallisation are dependent on how the starting lattice was populated. In this study the starting lattice is either populated randomly or with local clustering.

6.3.2 Random Starting Lattice

For the random starting lattice, the middle four squares are the SC crystal seed. Then around it equal numbers of left- and right-handed sites are randomly placed to fill the space.

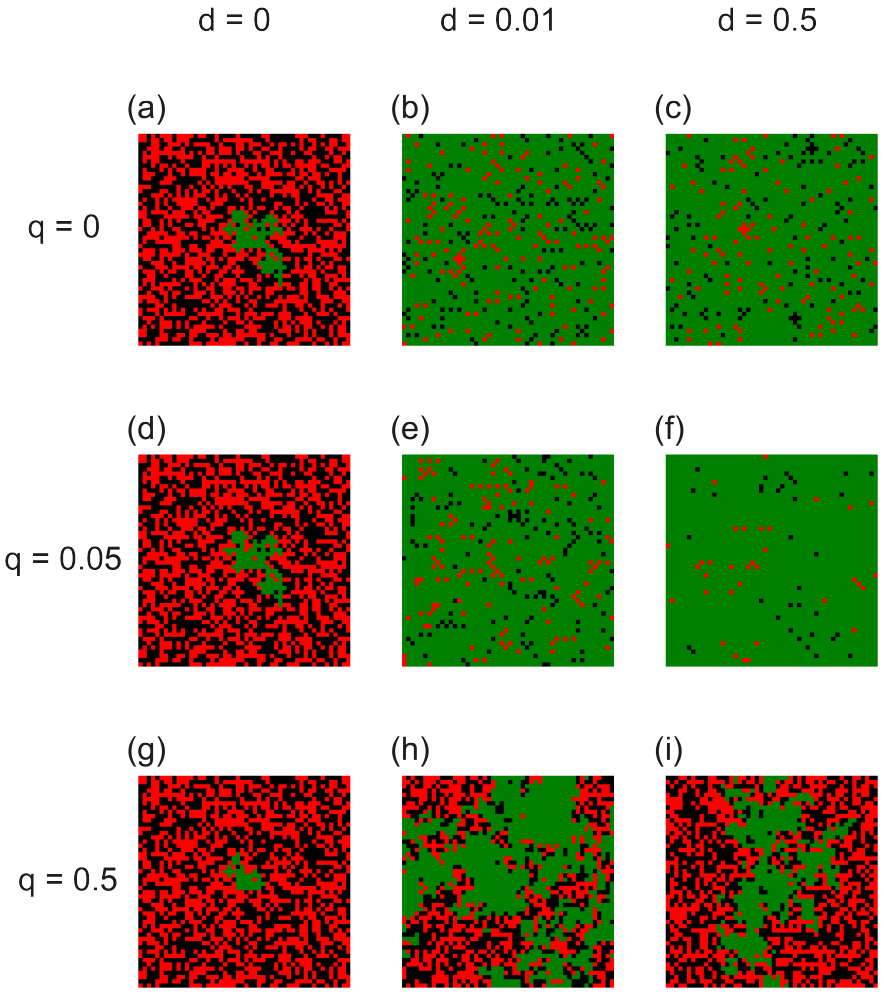

Figure 6.3: The final lattice arrangements during the crystallisation of PLA stereocomplex with varying melt and diffusion probabilities, starting from a random lattice. The LHA is shown in red, the RHA in black and the crystal in green. with crystalline regions in green, amorphous regions in red, and impurities in black. d is constant along a row, and q is constant across the column. The crystallinity is represented as Cr. When both q and d are zero ((a), (d) and (g)) the crystal grows into a fractal along the paths where the melt is already arranged in the correct way as there is no diffusion. Increasing the d greatly increases the crystallinity for low values of q ((b), (e) and (h)). When $q > 0.45$ the crystallinity drops across all d values, peaking at 0.452 for $d = 0.01$ and decreasing to 0.211 at $d = 0.5$.

When both q and d are zero, only a small fraction of amorphous sites crystallise. Only the sites that are already arranged in the correct complementary state can crystallise into the SC, resulting in a fractal growth. When d is non-zero, majority of the lattice crystallises as the sites in the melt are able to swap and bring the correct sites to the growth front. Higher d values allow the crystallisation to happen faster than with lower d values. There is no full crystallisation without q, as some of the melt is trapped in environments where they can neither diffuse nor crystallise.

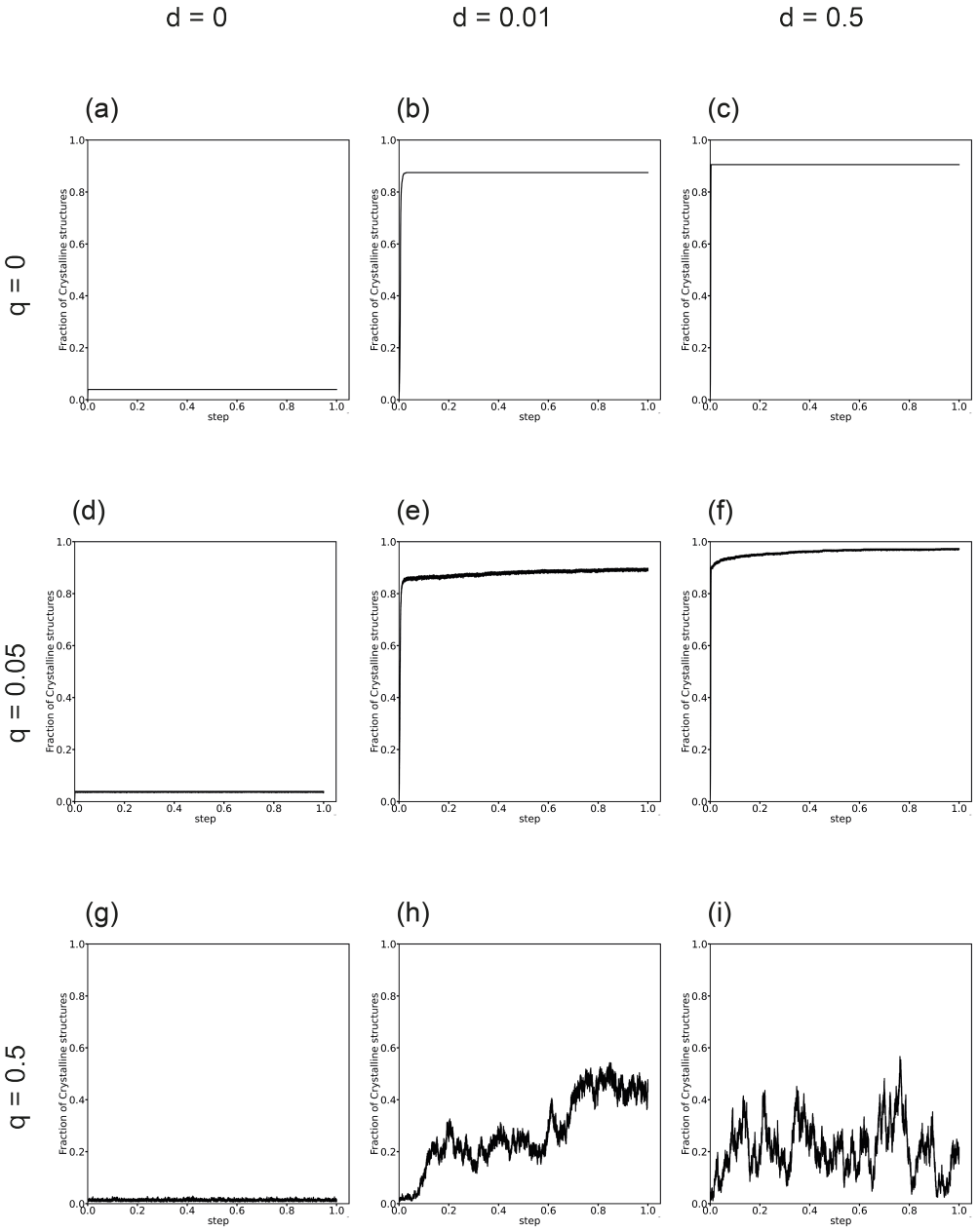

Figure 6.4: The change in the crystallinity with the simulation steps for different combinations of q and d. q is constant along a row, and d is constant across the column.

When q is larger than 0.45, the melt is more stable than the SC crystal, and with larger d values fluctuation in crystallinity in the lattice can be seen due to frequent crystallisation-melting processes. This is better seen in figure 6.4(h)-(i), where the graphs displays erratic behaviour, with frequent, irregular changes in the crystallinity.

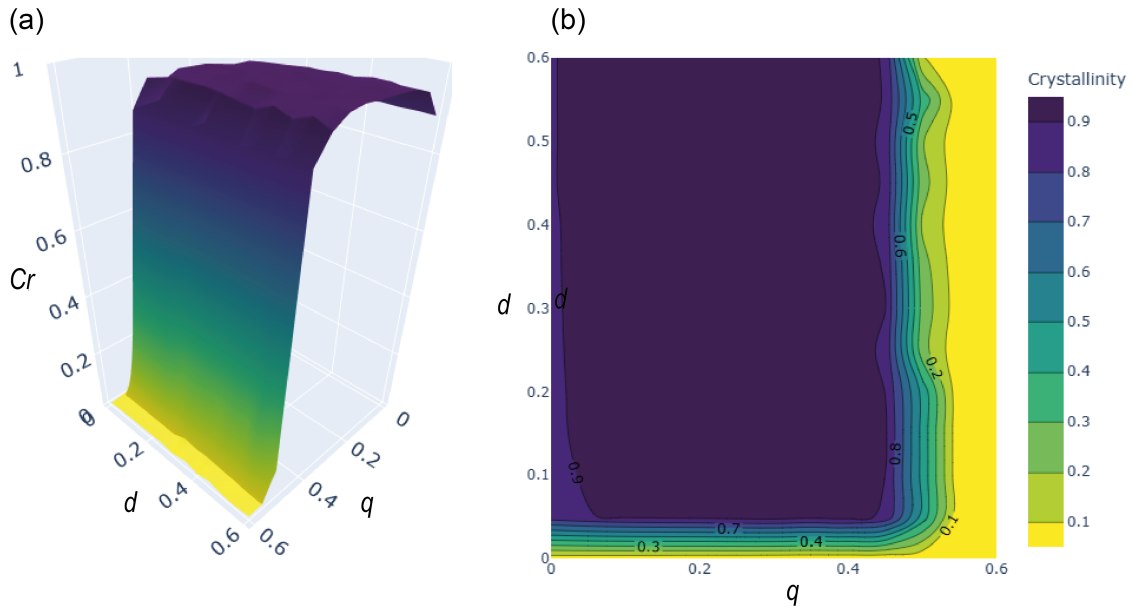

Figure 6.5: The crystallinity landscape for different q and d values. The crystallinity is shown as cr, and both (a) and (b) are coloured according to the value of the crystallinity for each combination of q and d. (a) Is the 3D surface representing the crystallinity. (b) is a 2D contour showing points with the same crystallinity as the same colour and joined by the contour lines.

The HC cluster at the end of the simulation is largest for q greater than 0.45. However, the clusters are not purely PLLA or PDLA but a mixture of both. The largest cluster reduces to below twenty sites in the cluster for $0 < q < 0.45$, where the crystallinity is highest.

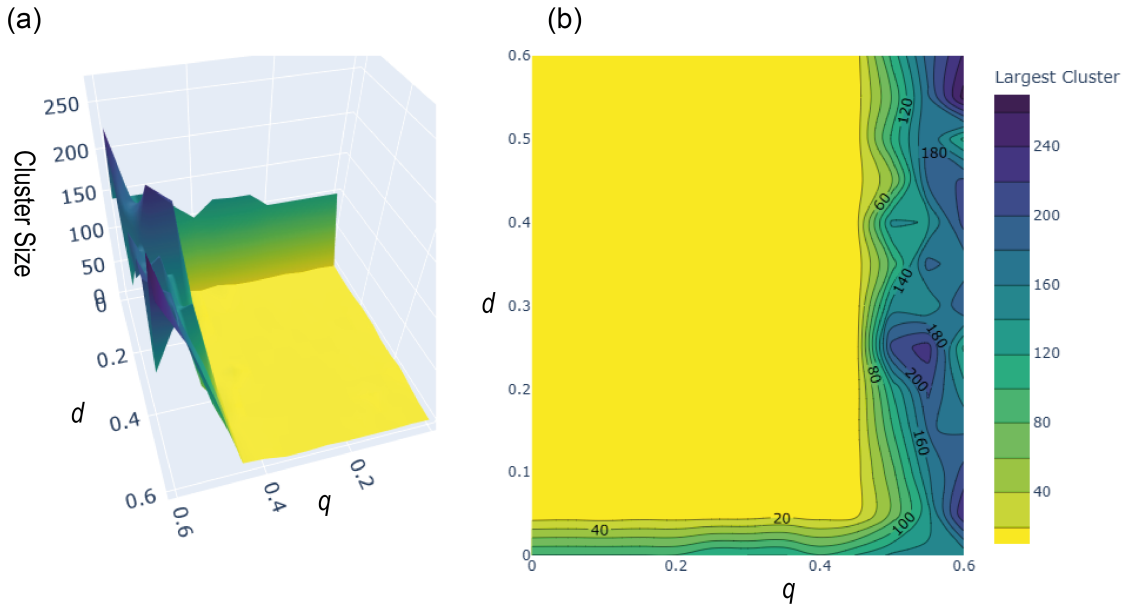

Figure 6.6: The largest homochiral cluster size landscape for different q and d values. The largest cluster size is shown (a) as a 3D surface and a (b) is a 2D contour. (a) and (b) are coloured according to the value of the size of the largest HC cluster for each combination of q and d.

6.3.3 Clustered Starting Lattice

A study by He et al [5] found that the likelihood of helices of the HMW chains encountering neighbours belonging to the same chain was increased. This means that there is more likely to have small-scale segregation in the neighbourhoods of either PLLA or PDLA. This is implemented by using MC simulations with Glauber dynamics to allow the random to segregate before crystallising. In this case amorphous sites of the different handedness may swap with probability D, either if the swapping increases the number of like-handed neighbours for both of them, or if it increases same handed neighbours for one and the other is maintained. Otherwise, they may still swap with probability d, where $d << D$. D is set as 1 and d is defined with respect to it. The segregation is allowed to take place for 5 million, 10 million and 20 million steps. Beyond this, the lattice separates into two unmixed HC domains.

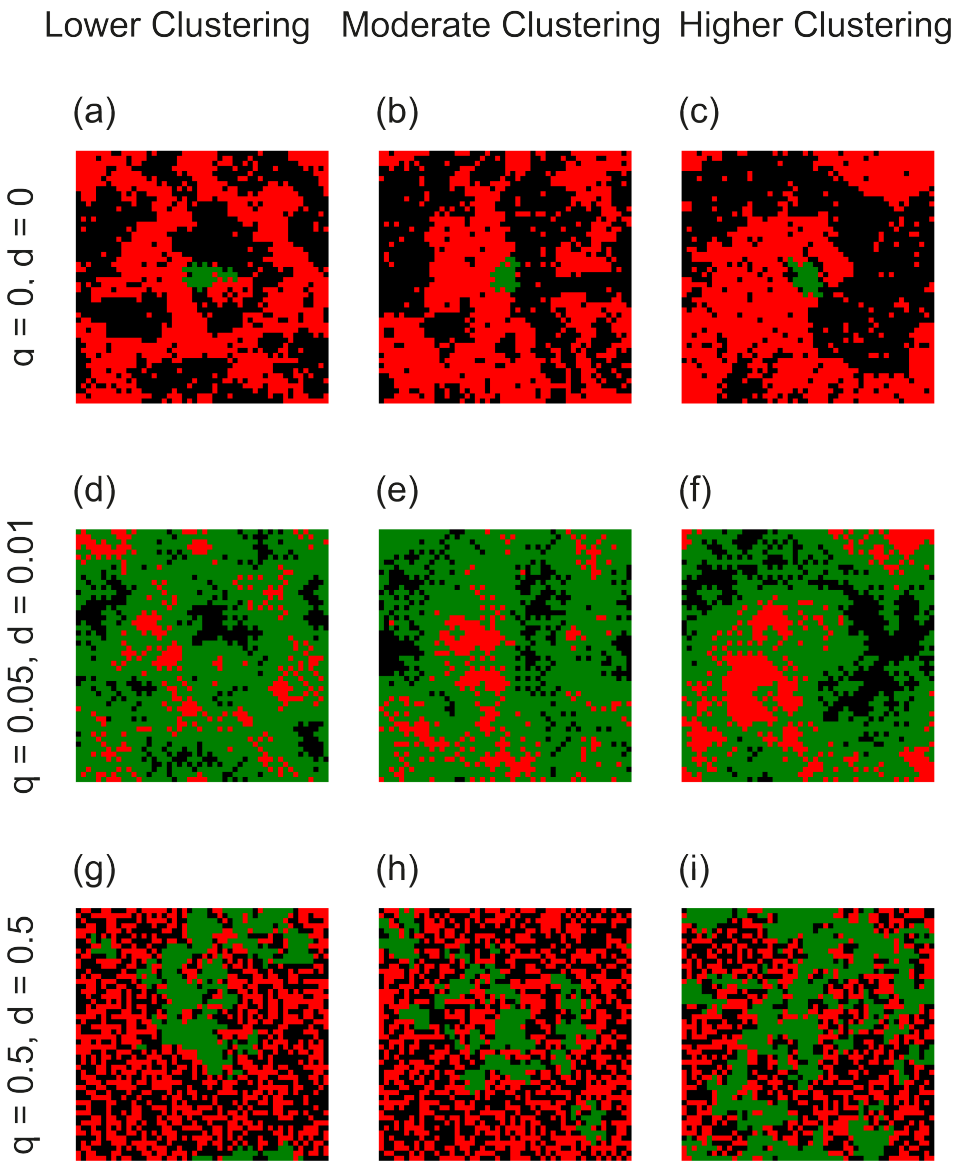

Figure 6.7: The final lattice arrangements for different values of q and d, with crystallisation carried out at different segregations. The values of q and d that the crystallisation were carried out at are the same across a row, and the results presented along each row had the same starting lattice. When q and d are both zero ((a)-(c)) a fractal growth is seen as before but with a lower crystallinity. The crystallinity is also lower than that in a random lattice at lower values of q and d ((d)-(f)). Moreover, the crystallinity is just over 0.5 with the highly segregated starting lattice with HC clusters as would be expected from the experimental results. Ad again similar to the random starting lattice, the crystallinity drops beyond $q = 0.45$.

The way the crystallinity varies with q and d is similar to that done from a random lattice. However, the clustering influences the value of he crystallinity and the sizes of the HC clusters. This becomes more apparent when the starting lattice is highly segregated and for low q and d values, i.e., low T values. As the value of q decreases, there is less melting of the crystal and lower fluctuations in the lattice, this allows the crystal to grow fast toward the equilibrium crystallinity. However, the reduced fluctuations also mean that the growth front is less likely to melt and this makes it more difficult for reorganising the lattice for better crystallisation. This results in crystal with pure HC clusters remaining. The sizes of the clusters are greater than those from a random lattice as shown in figure 6.8.

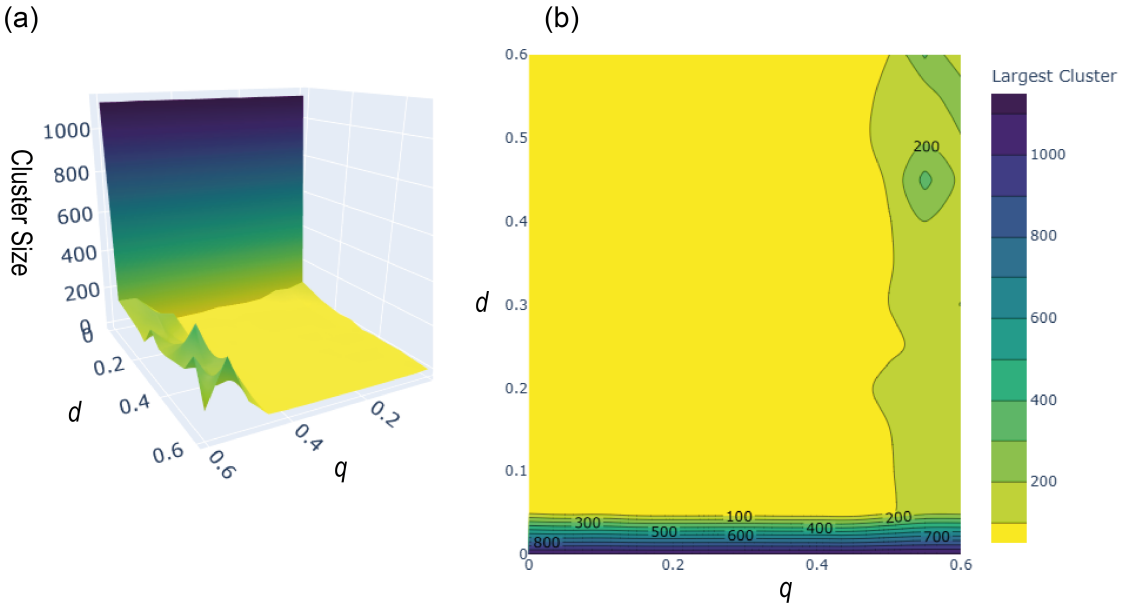

Figure 6.8: The largest homochiral cluster size landscape for different q and d values from the highly segregated starting lattice. The largest cluster size is shown (a) as a 3D surface and a (b) is a 2D contour. (a) and (b) are coloured according to the value of the size of the largest HC cluster for each combination of q and d. The clustering is highest at the $q, d = 0$ because of the initial segregation.

This result is similar to what is observed with high-molecular-weight PLA at low temperatures. At high temperatures the diffusion is high allowing for both good mixing between the PLLA and PDLA. And because the crystal is less stable, it can melt to allow reorganising and mixing of the remaining amorphous material. At lower temperatures the crystal is more stable, and the growth is faster than the diffusion. Because of the stability of the crystalline structure, it does not melt easily therefore does not allow good mixing that results in higher crystallinity. In the low-molecular-weight PLA the initial segregation must be lower therefore mixing is still relatively high.

6.4 Conclusion

The crystallisation of PLA stereocomplex was explored using Monte Carlo simulations on a square lattice, where each lattice site represents a helical segment of a chain in the lamellar. The simulation is controlled by the parameters p, q and d, which correspond to the probabilities of crystallisation, melting and diffusion, respectively. The simulation was done with p being constant and different sets of values of q and d. Diffusion facilitates the rearrangement of sites, enabling proper pairing of right- and left-handed helices at the crystallisation front, thereby controlling the speed of the crystallisation. Smaller values of q allow melt-recrystallisation to take place and promote higher crystallinity. At higher values of q the melt is more stable and most the crystal melts.

The simulations demonstrated that intermediate values of q ($0 < q < 0.45$) yielded the most effective SC crystallisation. Increasing the diffusion at each value of q increase the overall crystallinity, or at least the rate at which the overall crystallinity is reached. When the simulations are done from a random lattice the clusters trapped inside the melt are very small compared to the sizes of the clusters when the simulation is done from a lattice with local clustering.

The study shows that when the stereocomplex growth is possible at low temperature (low q values). Diffusion improves the crystallinity at these q values. The results have also showed that the stereocomplex growth is suppressed at high temperatures as seen experimentally.

References

[1] Jiaming Cui et al. “Poisoning by Purity: What Stops Stereocomplex Crystallization in Polylactide Racemate?” In: *Macromolecules* 56 (3 2023), pp. 989–998.

[2] Hideto Tsuji, Suong Hyu Hyon, and Yoshito Ikada. “Stereocomplex Formation between Enantiomeric Poly(lactic acid)s. 3. Calorimetric Studies on Blend Films Cast from Dilute Solution”. In: *Macromolecules* 24 (20 1991), pp. 5651–5656.

[3] Hideto Tsuji and Yoshito Ikada. “Stereocomplex Formation between Enantiomeric Poly(lactic acid)s. 9. Stereocomplexation from the Melt”. In: *Macromolecules* 26 (25 1993), pp. 6918–6926.

[4] Nicholas Metropolis et al. “Equation of State Calculations by Fast Computing Machines”. In: *The Journal of Chemical Physics* 21 (6 1953), pp. 1087–1092.

[5] Yucheng He et al. “Tammann analysis of the molecular weight selection of polymorphic crystal nucleation in symmetric racemic poly(lactic acid) blends”. In: *Macromolecules* 55 (9 2022), pp. 3661–3670.

7 Fddd - A Liquid Crystal of Rotating Quadrupoles

This Chapter presents a simple quantitative theory used to investigate the arrangement of the chiral columns in the columnar LC phases of the straight molecules reported by Li et al [1] and introduced in Chapter 1. The model is then used to evaluate four different arrangements of the chiral columns, of which one is the experimentally observed Fddd structure which has the lowest energy among the ones investigated. The work done here was included as part of the publication [1].

7.1 Introduction

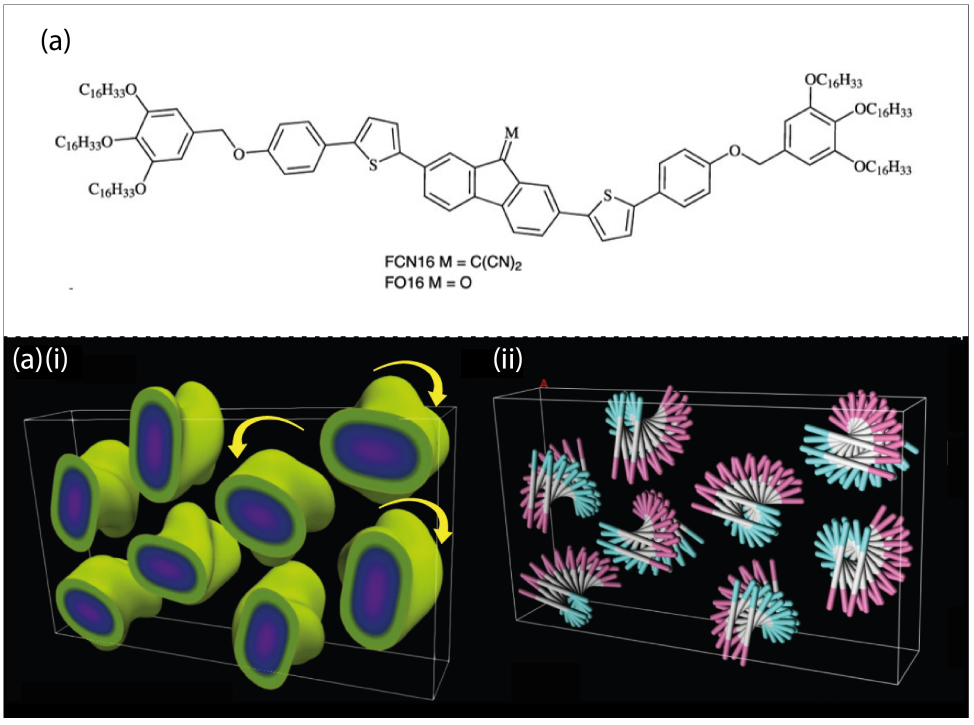

Figure 7.1: Liquid crystal phases in FCN16 and FO16 Compounds. (a) The molecular structure of FCN16 and FO16. (b)(i) The electron density map of the FCN16 showing the helical columns and used to create the stylised models of the Fddd. Taken from [1].

The straight compounds consist of a basic unit of a dimer, which forms the helical column structure. Each dimer is made up of the FO16 or FCN16 molecules illustrated in figure 7.1(a), featuring a core composed of aromatic rings with six attached aliphatic chains. The presence of the aromatic rings in the core not only contributes to its rigidity of the cores of the dimers but also encourages the molecules to align parallel to each other within the columns to maximise

the $\pi - \pi$ bonds. However, this arrangement is not favourable for the end chains which want to avoid clashes and as a compromise the dimers twist and form helices. In the study by Li et al [1] the helical columns are arranged with a complex Fddd symmetry. The unit cell has eight columns; four left-handed and four right-handed columns, with an overall achiral structure. Each column has four neighbours of a different handedness and two neighbours of the same handedness as shown in figure 7.1(b)(i) and (ii).

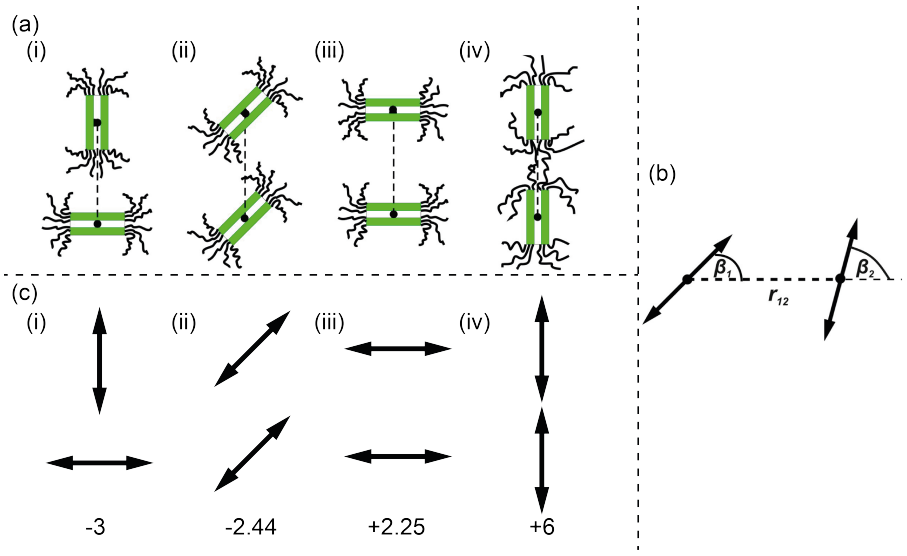

Figure 7.2: Schematic representation of the interactions between pairs of the straight dimers and of pairs of quadrupoles. (a) The interactions of two dimers of straight molecules in neighbouring columns with the minimum energy (i), moderate energy (ii-iii), and highest energy (iv). The minimum energy energy state (a)(i) uses the energy effectively while avoiding clashes, while the moderate energy interactions (a)(ii-iii) leave voids even though they avoid clashes effectively well. In (a)iv the clashes between the aliphatic chains is the highest and the energy is not used as efficiently as in (a)(i). These interactions are similar to those between two linear quadrupoles with the same orientations (c)(i-iv). (b) The interaction energy between two linear quadrupoles a distance r_{12} apart, a quadrupole moment ϕ, and with their orientation defined by angles β_1 and β_2 can be calculated from equation 7.1.

In this work we investigate the arrangement of these chiral columns, specifically whether there are any other configurations that are as energetically favourable for packing these columns as the Fddd. In order to be able to compare the Fddd configuration with others, we develop a model that can quantify the interaction of these columns. We start with the interaction of two such dimers in adjacent columns, where they try to pack by minimising the space they are in while also avoiding clashing between the aliphatic chains. The clashing between the chains is the least when the two dimers are oriented perpendicular to each other and this is provides the best packing between the two just like in figure 7.2(a)(i). While the clashing between the chains is also not bad when the two dimers are parallel to each other as in figure 7.2(a)(ii) and

(iii), the space is not used efficiently and therefore the arrangement is not as good as in figure 7.2(a)(i). The clashing is the highest when the two dimers are aligned end to end like in figure 7.2a(iv), they are also not utilising the space around the as efficiently.

These interactions are reminiscent of those of a linear electric quadrupole, where the highest interaction energy is seen when the quadrupoles are lined end to end as shown in figure 7.2c(i), and is lowest when the quadrupoles are perpendicular to each other. The linear electric quadrupole, hereafter referred to just as a quadrupole, is assumed to have partial positive charge at the ends and a negative charge in the middle that is twice the magnitude. It has low axial symmetry and only one non-zero electric quadrupole moment given by $3qd^2$, where the q is the magnitude of the partial charge at the ends and d is the length of the quadrupole. The interaction energy between two such low symmetry linear quadrupoles is given by the equation,

$$E_{\phi-\phi} = \frac{A\phi^2}{{r_{12}}^5} \tag{7.1}$$

where A given below, is a complicated equation that is in terms of Euler angle β and captures the rotation to principal axes in 2D. ϕ represents the average quadrupole moment of the two interacting quadrupoles and r_{12} is the magnitude of the vector joining their centres [2, 3].

$$A = 3\cos\left(2\beta_1 + 2\beta_2\right) + \frac{9}{16}\cos 2\beta_1 \cos 2\beta_2 + \frac{15}{16}\cos 2\beta_1 + \frac{15}{16}\cos 2\beta_2 + \frac{9}{16} \tag{7.2}$$

The angle β is defined as the angle the quadrupole makes with the line joining the centres of the quadrupoles as shown in figure 7.2b. It is defined as the angle from the line joining the centres to the quadrupole.

7.2 The Rotating Quadrupoles Model

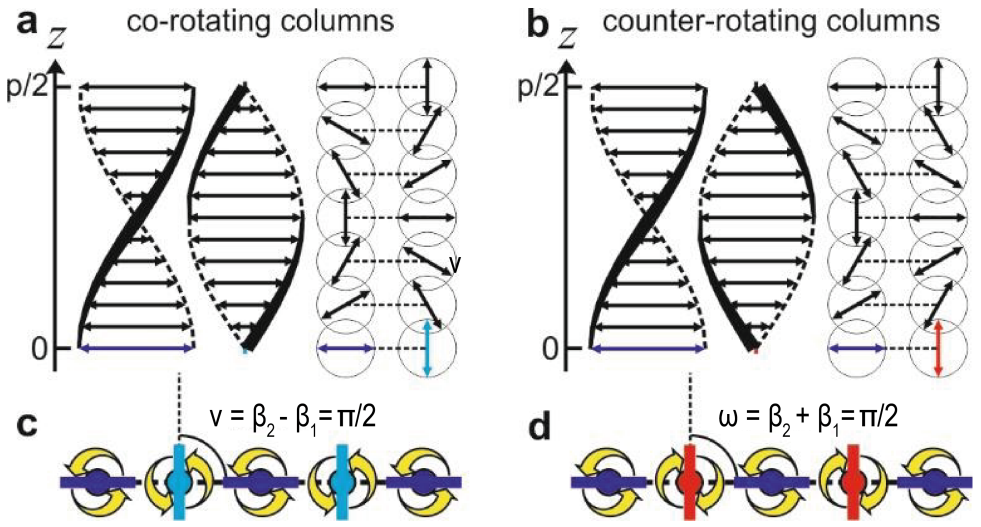

Figure 7.3: Schematic representation of the minimum energy arrangement of neighbouring co-rotating and counter-rotating quadrupole helical columns. Neighbouring co-rotating (a) and counter-rotating (b) helical columns as seen from the side and top. The quadrupoles are rotated by an angle t along the columnar direction (z-axis) to simulate the helicity. c The lowest energy arrangement of quadrupole helical columns in 1D The minimum energy 1D array for co-rotating (c) or counter-rotating (d) neighbours. The handedness of the columns is indicated by the direction of the yellow arrows and the starting angles of the quadrupole at z=0 is shown by the coloured rod at the centre. The interaction between two neighbouring co-rotating and counter-rotating helices is determined by the z-direction independent parameters ν and ω, respectively. For co-rotating helical columns $\nu = \beta_1 - \beta_2$, and for counter-rotating ones $\omega = \beta_1 + \beta_2$. Where β_1 and β_2 are the starting angles of the quadrupoles at z=0 defined according to figure 7.2(b), one from each column, at the same elevation z. Taken from [4]

The similarities between the interaction coupled with the fact that the molecules have no overall electric charge or dipole moment, allow for the dimers to be treated as a quadrupole to quantify the interactions between the columns. Each column is modelled as sequence of quadrupoles that twist along the helical axis as shown in figure 7.3 with the assumption that the helix is continuous. The interaction between the two helical columns is calculated by averaging the interactions of quadrupoles at the same heights along the columns, while disregarding interactions between dimers at different heights. Although this approach is very simple, it effectively captures the essential features of the interaction, as it considers the average orientation of dimers or quadrupoles in one column interacting with those in the other.

For two interacting columns of the same handedness, the difference between the β angles, ν at

each elevation is constant. To calculate the interaction U for two helical columns of the same handedness, co-rotating helical columns, we integrate A with the relevant β angles from 0 to π along the helix. We let $\beta_1 = t$ and $\beta_2 = \nu + t$, with t being a small rotation applied to both starting angles going up the helix. Then the interaction energy U_{co} is given by,

$$U_{co} = \frac{\phi^2}{{r_{12}}^5 \pi} \int_0^{\pi} A(t)\, dt = \frac{\phi^2}{{r_{12}}^5} \left[\frac{9}{32} \cos 2\nu + \frac{9}{16} \right] \tag{7.3}$$

The division by π in the expression for U_{co} normalises the interaction energy to reflect the average value over one turn of the helix. This ensures that the calculation provides an average interaction energy per unit twist along the helix, ensuring the result represents the mean interaction between quadrupoles at various angles, rather than a cumulative total.

For two interacting columns of the differing chirality, counter-rotating helical columns, the sum of the β angles describing the orientation of the quadrupoles, ω, is constant. Let $\beta_1 = t$ and $\beta_2 = \omega - t$, then the average interaction energy between two columns is given by:

$$U_{cou} = \frac{\phi^2}{{r_{12}}^5 \pi} \int_0^{\pi} A(t)\, dt = \frac{\phi^2}{{r_{12}}^5} \left[\frac{105}{32} \cos 2\omega + \frac{9}{16} \right] \tag{7.4}$$

The minimum energy occurs when both ν and ω are 90°. This is comparable with the interaction between two quadrupoles, where the energy minimum is when one quadrupole makes an angle of 90° with the line joining the two, and the other is parallel to this line. However, the minimum energy in units of $\frac{\phi^2}{{r_{12}}^5}$ for the co-rotating helices is $\frac{9}{32}$, whilst that of the counter-rotating is $-\frac{87}{32}$. The stark difference in the energy of $\frac{77}{32}$ shows that for co-rotating columns interacting dimers in adjacent columns at the same level spend more time in unfavourable configurations as compared to in interacting counter-rotating columns hence such a higher average energy per dimer.

On a 1D chain, it is then better to have the columns arranged in a counter-rotating format with alternating left- and right-handed columns. This arrangement would ensure that there a less clashing as indicated by the interaction energy between the columns according to equations 7.3 and 7.4 and shown in figure 7.3(c) and (d).

7.3 Rotating Quadrupole Columns on a Hexagonal Lattice

The columns of systems of straight molecules are seen to arranged with a hexagonal symmetry at high temperature. At the same time the Fddd phase is pseudo-hexagonal, that each column has a coordination number of six, with six nearest neighbours. This has led this study to employ a

hexagonal lattice as it is ubiquitous to the study of the packing of these systems. Studying these systems of straight molecules with chiral columns on a triangular lattice reduces the number of parameters as the distance between neighbouring lattice sites r_{12} is constant between all nearest neighbouring lattice sites. As the interaction energy between two quadrupoles falls off as ${r_{12}}^{-5}$, we can ignore next nearest-neighbour interactions and other further away interactions. Then the theory developed above and the equations 7.3 and 7.4 can be readily used to investigate different configurations of these columns on the lattice.

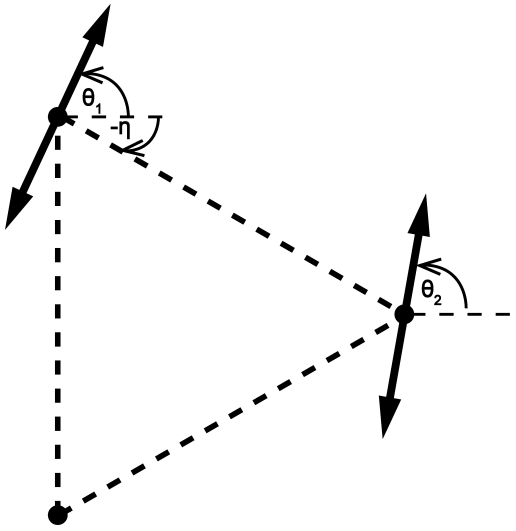

Figure 7.4: Beta angles definition in the triangular lattice. As with the case where the line joining the quadrupoles is parallel with the horizontal axis, the clockwise angles from the horizontal axis is taken as positive. Clearly the angle between the joining line and the quadrupole is the difference between θ and η.

On the triangular lattice however, the line joining the centres is not always parallel to the horizontal axis therefore the angle β is not necessarily the angle the quadrupole makes with the horizontal axis. We define the angle that the quadrupoles make with the horizontal axis as θ, and the angle the line joining the centres of the quadrupoles makes with the horizontal axis as η. Then the positive angle β is from the joining line to the quadrupole in a counter-clockwise direction, mathematically defined as

$$\beta = \theta - \eta \tag{7.5}$$

7.4 Results and Discussion

We applied our model of rotating quadrupoles on a hexagonal to four different configurations with different arrangements of columns, one of which is the Fddd, to calculate the average energy per dimer. This is done by calculating the energy of the unit cell of each configuration by summing up the interactions between the columns using the appropriate interaction energy equation. Between each pair of interacting nearest-neighbour columns, the appropriate parameter (ν or ω) are determined from the relevant β angles at z=0, hereafter referred to as the starting angles, which are in terms of the angles θ. The resulting energy of the unit cell will then be in terms of the starting angles θ.

In order to determine the angles θ responsible for the minimum energy interaction in each candidate configuration the basin-hopping algorithm [5] is used. The basin-hopping algorithm (discussed in detail in Chapter 2: Methodology) is a powerful global optimisation technique that effectively addresses the challenge of finding global minima in functions with multiple local minima. By combining local optimisation, typically using the BFGS (Broyden-Fletcher-Goldfarb-Shanno) method [6, 7, 8, 9, 10], with random perturbations to explore the parameter space, basin-hopping iteratively refines solutions while avoiding local traps. After identifying local minima, the algorithm applies random jumps to probe new regions of the parameter space, utilising a probabilistic acceptance criterion to facilitate exploration. This approach results in a robust method that enhances the likelihood of finding global minima.

The number number of columns per unit cell many vary between configuration, as such a way of comparing their energies is needed. To be able to compare the different configuration, the energy of the unit cell is calculated and divided by the average number interactions for each of column in the unit cell. This then gives the average energy per dimer.

7.4.1 The Fddd configuration

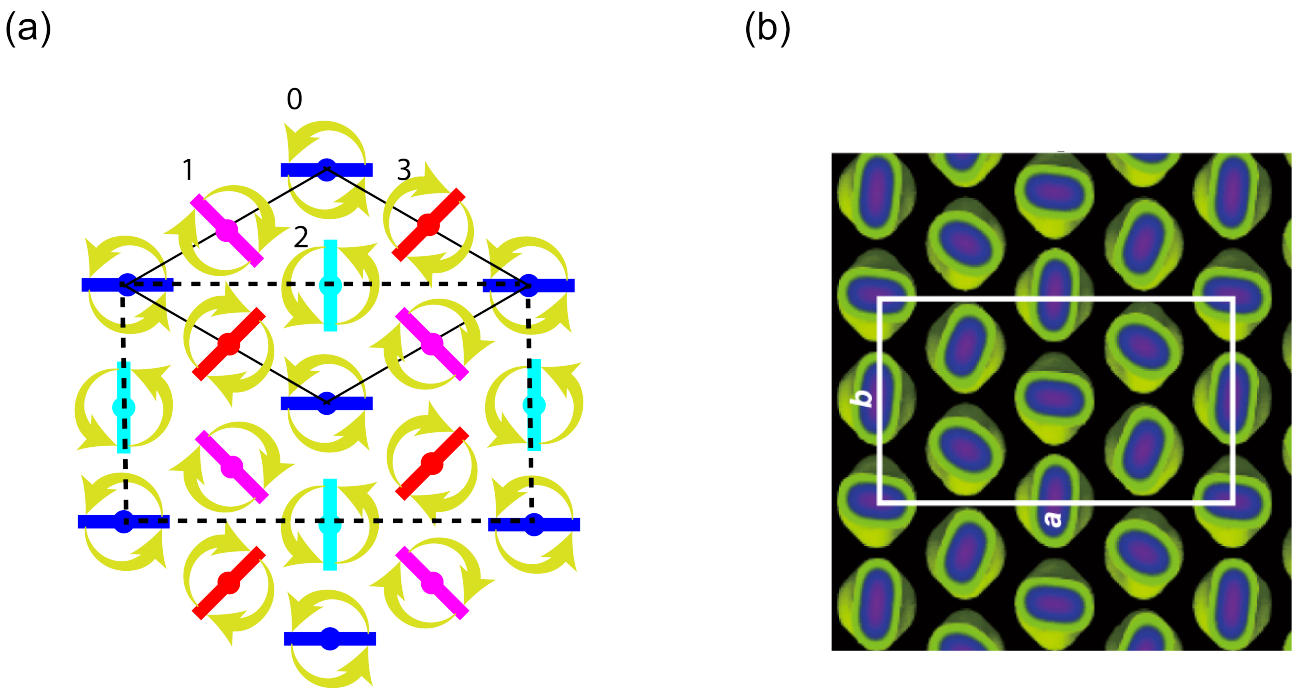

Figure 7.5: The calculated minimum energy configuration on a 2D hexagonal lattice. (a) Lattice configuration with two left- and two right-handed columns in a 2x2 hexagonal unit cell. The result is equivalent to the Fddd structure we have observed experimentally. The different columns are labelled 0 to 3 and colour-coded to distinguish them, with starting angles θ_0 to θ_3 that the coloured sold rods make with the horizontal axis. In the groundstate energy, $\theta_0 = 0°$, $\theta_1 = -45°$, $\theta_2 = 90°$ and $\theta_3 = 45°$ which they are arranged in. The handedness of each column is depicted by the yellow arrows. (b) Real space FCN16. The starting angles of the configuration matches the arrangement of the FCN16. Taken from [1].

It is not possible to have all neighbouring columns be a different handedness on a triangular lattice. The most likely solution would be to maximise the number of counter-rotating columns compared to co-rotating columns by having two of three columns be of the same handedness and the other a different handedness to the two as shown in Figure 7.5. This configuration is equivalent to the Fddd with a 2×2 hexagonal lattice unit cell, with two left- and two right-handed columns. Each column in the system has four neighbours of the opposite handedness and two of the same handedness. For the four different columns in the unit cell labelled 0 through to 3 as shown in figure 7.5, the associated starting angles are θ_0, θ_1, θ_2, and θ_3, respectively. The θ angles are defined with respect to the horizontal axis as described in figure 7.2(b), with corresponding β angles calculated between each pair according to equation 7.5. Without loss of generality, we fix $\theta_0 = 0$, and let rest of the starting angles vary. The energy of the unit cell

is given by,

$$U_{Fddd} = \frac{3\phi^2}{32r^5}\Bigg[70\Big(\cos 2\left(\theta_1 - \frac{\pi}{3}\right) + \cos 2\left(\theta_1 + \theta_2 + \frac{\pi}{3}\right) + \cos 2\left(\theta_3 + \frac{\pi}{3}\right) + \cos 2\left(\theta_3 + \theta_2 - \frac{\pi}{3}\right)\Big) + 6\Big(\cos 2\theta_2 + \cos 2(\theta_3 - \theta_1)\Big) + 72\Bigg] \tag{7.6}$$

The energy groundstate of this configuration per unit dimer in units of $\frac{3\phi^2}{32r^5}$ is -45.6, obtained from dividing the minimum energy of the unit cell by four because of the average number of interactions for each dimer. This happens with starting angles $\theta_1 = -45°$, $\theta_2 = 90°$, and $\theta_3 = 45°$. Here $\nu = 90°$ and $\omega = 90°$ which ensures the lowest possible energy in for both the co-rotating and counter-rotating rows of columns. Though this simple theory seems to show that the Fddd is a solution to this system as seen by the similarity in the arrangement of FCN16, figure 7.5(b), with the starting angles of the quadrupoles as seen in figure 7.5(a). However this does not prove that it is the best and the only solution. It is unsurprising that it is a good way of packing these chiral columns as it maximised counter-rotating interactions.

7.4.2 Alternative Configurations

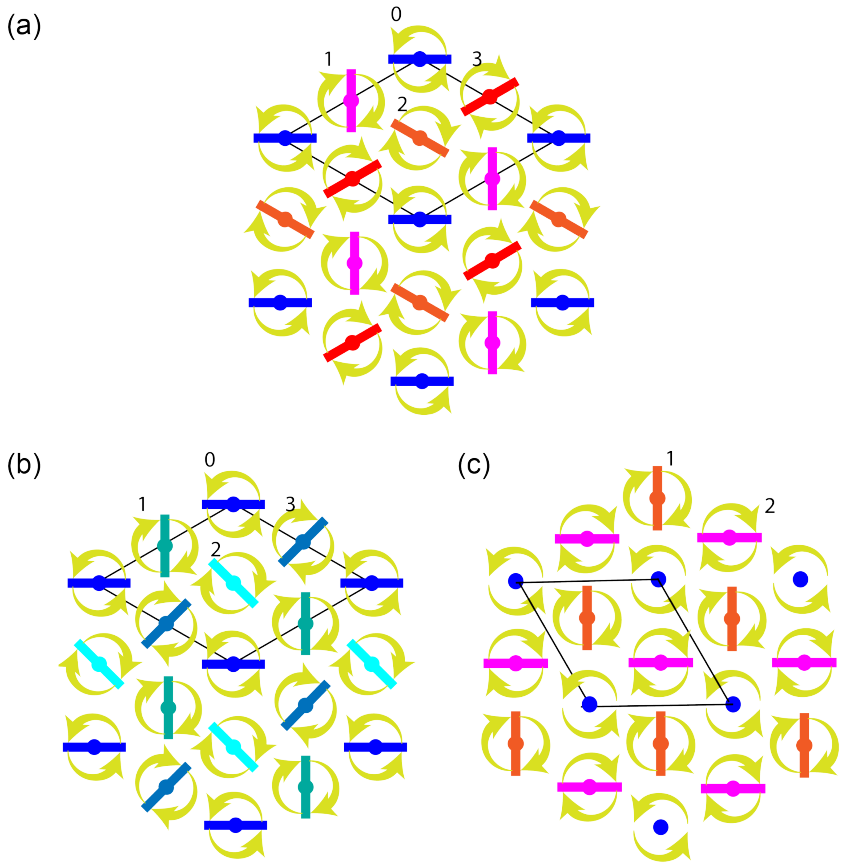

Figure 7.6: Possible candidates for the arrangement of chiral columns in the FCN16 and FO16. (a) The minimum energy arrangement of a 2D hexagonal lattice, with three left- and one right-handed columns in a 2x2 hexagonal unit cell (Configuration one). (b) The minimum energy arrangement on a 2D hexagonal lattice, with four columns of the same handedness in a 2x2 hexagonal unit cell (Configuration two). (c) The calculated minimum energy configuration on a 2D hexagonal lattice, with two left-hand one right-handed columns in a $\sqrt{3} \times \sqrt{3}$ hexagonal unit cell. The orientation of the right-handed (blue) columns can be random without affecting the system energy. (Configuration three)

Three further configurations were explored to see if they could also be a solution. The first alternative configuration shown in figure 7.6(a), is configuration 1, made up of another 2×2 hexagonal lattice unit cell with three columns of one handedness and one of the opposite handedness (assumed to three left- and one right-handed columns in figure 7.6(a) for example) in the unit cell and is overall chiral. The left-handed columns are surrounded by two right-handed column and four left-handed column, while the right-handed column has all six neighbours being left-handed. As seen from figure 7.6(a), the four columns in the unit cell can be labelled

0 through 3 again and with corresponding angles θ_0 to θ_3, respectively. As with the Fddd, assertion that $\theta_0 = 0°$ is made to reduce the number of variables. The energy of the unit cell is,

$$U = \frac{3\phi^2}{32r^5}\Big[70\big(\cos 2(\theta_1 - \frac{\pi}{3}) + \cos 2(\theta_2 - \pi) + \cos 2(\theta_3 + \frac{\pi}{3})\big) \\ +6\big(\cos 2(\theta_2 - \theta_1) + \cos 2(\theta_3 - \theta_2) + \cos 2(\theta_3 - \theta_1)\big) + 72\Big] \tag{7.7}$$

The minimum energy per dimer for this configuration was found to be -36.75 units of $\frac{3\phi^2}{32r^5}$ (found by dividing the energy of the unit cell by four as well), occurring when $\theta_1 = -30°$, $\theta_2 = 90°$, and $\theta_3 = 30°$. The higher energy compared to the Fddd configuration is understandable, as this setup includes two fewer counter-rotating interactions and two additional co-rotating pairs. Furthermore, the angular parameters ν and ω vary between pairs, with average values $\bar{\nu} = 80°$ and $\bar{\omega} = 90°$. Although this configuration is not as good as the Fddd one, the energy is comparable.

The second alternative configuration that was explored is yet another 2×2 hexagonal lattice unit cell picture in figure 7.6(b). The unit cell comprised of four columns all of the same handedness. As with the previous two configurations, the four columns in the unit cell can be labelled from 0 to 3 with corresponding starting angles. The corresponding energy for the unit cell, with the assumption that $\theta_0 = 0°$, is

$$U = \frac{3\phi^2}{32r^5}\Big[6\big(\cos 2(\theta_1) + \cos 2(\theta_2) + \cos 2(\theta_3) + \cos 2(\theta_2 - \theta_1) \\ + \cos 2(\theta_3 - \theta_2) + \cos 2(\theta_3 - \theta_1)\big)72 + \Big]. \tag{7.8}$$

The minimum energy per dimer for this configuration was found to be 15 units of $\frac{3\phi^2}{32r^5}$, occurring when $\theta_1 = 90°$, $\theta_2 = 0°$, and $\theta_3 = 90°$. The average angular parameter ν is 60°, which is less favourable compared to the first configuration ($\bar{\nu} = 90°$) and the Fddd configuration. In this setup, some dimers experience a ν of 90° (favourable for minimising repulsion), while others have $\nu = 0°$, leading to more clashing. These extremes produce a moderate average value of ν, where though the dimers in adjacent columns are not clashing as much, they pack insufficiently in space leaving voids, as seen in Figure 7.2(a)(ii-iii) and (c)(ii-iii).

The last system that was considered consists of two left- and one right-handed columns in a $\sqrt{3} \times \sqrt{3}$ hexagonal unit cell, figure 7.6(c). The left-handed columns have three left- and three right-handed neighbours, while the right-handed column is surrounded by all left-handed

neighbours. This arrangement is similar to that seen in a set of discotic columnar liquid crystals HHTT, mentioned in Chapter 2. For the three columns labelled 0 to 2 with corresponding starting angles θ_0, θ_1, and θ_2, the energy for the unit cell is

$$U = \frac{3\phi^2}{32r^5}\left[9\cos 2(\theta_1 - \theta_2) + 54\right] \tag{7.9}$$

Interestingly, the energy in this configuration is independent of the angle of the right-handed column, depending solely on the angular difference between the two left-handed columns. The global minimum energy occurs when these two columns are out of phase by 90°, while the maximum occurs at 180°. The minimum energy per dimer for this configuration is 15 units of $\frac{3\phi^2}{32r^5}$. Since the minimum energy occurs when $\nu = 90°$ packing within the system tries to minimise the clashes within the co-rotating neighbours. However, this does not make it as good as the Fddd, or even configuration one, where there are at least as many counter-rotating columns as there are co-rotating. Each dimer experiences the same energy as in configuration two with all columns being of the same handedness.

7.5 Conclusion

It is possible to build a simple model to quantify the interaction of the straight molecule chiral LC columns using quadrupoles because of the similarity between the interactions of dimers and quadrupoles figure 7.2, and the similarity in their structure figure 7.1. The dependency of the quadrupole interaction energy on their orientation allows us to be able to simulate the twisting in the helical columns by continually rotating the quadrupoles from $z = 0$ going up the z-axis, until the come back to their starting angle at $z = 0$ figure 7.3. The interaction of energy per dimer is then just the average of the interactions between quadrupoles at different elevations. By integrating the quadrupole-quadrupole energy over pitch of the helical column, the average interaction energy per dimer between columns is seen to only depend on either angular parameter ν or ω, equations 4.14 and 4.15, respectively. The angular parameter ν is the difference between the orientational angles of dimers in co-rotating neighbouring columns at the same z-level, while ω is the sum of the β angles in counter-rotating columns at the same elevation. Both are constant along the columns and are independent of the elevation. The average minimum energy per dimer happens when both ν and ω are 90°, with a value of $\frac{9}{32}$ units of $\frac{\phi^2}{r^2}$ for columns of the same handedness and $-\frac{87}{32}$ for those of different handedness.

Four candidate configurations were investigated using this model on a hexagonal lattice, with the global minimum determined by the basin-hopping algorithm. The first three configurations have a 2×2 unit cell, the first one having more counter-rotating neighbours than co-rotating neighbours (Fddd), the second one with the same number of co-rotating and counter-rotating columns and the last having columns of the same handedness. The last configuration had

a $\sqrt{3} \times \sqrt{3}$ unit cell with one column of one handedness and two columns of the opposite handedness. The Fddd configuration showed the lowest energy per dimer of -45.6 in units of $\frac{3\phi^2}{32r^5}$, while the first, second, and third configurations had energies of -36.75, 15, and 15 all in units of $\frac{3\phi^2}{32r^5}$.

It is unsurprising that these straight-core molecules form chiral helical columns in the columnar phase with an Fddd structure as observed by experiments. On a 1D chain, the helices of these straight-core molecules would rather have neighbours with a different handedness to their neighbours to reduce clashing. On adding a third helix to form an equilateral triangle, the new helix would have to have the same handedness as one of the already existing ones as a compromise. Helices of the same handedness have more clashes as they interact, therefore it would be best to have as many helices of opposite chirality as possible. The Fddd configuration is a better way of packing these molecules in helices in tighter space as it maximises the number of counter-rotating helices that are interacting. Configuration one is nearly as good except for the central helix having its handedness flipped. This means there are more two extra co-rotating pairs and two less counter-rotating ones. Configurations two and three are the most unfavourable. The former only has co-rotating columns where avoiding clashes between interacting dimers is not that easy. Whilst the latter does have a one column of a different handedness to the others, its minimum energy configuration is not an efficient use of packing the columns in space, which in turn makes it as bad as configuration one.

References

[1] Ya xin Li et al. "A case of antiferrochirality in a liquid crystal phase of counter-rotating staircases". In: *Nature Communications* 13 (1 2022).

[2] A D Buckingham. "Molecular quadrupole moments". In: *Quarterly Reviews, Chemical Society* 13 (3 1959), pp. 183–214.

[3] C Hosticka, T K Bose, and Jerzy S Sochanski. "Generalized treatment of the quadrupole-quadrupole interaction of low symmetry molecules and its effect on the second dielectric virial coefficient". In: *The Journal of Chemical Physics* 61 (7 1974), pp. 2575–2579.

[4] Ya xin Li et al. "Supplementary Information A case of antiferrochirality in a liquid crystal phase of counter-rotating staircases". In: *Nature Communications* 13 (1 2022).

[5] David J Wales and Jonathan P K Doye. "Global Optimization by Basin-Hopping and the Lowest Energy Structures of Lennard-Jones Clusters Containing up to 110 Atoms". In: *Journal of Physical Chemistry A* 101 (28 1997), pp. 5111–5116.

[6] C G Broyden. "The Convergence of a Class of Double-rank Minimization Algorithms 1. General Considerations". In: *IMA Journal of Applied Mathematics* 6 (1 1970), pp. 76–90.

[7] R. Fletcher. "A new approach to variable metric algorithms". In: *The Computer Journal* 13.3 (1970), pp. 317–322.

[8] Donald Goldfarb. “A family of variable-metric methods derived by variational means”. In: *Mathematics of Computation* 24 (109 1970), pp. 23–26.

[9] D F Shanno. “Conditioning of quasi-Newton methods for function minimization”. In: *Mathematics of Computation* 24 (111 1970), pp. 647–656.

[10] R Fletcher. *Practical methods of optimization*. Chichester ; New York: Wiley-Interscience, 1987.

8 Conclusion and Future Work

8.1 Conclusion

Poly(ethylene brassylate) shows two minima in its crystallisation rate as it crystallises [1]. A 1D quantitative model was developed to describe the two minima in the crystallisation rate of PEB [1] based of the HU model [2]. The model agrees with the experimental data that the minima are due to self-poisoning like with the long chain n-alkanes [3]. The more stable crystal growing with longer stems are poisoned by the deposition of shorter stems. At high temperatures the crystal of these shorter stems are not stable enough to crystallise. As the temperature is lowered towards their melting point, their stems get deposited faster than they are removed at the growth front of the more stable crystal of the longer stems. This causes a build up and prevents the longer stems attaching. As the temperature is lowered below the melting point of the crystal of the shorter stems, the crystal becomes more stable and grows in place of the crystal of the longer stems. Most of the conversation involving self-poisoning is either purely qualitative or uses simulations. This model though simple was able to reproduce the crystallisation curves of very well, except at the crossing point between the DSC data and FSC data. This allows for direct comparison between mode l and experimental result, which even the HG model did not have. The model can be used to study crystallisation dynamics in other work systems as shown in Chapter 4. The results of this study have been published in [4].

Three polymers of bromine-substituted polyethylene (PEBr) are seen to crystallise with a cessation in their growth rate as function of cooling [5]. These polymers have two differing forms, Form I and II [6, 5]. It was suggested that the growth rate minimum was due to poisoning of the growth of Form II by Form I growth, however, WAXS shows that both crystals above and below the poisoning are that of Form II. A model was developed based on poisoning between Form I and Form II. The model fails to reproduce the experimentally observed curves unless it is assumed that the attachment rate of Form II is higher than that of Form I. However, Form I was found to have a higher nucleation density than Form II which makes this assumption unphysical. By assuming that PEBr crystallises with quantised lamellar thickness, it is possible to explain these dynamics by poisoning due to competing lamellar thickness. The model of different lamellar thicknesses derived in Chapter 3 does a good job of producing curves that fit the trend and shapes of the growth rate of PEBr [4]. Though the model is good at fitting the data and provides an alternative take on the mechanism behind the self-poisoning, there is no experimental data to support it. More x-ray diffraction (XRD) work for more accurate measurement of the crystallinity of the crystal forms formed at different temperatures and determination of the crystalline layer thickness need to be done to provide the evidence to distinguish between the two models.

A united-monomer model of poly(ethylene bromine) (PEBr) was developed to study its crys-

tallisation further. The model was made by extending the existing united-monomer model for PE to include dibromo groups [7]. By employing the self-seeding crystallisation protocol, it was possible to simulate PEBr crystallise. The resulting crystallises were seen to growth with quantised lamellar thickening with increasing crystallisation temperature which seems to be the result of the dibromo groups. Though quantised lamellar thickening is experimentally observed in polymers like long chain n-alkanes [3, 8] and PEB [1, 4], it is rare in simulation. The quantisation was not seen for crystals grown with continuous cooling. The PEBr chains seem to prefer to fold at the Br groups. When the systems where quenched to room temperature the Br groups formed registered layers within the crystalline layers similar to those seen in Form I′ of PEBr [6]. However, they did not show the Form II structure. The discovery of the quantisation in the these simulations present an insight into how to modify molecular architecture. By systematically placing small chemical moieties, halogens, or short chain branches the semi-crystalline morphology can be controlled.

Cui et al [9] carried out a study of the low- and high-molecular-weight poly(lactic acid) (PLA) stereocomplex (SC). In the SC the enantiomers are arranged in an antiferrochiral structure. The growth of the SC is highly suppressed in the high-molecular-weight case, while it crystallises to near completion in the low-molecular-weight case. They suggested that in the high-molecular weight case there are fluctuations in the melt that results in a build up of the HC at the SC growth front, and this disrupts the antiferrochiral arrangement and slows down the growth. The crystallisation of the PLA stereocomplex is simulated by a Monte Carlo simulation on a square lattice, where each site represents a helical segment of a chain in the lamella. The simulation uses the Metropolis-Hastings algorithm, where lattice sites undergo crystallisation, melting, and diffusion processes with probabilities dependent on parameters that model temperature and diffusion. The results reveal that diffusion and melting parameters, d and q, play significant roles in determining the rate and extent of crystallisation. Higher diffusion rates (d) accelerate crystallisation, while melting rates (q) above a critical threshold destabilise the SC. In the study two different initial lattice configurations are explored, one which is randomly populated and one which has local clustering. The clustered lattice showing increased likelihood of of having HC clusters, which reduces the crystallinity of the SC. The results show that it is possible to improve the SC growth with a seed and at lower temperatures, where $q > 0.45$.

LC phases made of straight achiral dimers of polycatenars have been observed to have chiral columns [10]. Each unit cell comprises of four left- and four right-handed columns, making the system achiral as a whole. It is possible to model the interactions of two such dimers as linear electric quadrupoles because of the similarity between the interactions of dimers and quadrupoles, and the similarity in their structure. The dependency of the quadrupole interaction energy on their orientation allows us to be able to simulate the twisting in the helical columns by continually rotating the quadrupoles from $z = 0$ going up the z-axis, until the come back to their starting angle at $z = 0$. For two interacting columns, the interaction of energy per dimer is given by the average quadrupole-quadrupole interaction energy at different elevations. This average energy is seen to only depend on either the difference between the angles for columns of the same handedness (ν) and the sum of the angles for columns of different

handedness ω. Both ν and ω are constant and independent of height along the z-axis. The average minimum energy per dimer happens when both ν and ω are 90°, with a value of $\frac{9}{32}$ units of $\frac{\phi^2}{r^2}$ for columns of the same handedness and $-\frac{87}{32}$ for those of different handedness. When the Fddd was compared with four other configurations on a hexagonal lattice, with the energy per dimer calculated using the quadrupole model, it had the lowest energy. Ideally two of these columns would prefer to have neighbours of the opposite handedness because it would mean less clashing. On a hexagonal lattice it is impossible to have all neighbours be of a different handedness. The best arrangement is to maximise the number of neighbours of the opposite handedness, and that is what the Fddd does.

8.2 Future Work

In future work, a rigorous error analysis will be performed to assess the reliability and validity of the results. For curve fitting using Python's curvefit function, confidence intervals for fitted parameters will be determined using covariance matrices, and residual analysis will be conducted to identify systematic deviations. Additionally, bootstrapping techniques may be employed to estimate parameter uncertainties. In molecular dynamics simulations using LAMMPS, convergence tests will be implemented by running multiple independent simulations with varying initial conditions to ensure statistical robustness. Sensitivity analysis will also be applied to assess the effect of simulation parameters, such as time step and thermostat settings, on the final results. For the Monte Carlo simulations on a 2D lattice, the model suggests that initial conditions play a crucial role, as observed experimentally. Therefore, different initial configurations will be tested to evaluate their impact on crystallisation dynamics. Furthermore, ensemble averaging over multiple runs will be used to mitigate the effects of stochastic fluctuations. In the case of BFGS optimisation, the stability of solutions will be checked by varying initial guesses and monitoring the convergence behaviour. By implementing these validation techniques, future work will strengthen the reliability of the numerical findings and ensure their consistency with experimental observations.

Building on the findings of the molecular simulation of poly(ethylene bromine), future investigations can explore how both the spacing and quantity of bromine groups impact the semi-crystalline structure and regulate lamellar thickening. Additionally, larger-scale systems may be examined to study the recently observed chevron-shaped crystals, characterised by lamellae approximately 70 nm thick, and to assess whether the united-monomer model accurately captures these key structural features. Models with the bromine atoms every 10th bead (PEBr20) ensuring uniformity in chain would also be of interest, as well as having a single bromine atom as opposed to two. Using multi-state iterative Boltzmann inversion for coarse-graining in future work might improve the simulation and show Form II.

Currently the simulations in for PLA are done with nucleus seeds that are the same and of different sizes. Future work could explore the effects of different nuclei, at different positions

and the number of seeds, on the crystallisation of the SC. Another avenue that could be explored includes using non-isothermal simulations involve varying the temperature during the simulation. This may yield results more comparable to the experimental results. It would also be interesting to carry out the simulations on larger lattices such as a 100 by 100 lattice.

A lot of time was spent trying to find an equivalent model for the bent core molecules as in the straight molecules, no success. They are thought to have a distorted hexagonal lattice unlike in the straight molecules. Instead of the molecules rotating around their centres, they are assumed to rotated off the centre, therefore the distance between molecules are not fixed. The bent molecules may be studied using molecular dynamics in future to investigate their assembly.

References

[1] Stephanie F Marxsen et al. "Crystallization Rate Minima of Poly(ethylene brassylate) at Temperatures Transitioning between Quantized Crystal Thicknesses". In: *Macromolecules* (2022).

[2] Paul G Higgs and Goran Ungar. "The growth of polymer crystals at the transition from extended chains to folded chains". In: *The Journal of Chemical Physics* 100 (1 1994), pp. 640–648.

[3] Goran Ungar and Andrew Keller. "Time-resolved synchrotron X-ray study of chain-folded crystallization of long paraffins". In: 27 (12 1986), pp. 1835–1844.

[4] Kutlwano Gabana et al. "Quantitative Model of Multiple Crystal Growth Rate Minima in Polymers with Regularly Spaced Substituent Groups". In: *Macromolecules* (2024).

[5] Xiaoshi Zhang et al. "Effect of Self-Poisoning on Crystallization Kinetics of Dimorphic Precision Polyethylenes with Bromine". In: *Macromolecules* 51 (4 2018), pp. 1386–1397.

[6] Masafumi Tasaki et al. "Polymorphism and phase transitions of precisely halogen-substituted polyethylene. (1) Crystal structures of various crystalline modifications of bromine-substituted polyethylene on every 21st backbone carbon". In: *Macromolecules* 47 (14 2014), pp. 4738–4749.

[7] William S Fall et al. "Role of Short Chain Branching in Crystalline Model Polyethylenes". In: *Macromolecules* 55 (2022), p. 8438.

[8] G Ungar and A Keller. "Long range intermixing of paraffin molecules in the crystalline state". In: *Colloid and Polymer Science* 257 (1979), pp. 90–94.

[9] Jiaming Cui et al. "Poisoning by Purity: What Stops Stereocomplex Crystallization in Polylactide Racemate?" In: *Macromolecules* 56 (3 2023), pp. 989–998.

[10] Ya xin Li et al. "A case of antiferrochirality in a liquid crystal phase of counter-rotating staircases". In: *Nature Communications* 13 (1 2022).